

ISTANBUL TECHNICAL UNIVERSITY ★ GRADUATE SCHOOL OF SCIENCE
ENGINEERING AND TECHNOLOGY

**IONOSPHERIC VARIABILITY OVER ISTANBUL USING SID-VLF AND HF-
RADAR OBSERVATIONS**

M.Sc. THESIS

Ayşegül Ceren MORAL

Department of Meteorological Engineering

Atmospheric Sciences Programme

JANUARY 2014

ISTANBUL TECHNICAL UNIVERSITY ★ GRADUATE SCHOOL OF SCIENCE
ENGINEERING AND TECHNOLOGY

**IONOSPHERIC VARIABILITY OVER ISTANBUL USING SID-VLF AND HF-
RADAR OBSERVATIONS**

M.Sc. THESIS

Ayşegül Ceren MORAL
511111002

Department of Meteorological Engineering

Atmospheric Sciences Programme

Thesis Advisor: Prof. Dr. Zerefşan KAYMAZ

JANUARY 2014

İSTANBUL TEKNİK ÜNİVERSİTESİ ★ FEN BİLİMLERİ ENSTİTÜSÜ

**SID-VLF İLE HF RADARI VERİLERİ KULLANILARAK İSTANBUL İÇİN
İYONOSFERİK DEĞİŞKENLİĞİN BELİRLENMESİ**

YÜKSEK LİSANS TEZİ

**Ayşegül Ceren MORAL
511111002**

Meteoroloji Mühendisliği Anabilim Dalı

Atmosfer Bilimleri Programı

Tez Danışmanı: Prof. Dr. Zerefşan KAYMAZ

OCAK 2014

Ayşegül Ceren Moral, a **M.Sc.** student of ITU **Institute of Science and Technology** 511111002, successfully defended the **thesis** entitled “**IONOSPHERIC VARIABILITY OVER ISTANBUL USING SID-VLF AND HF-RADAR OBSERVATIONS**”, which she prepared after fulfilling the requirements specified in the associated legislations, before the jury whose signatures are below.

Thesis Advisor : **Prof. Dr. Zerefşan KAYMAZ**
İstanbul Technical University

Jury Members : **Prof. Dr. H. Sema TOPÇU**
İstanbul Technical University

Prof. Dr. Zafer ASLAN
İstanbul Aydın University

Date of Submission : 16 December 2013
Date of Defense: 24 January 2014

To my mother Muhterem Pakyürek, brother Ergin Moral and Boris,

FOREWORD

I would like to thank my thesis advisor Prof Dr. Zerefşan Kaymaz for her constant support, understanding and guiding throughout stages of this work. I appreciate her extraordinary patience, which made the hardest moments of our study easier and bearable. I have met with her when I was taking the courses on Space Environment and Planetary Atmospheres during my senior year and thereafter decided to study in the fascinating world of space weather. Her inspiring deep knowledge attracted me into the field. Next, I would like to express my gratitude to my colleagues and friends in the Upper Atmosphere and Space Weather Laboratory; Ceren Kalafatoğlu Eyigüler, Filiz Türk Katırcıoğlu, İklim Gençtürk Akay and Doğa Can Su Öztürk from whom I have benefitted a lot through our scientific discussions and our weekly gatherings. My special thanks are for my precious friends Nihan Karataş, Meral Tuna and Emel Ünal for being there when I need their presence and support. I also sincerely thank to my colleagues in Room 310, especially to Nilcan Akataş and Aslıhan Vuruşkan, in sustaining a cozy and peaceful atmosphere in our little cubicles. Lastly, I would like to give my wholehearted thanks to my family for their infinite and unconditional love and support that we usually take it for granted.

This work has been supported by two projects; İTÜ BAP project No 36514 and TÜBİTAK project no 113Y213. İTÜ BAP project is used to analyze the SID-VLF data while TÜBİTAK project is used for the ionosonde part presented here

December 2013

Ayşegül Ceren MORAL
Meteorological Engineer

TABLE OF CONTENTS

	<u>Page</u>
FOREWORD	ix
TABLE OF CONTENTS.....	xi
ABBREVIATIONS	xiii
LIST OF TABLES	xv
LIST OF FIGURES	xvii
SUMMARY	xxi
ÖZET.....	xxv
1. INTRODUCTION.....	1
1.1 Radio Waves	3
1.2 Very Long Frequency (VLF) Waves	5
1.3 High Frequency (HF) Waves	6
1.4 Frequency and Electron Density Relation.....	7
1.5 Ionospheric Variability.....	10
1.6 Ionospheric Observations	12
1.7 Unusual Events in Ionosphere	15
1.7.1 Sporadic E.....	15
1.7.2 Spread F	16
1.7.3 Sudden ionospheric disturbances	17
1.7.4 Travelling ionospheric disturbances and gravity waves	18
1.7.5 Solar Activity	18
1.7.5.1 Solar flares.....	19
1.8 Purpose of the Thesis.....	21
2. SUDDEN IONOSPHERIC DISTURBANCES (SIDS) AND VLF WAVES..	23
2.1 SIDs as Seen in VLF Signals	28
2.2 Literature on SID and VLF Relation.....	31
3. SID ANALYSIS USING VLF DATA RECORDED AT ITU SID MONITOR	35
3.1 ITU SID-VLF MONITOR	35
3.2 Results From SID-VLF Observations	37
3.2.1 General structure	37
3.2.2 Effects of solar flare	43
3.2.3 Wave structures	46
4. SUMMARY AND CONCLUSION FROM ITU SID-VLF OBSERVATIONS	49
5. ITU HF RADAR, IONOSONDE, AND IONOSONDE OBSERVATIONS ..	51
5.1 Background Work On Ionosphere By HF Radars: E And F Layers	54
5.2 Ionospheric Models	65
5.2.1 International reference ionosphere (IRI)	65
5.2.2 TIE-GCM	67
6. RESULTS OF HF RADAR.....	71

6.1 General Character of F2 layer at Istanbul.....	71
6.2 Typical Ionospheric Daily Variations Observed At Istanbul	82
6.3 Substorm Effects	86
7. SUMMARY AND CONCLUSIONS.....	98
REFERENCES.....	105
CIRRICULUM VITAE	107

ABBREVIATIONS

CME	: Coronal Mass Ejection
DPP	: Delayed Positive Phase
EUV	: Extreme Ultraviolet
foF2	: Critical Frequency of F2 Layer
HF	: High Frequency
IMF	: Interplanetary Magnetic Field
IRI	: International Reference Ionosphere
ITU-UUBF	: İstanbul Technical University Aeronautics and Astronautics Faculty
MSTIDs	: Medium-Scale TIDs
MUF	: Maximum Usable Frequency
NeXtYZ	: Three-dimensional electron density inversion for dynasonde
NmF2	: Peak Electron Density Of The F Region
NPP	: No Positive Phase
RPP	: Regular Positive Phase
SID	: Sudden Ionospheric Disturbances
SWF	: Short Wave Fades
TEC	: Total Electron Content
TID	: Traveling Ionospheric Disturbances
TIE-GCM	: Thermosphere-Ionosphere Electrodynamics Circulation Model
ToA	: Time of Arrival
UV	: Ultraviolet
VLF	: Very Low Frequency
vTEC	: Vertical Ionospheric Electron Content

LIST OF TABLES

	<u>Page</u>
Table 1.1 : The maximum electron density and the height that it is observed.....	3
Table 1.2 : EM waves according to their frequency and wavelength [4].....	4
Table 1.3 : Solar flare classifications	20
Table 2.1 : Characteristics of the VLF signals transmitted by the VLF stations	27
Table 3.1 : Statistical properties for the data given in Figure 3.5.	41
Table 3.2 : Statistical properties for the data given in Figure 3.6.	43
Table 6.1 : Statistical properties for the data given in Figure 6.2.	75
Table 6.2 : Statistical properties for the data given in Figure 6.3.	77
Table 6.3 : Statistical properties for the data given in Figure 6.4	79
Table 6.4 : Statistical properties for foF2 data given in Figure 6.5.	80
Table 6.5 : Statistical properties for hmF2 data given in Figure 6.5.....	81
Table 6.6 : Statistical properties for TEC data given in Figure 6.5.....	82
Table 6.7 : Mean DST and AE values for selected cases.....	87
Table 6.8 : Statistics from model-model and model-data comparisons	97

LIST OF FIGURES

	<u>Page</u>
Figure 1.1 : Formation of Ionosphere by incoming solar radiation at higher altitudes [1].....	1
Figure 1.2 : Ionosphere and its layers; during the day (dashed line) and during the night (solid line) [2]	2
Figure 1.3 : Electromagnetic spectrum showing the range of radio waves used in this study [3]	4
Figure 1.4: Comparison of size of the VLF and HF Transmitter Antennas [5].....	6
Figure 1.5 : Propagation of VLF and HF radio waves through ionosphere [1].....	7
Figure 1.6 : Ionospheric layers and reflection of radio signal. Left panel gives the daytime conditions while the right panels illustrate the nighttime conditions [6].	9
Figure 1.7 : The wintertime daily variation of electron density over Canberra [1].....	11
Figure 1.8 : Sketch showing the latitudinal dependence of electron density at day (left) and night (right) [1].....	11
Figure 1.9 : Solar cycle dependence of HF frequency waves over Canberra [1]	12
Figure 1.10: Components of an ionosonde (top row); transmitter, receiver and ground station. Virtual height concept and Ionogram are given at the bottom row [1].	14
Figure 1.11 : An example of a real ionogram [8].....	15
Figure 1.12 : Illustration of Sporadic E layer [1].....	16
Figure 1.13: Illustration of Spread F [1]	17
Figure 1.14 : Active Sun [12]	19
Figure 1.15 : Effects of radio wave propagation [13].....	20
Figure 2.1 : Illustration of VLF propagation in the presence of solar glare and increased ionization in D layer [21].....	25
Figure 2.2 : VLF propagation under the day (right) and night (left) ionospheric conditions.....	25
Figure 2.3: Distribution of the stations with VLF transmitter over the globe. Red circles indicate the transmitter sites used to monitor the ionosphere at ITU SID station.....	26
Figure 2.4 : SID Monitor to detect the solar flare effects on ionospheric D-region [22].....	28
Figure 2.5 : An example of daily variation of SID data for quiet conditions [22].....	29
Figure 2.6 : Daily typical VLF recording of SID events with an active Sun picture [22].....	29
Figure 2.7 : An example of SID data for disturbed conditions [22]	30
Figure 2.8 : An example of VLF data showing lightning signatures [22]	31

Figure 3.1 : ITU-SID antenna on the roof of the Astronautics and Aeronautics Faculty, ITU	35
Figure 3.2: ITU-UASW Lab Group members performing the antenna setup: sitting from left to right are Doğa Can Su Öztürk, Zerefşan Kaymaz, Emine Ceren Kalafatoğlu Eyigüler, and İklim Gençtürk Akay (Photo taken by Ayşegül Ceren Moral).....	36
Figure 3.3 : Top: An example of VLF recording from ITU station on the day of October 31, 2011. The signal transmitter is the BAFA VLF station. Bottom: GOES15 X-ray flux. Red lines indicate the sunrise (left) and sunset (right)	37
Figure 3.4 : Four examples of VLF variations recorded at ITU SID station. Transmitting station is BAFA, Turkey	39
Figure 3.5: Monthly distributions of VLF signals transmitted from Bafa and received at ITU.....	40
Figure 3.6 : Seasonal variations of VLF data received at ITU VLF station	42
Figure 3.7 : VLF signal strength (top) and the GOES 15 X-ray flux data (bottom).....	44
Figure 3.8: Top: Example of VLF data on 18th of October 2012. Bottom: Corresponding GOES 15 X ray flux data.	45
Figure 3.9 : Example of ITU SID-VLF data on day March 18, 2013 with no solar flare association	45
Figure 3.10 : Example of wavy structures in ITU VLF data plotted in three successive days from March 4 to 6, 2013	47
Figure 3.11: Example of wavy structures in VLF data plotted for a week (March, 1-7 2013).....	47
Figure 5.1 : Photo of the ITU Dynssonde components: (a) transmitter site and transmitters, (b)one of the four recievers, (c) mobo continig the Dynasonde hardware.....	53
Figure 5.2: A daytime ionogram example produced by NeXtYZ at ITU on day Dec 15, 2013.....	54
Figure 5.3 : Normalized median TEC during geemagnetic storm at Hamilton (top) and Aerocibo (bottom) [28]	58
Figure 5.4 : TEC variations at 7 stations in North US during March 8, 190 ionospheric storm [29]	59
Figure 5.5: TEC variation at different seasons during the four days following the storm [34].....	61
Figure 5.6 : Averaged daily TEC variations under different solar activity periods [14].....	62
Figure 5.7 : Variations in TEC at different longitudes at low latitudes for three stations [14].....	63
Figure 5.8: Monthly variations of TEC in 1971 at Sagamore Hills, MA, USA [14].....	64
Figure 5.9 : Nighttime variations of TEC for six different events. Quiet time conditions at middle right panel.....	65
Figure 6.1 : On the left is an example of two ionograms to illustrate the day and night differences at ITU station for the day April 21, 2013 at 12 LT and 00 LT times. On the right, daily variation is presented for the ionospheric parameters of F2, hmF2, foE, hmE and TEC on the same day.....	72
Figure 6.2: Monthly variations of foF2, the critical frequency of F2 layer.	74

Figure 6.3 : Monthly variation of hmF2, height corresponding to maximum electron density in F2 layer.....	76
Figure 6.4 : Monthly variation of TEC, Total Electron Content of 1-year data	78
Figure 6.5: Seasonal variations of foF2 (first column), hmF2 (second column) and TEC (third column).....	80
Figure 6.6 : Four typical daily variations observed in foF2 in 2013 at Istanbul.....	83
Figure 6.7 : Variability illustrated with foF2 versus hmF2 for two events	84
Figure 6.8: Gravity wave example seen on day of October 8, 2012.....	85
Figure 6.9 : Expanded version of Figure 6.9 to show the gravity wave structure in detail.....	86
Figure 6.10 : Daily variations of ionospheric parameters, foF2, hmF2 and TEC on selected quiet and disturbed days	88
Figure 6.11: Comparison of the daily variation of TEC of the selected cases with those of the models	90
Figure 6.12 : Differences between the model predictions and ITU Dynasonde data for selected quiet and magnetically disturbed days	91
Figure 6.13 : ITU electron density profiles produced by NeXtYZ at different phases of the substorms for the selected cases. Black, green and red denote the beginning, expansion and recovery phase of the substorms respectively	93
Figure 6.14: Model-Data comparisons during the different phases of the substorms during beginning (top), expansion (middle) and recovery (bottom) phases.....	94
Figure 6.15 : Comparisons between the models during the different phases of the substorms during beginning (top), expansion (middle) and recovery (bottom) phases.....	96

IONOSPHERIC VARIABILITY OVER ISTANBUL USING SID-VLF AND HF-RADAR OBSERVATIONS

SUMMARY

Ionosphere is the conductive layer of the atmosphere extending from about 60 km to 2000 km, although there is not any upper limit. It blends into the outer space. It is formed as a result of the interaction between the neutral atoms and molecules of the upper atmosphere with the solar radiation. Therefore, the amount of solar radiation and the composition of the upper atmosphere, i.e. the density and the type of the neutral atoms, determines how strong the ionosphere is. As the solar radiation and the number density of electrons vary with height in an opposite sense, this dependence leads to distinct layers in the ionosphere. These layers are, in general, known as D, E, F1 and F2 layers respectively from the bottom towards up. Whilst this classification defines the daytime ionosphere, owing to the decreasing solar radiation during the night, D layer disappears and the F1 and F2 layers are combined into F layer and these then form the nighttime ionosphere.

Ionosphere plays a crucial role in communication and related areas. It is the electron density in the ionosphere that determines the frequency of the radio waves used in worldwide long distance communication and with the satellite communication. Especially GPS communications, which are the essential communication means of our era, depend largely on the behaviour of the ionosphere. The errors resulting from the variations in the electron density can reach errors on the order of 50-100 meters in distance predictions by GPS. The number of electrons in each ionospheric layer is associated with a specific frequency which determines the maximum usable frequency of the radio the waves. Therefore, the variations in electron density are the crucial factor for the success of radio communications in various levels. These variations in electron density can result from the several factors. In addition to the amount of total solar radiation reaching the Earth, the solar and magnetospheric activities are the main sources that cause variations in the ionization level in the ionosphere.

Radio waves are the low frequency electromagnetic waves which do not harm living organisms. These waves can propagate in the atmosphere without any change in their speed and direction unless they encounter a serious number of electrons which is the case in the ionosphere. Ionosphere can affect both the speed of the radio wave and change its direction, as well as it can totally absorb the radio wave or just attenuate some. When, how and which one will take place require predictions of ionospheric density which is one of the branches of Space Weather.

Ionosphere can be studied using VLF (Very Long Frequency) and HF (High Frequency) radio waves. While VLF waves are used to study the electron density variations in the lower ionosphere, D layer, HF waves are used to study the higher ionosphere, E and F layers. Ionosondes are very oldest radars, which use the time of

flight of the radio signal with frequencies between 1-3 MHz, to determine the electron density. In addition to ionosonde, incoherent radars such as EISCAT and line of site radars such as SuperDARN are used in the measurements of the ionospheric electron density. Ionospheric electron densities are also studied using models. Several ionospheric models are available such as IRI, TIEGCM, etc.

In this work, we study the electron density variations over İstanbul using SID-VLF and ionosonde-HF data. SID (Sudden Ionospheric Disturbances) are studied using VLF signatures received at İstanbul ITU station sent from different VLF stations spread over the globe. A SID monitor is located on the roof of ITU UUBF and records signals from several stations. By looking at the variations in the signal strength it is possible to detect the variations in the D-layer of the ionosphere and their sources. On the other hand, data from ionosonde established in the Ayazaga Campus of ITU is used to study the electron variations in the E and F layers of the ionosphere over İstanbul. In this study we present Case studies from selected events while we refer the statistical study to a extensive study.

In Chapter 4 of this thesis, we present our results from SID-VLF data. We find that the general structure of the signal strength is in accordance with the daily solar radiation. We see the signatures of the solar activity such as solar flares. The signal rates during these times can be increased or decreased depending on the activity level. Also, we determine general types of variations associated with D region electron density. Four types of daily variations are detected for which some can be explained in presence of solar activity, some with the solar radiation but we also have variations not attributable to both. We give discussion on these in the presence of available literature.

Ionosonde radar within the ITU campus is a type of Digisonde called Dynasonde or VIPIR (Vertically Incident Pulsed Radar). Dynasonde returns critical frequency of each ionospheric layer along with additional 79 additional ionospheric parameters including the total electron density and maximum height of the reflection. Dynasonde data collected since its establishment were used to determine the daily, seasonal and annual variation of the electron density over İstanbul. In addition to these statistics, solar activity and magnetospheric storm effects on ionospheric electron density were studied through selected events. Wave activities seen in the ionograms were studied in terms of magnetospheric and tropospheric effects. We find that the ionosphere is highly variable during the summer months with larger electron densities while it is less variable with lower electron densities during the winter. We see that the several types of daily variations were observed over İstanbul. While the electron density show its expected peak at noon time when the solar radiation is highest, we also see double peak structures again during the noon times but just before and after the noon time with a drop at the noon. Other variations include dusk events when we see higher electron densities during the evening time. In addition, we see wave structure during the early morning times, which are attributable to the gravity waves from the lower atmosphere. We also compare our observations with the current available models like International Reference Ionosphere (IRI) and TIEGCM. IRI model is dominantly driven by the solar radiation and does not have any solar and magnetospheric effects. TIEGCM, on the other hand, includes the solar and magnetospheric effects to some degree.

In this thesis, Chapters 1, 2 and 3 contain the SID-VLF study while Chapters 4, 5, and 6 comprise the analysis and results related to the ionosonde. Chapter 7 gives a general discussion and a summary of our study. It also covers the suggestions and future work.

SID-VLF İLE HF RADARI VERİLERİ KULLANILARAK İSTANBUL İÇİN İYONOSFERİK DEĞİŞKENLİĞİN BELİRLENMESİ

ÖZET

İyonosfer atmosferin 60km ile 2000 km arasındaki iletken tabakasıdır. Bu özelliği nedeni ile radyo dalgaları ile iletişimde önemlidir. İyonosfer güneş ışınları ile atmosferdeki nötral atomların etkileşimi sonucunda oluşur. Güneş radyasyonu atmosferin tepesinden aşağı doğru indikçe azalır. Buna karşılık nötral atom yoğunluğu yerden yükseldikçe azalır. Maksimum elektron yoğunluğu bu iki değişime bağlı olarak atmosferde farklı yüksekliklerde meydana gelir. Her bir maksimum elektron yoğunluğu bölgesi farklı bir iyonosfer tabakasını oluşturur. Bu tabakalar gündüz zamanı D, E, F1 ve F2 tabakalarıdır. Gece güneş radyasyonu daha az olduğundan elektron üretimi yeterli değildir. Bunun sonucu olarak geceleyin D tabakası kaybolur, F1 ve F2 tabakaları birleşerek F tabakasını oluşturur ve elektron yoğunluğu E ve F tabakalarında azalır, maksimum yoğunluğun olduğu yükseklik daha yukarıya kayar.

İyonosfer radyo iletişiminde çok önemlidir çünkü her bir tabakanın elektron yoğunluğu radyo dalgasının frekansı ile ilişkilidir. İyonosfer VLF ve HF frekansındaki radyo dalgalarını yansıtarak veya gücünü azaltarak veya tamamen absorblayarak radyo iletişimini ya mümkün kılar veya engel olur. Eğer iyonosferik tabakanın kritik frekansı radyo dalgasının frekansına eşit ise radyo dalgası o tabakadan yansır. Diğer yandan eğer radyo dalgasının gücü düşük ise dalga gündüz vakti D tabakasında absorblanır. Bu durumda iletişim gerçekleşmez. Gerek uzun mesafeli iletişimlerde gerekse uydularla olan iletişimlerde iyonosferik elektron yoğunluğu değişimlerini bilmek başarılı bir iletişim için çok önemlidir.

İyonosferin durumunun bilinmesi, radyo iletişimi açısından en çok GPS ile konum belirleme sistemleri için önemlidir. GPS ile konum belirleme sistemlerinde elektron yoğunluğundaki değişimler yaklaşık 50-100 metreye varan hatalara sebep olmaktadır.

İyonosferik elektron yoğunluğunun değişimine neden olan pek çok faktör vardır. Gelen güneş radyasyonu miktarı en temel faktördür. Bunlara ilaveten güneş aktiviteleri, manyetosferik fırtına aktiviteleri, gravite dalgaları bunlardan bazılarıdır. Güneş aktiviteleri arasında güneş alevleri ilk sırayı alır. Güneş alevleri sırasında uzaya çok miktarlarda yüksek enerjili parçacığın yanı sıra, x-ışınları ve daha kısa dalga boylarında radyasyon yayılır. Hem enerjiktik parçacıklar hem de özellikle bu x-ışınları aralığındaki elektromanyetik radyasyon iyonosferde en aşağı seviyelerdeki iyonizasyon miktarı değiştirirler. Bunlar oluştuğunda elektron yoğunluğu artar. Dolayısıyla ortamın iyonizasyonu da. Manyetik fırtınalar diğer yandan, manyetosferdeki, özellikle manyetik kuyrukta meydana gelen manyetik birleşme sonucunda atmosfere transfer edilen manyetosferik mikrofırtına dönemleri olup, iyonosferde hareketli iyonizasyon gruplarına neden olurlar. Gravite dalgaları ise kaynağı genelde troposferdeki yükselti değişimlerinden kaynaklanan düşey yönde

hareket ederken enerjisi artan ve nihayet iyonosferik seviyelerde kırılmaya uğradığında enerjisi bulunduğu ortama bırakan dalga yapılarıdır. Bu dalgaların oluşumuna zaman zaman manyetosferik fırtınalar da sebep olabilir.

Farklı ekenler sonucunda iyonosferde, Spread F, Sporadic E, orta Enlem çöküntüsü, gün batımı vakası vb. gibi düzensizliklere ilaveten, TIDs (hareket eden iyonosferik bozuntular veya SID aniden aratan iyonosferik bozuntular) da görülür. İyonosfer gün içinde, mevsimlik ve yıllık değişimlerine ilaveten yükseklikle ve coğrafik enlem ile de değişir. Ekvatoryel enlemlerdeki iyonosferik elektrodinamik ile orta ve yüksek enlemlerdeki iyonosferik dinamik ve bu nedenle de değişkenlikler farklılık gösterirler.

Radyo dalgaları, yaşayan canlılara zarar vermeyen, düşük frekanslı elektromanyetik dalgalarlardır. Bu dalgalar, iyonosferdeki elektronlarla girdikleri etkileşim haricinde, atmosferde hızlarında ve ilerleme yönlerinde hiçbir değişime uğramadan yol alırlar. İyonosfer, radyo dalgalarının hem hızında hem de yönünde bir değişime yol açarlar. Radyo dalgasını tamamen absorblayabilir ya da sadece güç kaybına uğramasına neden olabilirler.

İyonosfer VLF (Çok Uzun Frekanslı) ve HF (Yüksek Frekanslı) radyo dalgaları ile incelenebilir. VLF dalgaları aşağı seviye iyonosferin – D tabakası- özellikleri konusunda bilgi sahibi olmamızı sağlarken, HF dalgaları ile yukarı seviye iyonosfer –E ve F tabakaları- incelemek için kullanılır. Bu çalışmada, hem VLF hem de HF radarı (İyonzonde) kullanarak İstanbul üzerindeki iyonosferin genel durumunu belirlemeye çalıştık. Bunun için İTÜ Ayazağa yerleşkesi Uçak ve Uzay Bilimleri Fakültesinin çatısına bir adet VLF anteni kurduk. Bu SID-VLF anteni ile dünya geneline dağılmış pek çok VLF vericisinden 6 tanesini 2-yıl boyunca sürekli kaydettik. SID-VLF anteninin sinyal gücündeki değişimlerini, D tabakasındaki değişiklikleri belirlemekte kullandık. İncelemelerimiz sonucunda sinyal gücünün genel yapısının tipik olarak gelen güneş radyasyonuna paralel değiştiği görülmüştür. Güneş alevleri sırasında, aktivitenin seviyesine bağlı olarak, sinyal gücünde artma ya da azalmalara rastlanmıştır. Bazıları güneş aktiviteleri ile bazıları da gelen radyasyon miktarı ile ilişkilendirilebilen günlük dört karakteristik değişim gösterdiği belirlenmiştir.

E ve F tabakaları içinde iyonozonde radarı kullanıldı. İyonzondeler elektron yoğunluğunun tahmini için kullanılan radarlardır. 1-3 MHz arası frekansa sahip radyo dalgalarının vericiden gönderildikten sonra, iyonosferden geri yansıtılıp alıcıda kaydedilinceye kadar geçen süreyi kullanarak elektron yoğunluğunu hesaplarlar. İTÜ Ayazağa yerleşkesinde kurduğumuz iyonozonde radarı Dynasonde ya da VIPIR adıyla anılan bir Digisonde'dir. 25'er metrelik 2 vericisi, 4 adet alıcısı vardır. Dynasonde radar, NeXtYZ programı ile her iyonosferik tabakanın kritik frekanslarının yanında 79 ilave parametrenin daha ölçümünü de verir. Bu parametrelerden bazıları toplam elektron yoğunluğu ve maksimum yansıma yüksekliğidir.

Dynasonde radarı, kurulduğu gün olan Ekim 2012'den bu yana veri kaydetmektedir. Başlangıç olarak bu veriler İstanbul'un elektron yoğunluğundaki günlük, aylık ve mevsimlik değişimleri ortaya çıkarmak için kullanılmıştır. Bunun yanı sıra manyetosferik aktivitelerin elektron yoğunluğu üstüne olan etkileri de vaka çalışmaları yolu ile araştırılmıştır. Bu kısımda manyetosferik mikrofırtına dönemleri manyetik indekslere bakara belirlenmiş ve söz konusu günlerdeki elektron yoğunluğu, maksimum yükseklik ve TEC incelenmiştir. HF Radar (İyonzonde)

verileri mevcut iyonosferik modeller ile karşılaştırılmıştır. IRI ve TIGCM kullanılan ii modeldir. IRI, International Reference Ionosphere, uluslararası bir çaba sonucunda amatör radyo kullanıcılarına doğru iyonosferik haberleri verebilmek amacı ile ortaya çıkmıştır. Zaman içinde gelişmiş, geliştirilmiş bugün iyonosferin herhangi bir coğrafi bölgesindeki ve herhangi bir andaki elektron yoğunluğunu elde etmek için pek çok amaç için kullanılmaktadır. İyonosferin ekstrem durumlarını ve değişkenliğini doğru yansıtmaya da ortalama şartlardaki iyonosferi verdiğiinden karşılaştırma amacı ile kullanılmıştır/kullanılmaktadır. Diğer yandan, TIEGCM modeli biraz daha gerçeğe yakın durumları, mikrofırtınaların daha iyi entegre edilmesi gibi, vermektedir. Her iki model de açık model olup serbestçe kullanılabilir.

Bu çalışmanın ana amacı İstanbul Teknik Üniversitesi yerleşkesinde bulunan SID-VLF ve Dynasonde HF frekanslarındaki sinyallerdeki değişkenlikler kullanılarak iyonosferin elektron yoğunluğundaki değişimleri gözlemlemek ve elektron yoğunluğu değişimine sebep olan fiziksel ve dinamik süreçleri belirlemektir. Bunun için güneş alevleri tepkisine ve manyetosferik mikrofırtına dönemlerindeki değişimlerine bakılmıştır.

SID-VLF monitörü Stanford Üniversitesinden elde edilmiştir. Dünya üzerine yayılmış 6 VLF istasyonundan gönderilen sinyalleri gözlemektedir. HF radarı ise ITU Rektörlüğü'nün desteği ile elde edilmiştir. HF verileri ile öncelikle genel iyonosferin durumunu belirlemek için günlük, aylık ve mevsimsel değişiklikler belirlenmiş, iyonogramlarda görülen yerçekimi dalgası araştırılmış, manyetosferik fırtına etkileri incelenmiş ve elde edilen sonuçlar mevcut iyonosferik modeller ile IRI ve TIE-GCM, karşılaştırılmış ve değişime neden olan fiziksel süreçler anlaşılmasına çalışılmıştır. Elde edilen sonuçlar mevcut literatürdeki bulgular ile karşılaştırılmıştır. Manyetik açıdan sakin ve aktif günler için vaka analizleri yapılmıştır. Bu vakalar mevcut iyonosferik model çıktıları ile karşılaştırılmıştır.

Bu çalışmanın ilk bölümünde (Bölüm 1) iyonosferin oluşumu, yapısı ve genel özellikleri ve radyo dalgalarının özellikleri verilmiştir. Bölüm 2'de ITU-VLF istasyonunun kurulumu ve özellikleri ile literatür çalışmasına değinilmiştir. Bölüm 3'de SID VLF genel yapısı, güneş alevi ile ilişkilendirilmesi ve dalgalı yapı incelenmiştir. 4. bölümde SID-VLF analizlerinin sonuçları verilmiştir. Bölüm 5'te HF radarları ile ilgili literatür çalışması, iyonosferik modeller hakkında kısa bilgi verilmiştir. 6. bölümde iyonozonda verileri ile bakılan İstanbul üstündeki iyonosferin genel yapısı incelenmiş, günlük karakteristik değişimler çalışılmış, yerçekimi dalgaları ile etkileşime bakılmış ve mevcut iyonosferik modellerle, IRI ve TIE-GCM, mikrofırtına etkileri incelenmiştir. Son bölüm olan Bölüm 7'de ise her iki veri setinden elde edilen sonuçlar tartışılarak özet ve sonuçlar verilmiştir.

1. INTRODUCTION

Ionosphere is the region of the atmosphere, which exhibits electrical properties owing to the free electrons resulting from the interaction between the shortwave length solar radiation and the neutral atoms of the upper atmosphere as it is depicted in Figure 1.1. If the energy of the solar radiation is enough to break an electron apart, a positively charged atom left. This process creates free electrons and ions in the region called ionosphere starting from 60 km and higher up [1].

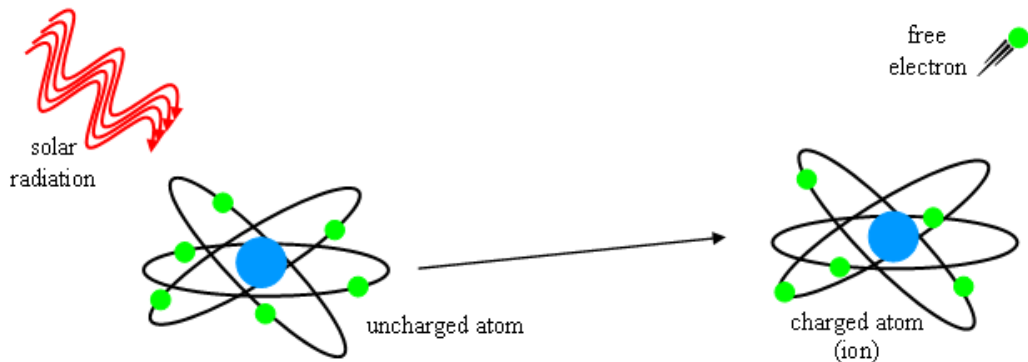


Figure 1.1: Formation of Ionosphere by incoming solar radiation at higher altitudes[1].

The electron density peaks at about 250 to 350 kms after which it decreases significantly. Figure 1.2 gives a simple sketch of the ionosphere. Since the solar radiation from the top of the atmosphere decreases as the solar radiation moves downward, and the number density of the neutral atoms decreases upward from the ground, this variation determines where the peak of the electron density occurs and creates distinct layers in the ionosphere with different characteristics. These layers are D, E, F1 and F2 layers during the daytime. D layer is the bottom most region of the ionosphere. The electron density in this region is the lowest compared to those in the E and F layers. Since the density of neutral atoms is higher than the density of the electrons in D region, the frequency of the collisions between electrons and neutral atoms are the highest. The highest electron density is found in the F2 layer, which is also the peak of the ionosphere and E and F1 layers are located between D

(~60-90 km) and F2 (200-350 kms). During the night, the solar radiation decreases. Thus, only E and F layers are seen with lesser electron densities. In other words, D layer disappears and F1 and F2 combine into one region called F region [1]. Table 1.1 below gives the maximum electron density and the height that it is observed.

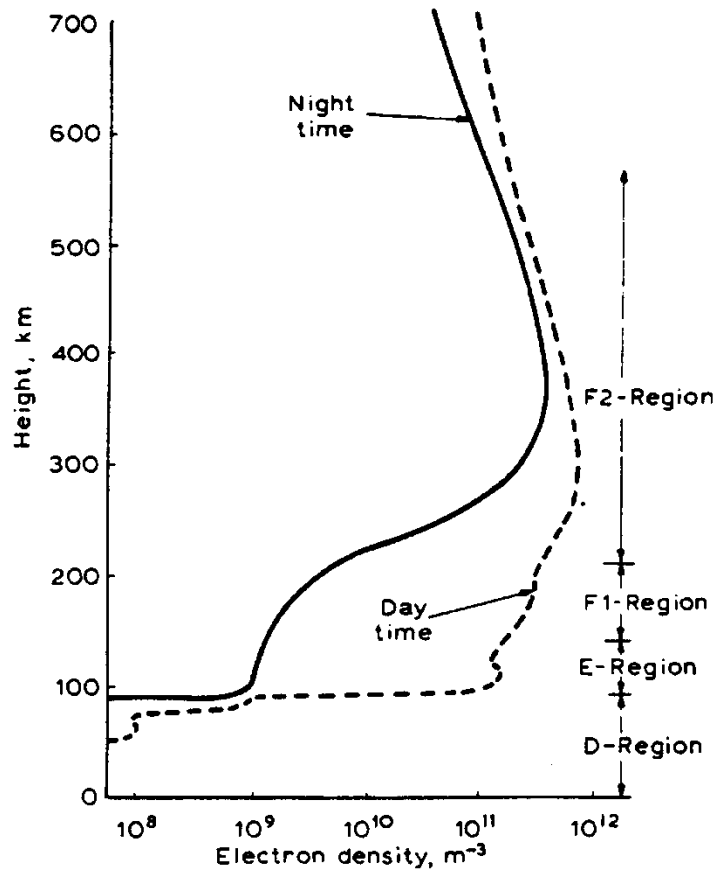


Figure 1.2: Ionosphere and its layers; during the day (dashed line) and during the night (solid line) [2].

Table 1.1: The maximum electron density and the height that it is observed.

Layers	Daytime Electron Density [cm^{-3}]	Daytime Critical Frequency [MHz]	Nighttime Electron Density [cm^{-3}]	Nighttime Critical Frequency [MHz]
D	2×10^3	0.4		
E	4×10^5	5.7	2×10^5	4
F1	2×10^6	12.7	7×10^5	7.5
F2	4×10^6	18		

1.1 Radio Waves

Figure 1.3 illustrates the electromagnetic spectrum and Table 1.2 gives the list of the frequency and wavelength bands corresponding to the radio waves. As can be seen from Figure 1.3 and Table 1.2, VLF (Very Low Frequency) waves take place in the 3-30 kHz frequency band corresponding to 10-100 km wavelength waves and HF (High Frequency) waves are found in the frequency range from 3-30 MHz corresponding to 10-100 m wavelength waves. Both frequency regions correspond to the non-ionizing part of the electromagnetic spectrum and not harmful for the living organisms.

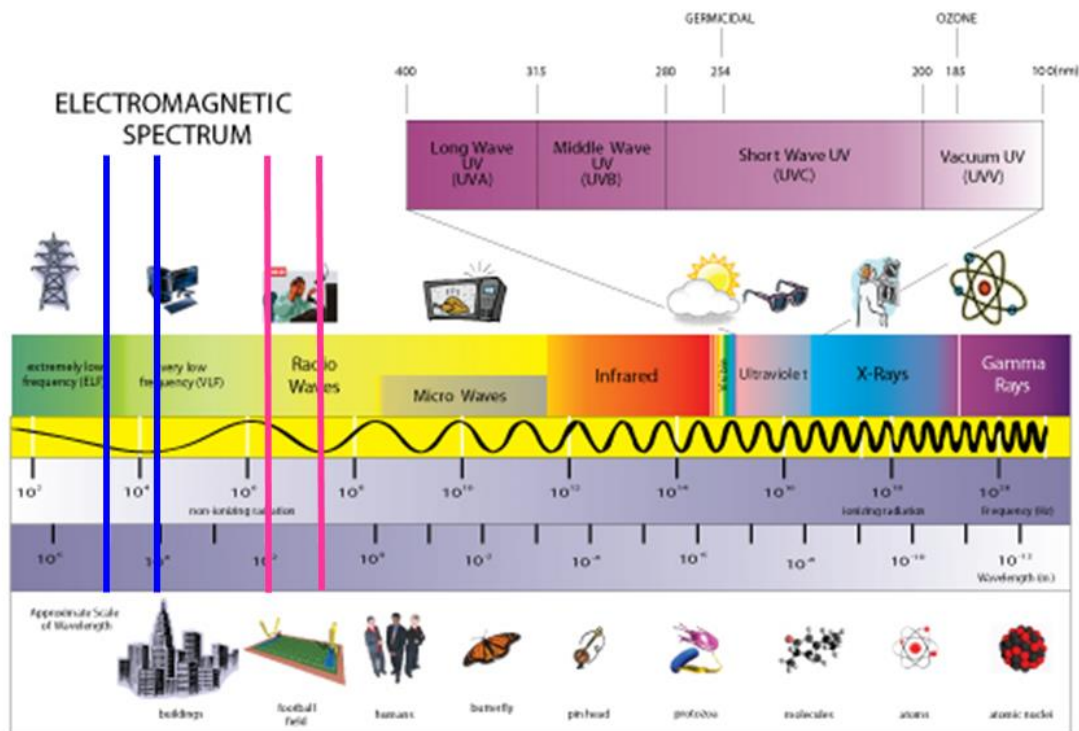


Figure 1.3: Electromagnetic spectrum showing the range of radio waves used in this study [3].

Table 1.2: Electromagnetic waves according to their frequency and wavelength [4].

Band name	Abbr	Frequencies	Wavelength
Extremely low frequency	ELF	3-30 Hz	100Mm-10Mm
Super low frequency	SLF	30-300 Hz	10000-1000 km
Ultra low frequency	ULF	300-3000 Hz	1000-100 km
Very low frequency	VLF	3-30 kHz	100-10 km
Low frequency	LF	30-300 kHz	10-1 km
Medium frequency	MF	300-3000 kHz	1 km – 100 m
High frequency	HF	3-30 MHz	100-10 m
Very high frequency	VHF	30-300 MHz	10-1 m
Ultra high frequency	UHF	300-3000 MHz	1 m- 100 mm
Super high frequency	SHF	3-30 GHz	100-10 mm
Extremely high frequency	EHF	30-300 GHz	10-1 mm

1.2 Very Long Frequency (VLF) Waves

Basic properties of VLF waves include [1]:

1. Because of their large wavelengths, VLF radio waves can diffract around large obstacles. Therefore, they are not blocked by mountain ranges, and they can propagate as a ground wave following the curvature of the Earth.
2. D layer of the ionosphere at 60 km altitude reflects VLF radio waves as seen in Figure 4.
3. These waves travel in a zigzag path between the Earth and the ionosphere.
4. VLF waves have very low path attenuation, 2-3 dB per 1000 km, with little of the "fading" experienced at higher frequencies. This is because VLF waves are not much more affected by ionization gradients and turbulence as they are reflected from the bottom of the ionosphere.
5. Because of (4), VLF transmissions are very stable and reliable, and are used for long distance communication.
6. They cannot be used in the transmission of the audio (voice).
7. They can be used to transfer only low data rate coded signals, like in the telegraph lines.

The VLF waves can be utilized in

1. A few radio navigation services,
2. Government time radio stations which broadcast time signals to set radio clocks,
3. Secure military communication,
4. Geological surveys,
5. Earthquake research,

Since VLF waves penetrate about 40 meters into saltwater, they are especially used for military communication with submarines.

One of the disadvantages of VLF waves, the VLF transmitter as seen in Figure 1.4 is much larger than the HF transmitter, which makes its usage impractical and costly.

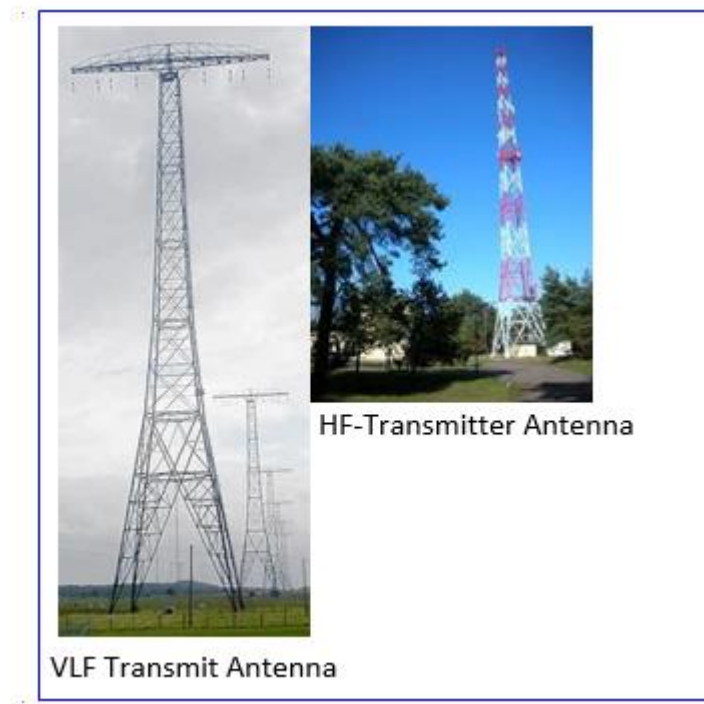


Figure 1.4: Comparison of size of the VLF and HF Transmitter Antennas [5].

1.3 High Frequency (HF) Waves

Some of the properties of the high frequency (HF) waves are given below [1]:

1. HF bands are used by commercial Radio broadcasting stations.
2. HF signals are reflected by the ionosphere at several heights above 60 km as seen in Figure 1.4.
3. Multiple reflections between ionosphere and earth occur, allowing great distances to be obtained in these ranges.
4. The disadvantage of this type of propagation is that it depends on the characteristics of the ionosphere, which varies widely, especially during daylight hours.
5. As a result of the variations in the ionosphere, HF waves are reflected differently and they take different paths over a period of time.
6. Because of (5), the HF signal at the receiver varies in strength, which causes the output to fade in and out.

HF waves are used for

1. radio communication
2. long distance communication
3. satellite communication including GPS communication
4. radar target detection

As seen in Figure 5, the HF transmitter antenna is smaller than VLF transmitter and thus, is more economical.

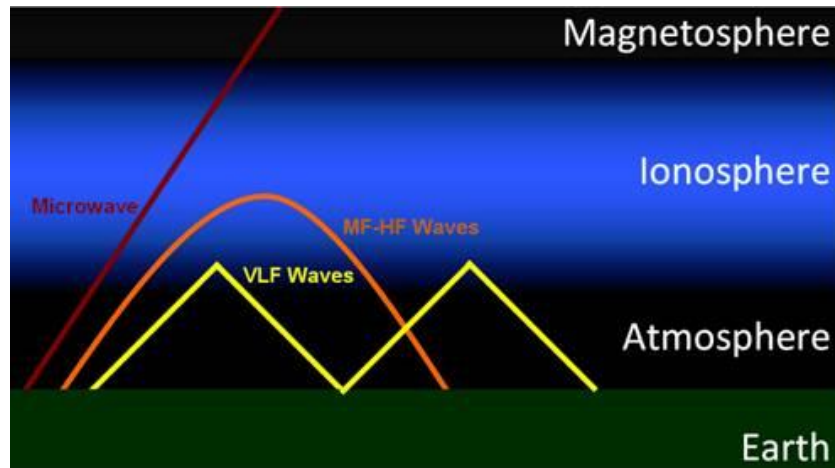


Figure 1.5: Propagation of VLF and HF radio waves through ionosphere [1].

SID-VLF recorder, which is present at the roof of ITU UUBF, observes VLF waves in the frequency of 3-30 kHz transmitted from several SID transmitters around world. The variations in electron density of the D region of the ionosphere are referred by looking at the variations in the signal power received at ITU. In addition, the HF variations in 3-30 MHz range measured by Dynasonde installed at ITU campus are studied to refer to the variations in E and F layer electron density.

1.4 Frequency and Electron Density Relation

The electron density in the ionospheric layers defines the range of the frequencies that the long distance communication and communication with satellites are possible. The ionosphere itself oscillates at its intrinsic frequency described as plasma frequency as given below.

$$f_p^2 = \frac{n_e q^2}{4\pi\mu\epsilon_0} \quad (1.1)$$

Where f_p denotes plasma frequency of the ionosphere, n_e is the electron density, q is the electronic charge, μ is the permeability of the medium, ϵ_0 is the emissivity.

In addition, each layer has a characteristic frequency defined as critical frequency associated with the electron density at the peak of each layer. This is given as below:

$$f_c = \frac{9 \times 10^{-3}}{\cos \alpha} \sqrt{n_{e,max}} \quad (1.2)$$

Where f_c gives the critical frequency of the ionospheric layer corresponding to the maximum electron density height, α is the incidence angle of the radio wave signal measured from the vertical and $n_{e,max}$ is the maximum electron density for each ionospheric layer. The critical frequency also gives the Maximum Usable Frequency (MUF) that one should use for a successful communication. It is the highest frequency that can be reflected from an ionospheric layer. No frequencies below the critical frequency of an ionospheric layer can penetrate the layer and they reflected back to the ground. In other words, if you choose a frequency lower than critical frequency of ionospheric layers, the layer is going to reflect your signal like a mirror. By knowing this feature of ionosphere, with given angle a radio signal can travel long distances in the atmosphere, without fading away.

We can summarize that the propagation of radio waves depends on two factors: incidence angle (α) and the number density of electrons ($n_{e,max}$). For vertically propagating ($\alpha=0$) radio waves this equation becomes,

$$f_c = 9 \times 10^{-3} \sqrt{n_{e,max}} \quad (1.3)$$

This is also equivalent to the plasma frequency of the region at that height at $n_{e,max}$.

As can be seen from these equations, depending on the number of electrons in each layer ionosphere affects the signal propagation in several ways. One of these effects is the reflection of the radio signals as seen in Figure 1.6. The ionosphere affects both the speed of the radio waves, and the direction by bending. When there are no free electrons, as in the lower atmosphere up to 60 km where the signal first encounter the ionosphere, the signal propagate at the speed of sound without any change in its direction. However, once the signal encounters the ionosphere, the part of the signal which is in the ionosphere propagate faster than the other part of the signal thus the signal's direction changes by bending which eventually causes a

reflection called specular reflection toward the Earth's surface. The phase velocity of the signal is related to the number density of the electrons as below:

$$u = \frac{c}{\sqrt{1 - 8.1 \times 10^{-5} \frac{n_e}{f^2}}} \quad (1.4)$$

Here, u shows phase velocity of radio wave; c is the speed of light; n_e is the electron density, f is the radio wave frequency.

The reflection of the signals from different ionospheric layers during the day (left) and night (right) are illustrated in Figure 1.6 below.

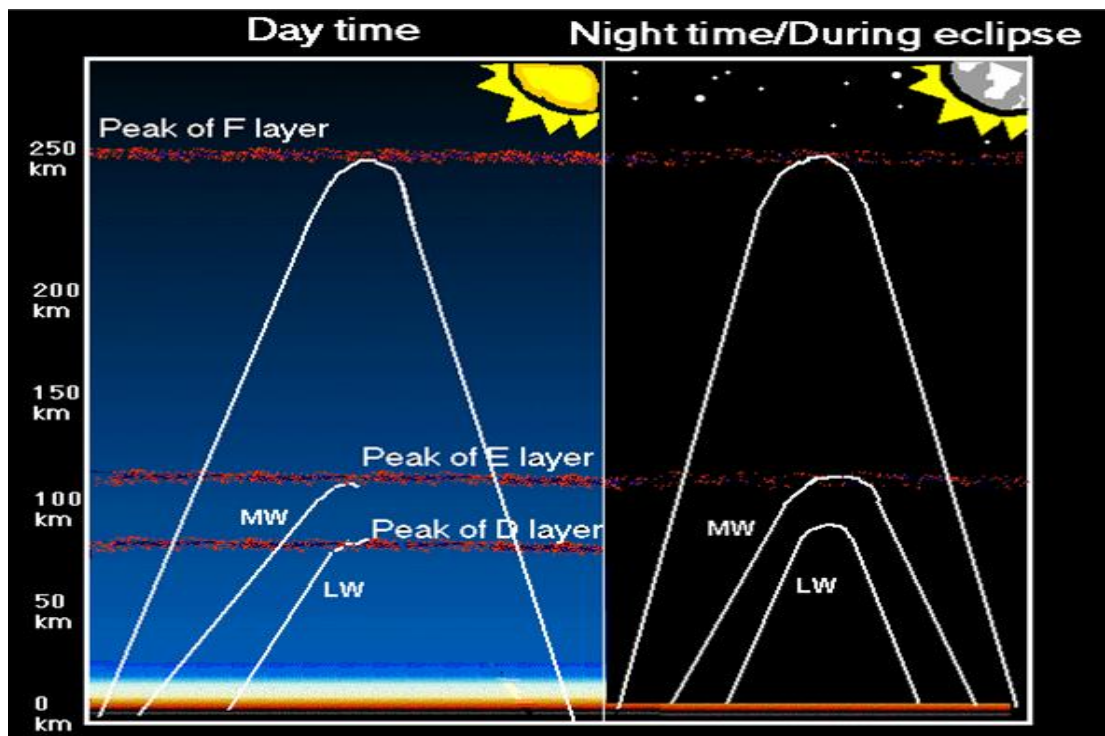


Figure 1.6: Ionospheric layers and reflection of radio signal. Left panel gives the daytime conditions while the right panels illustrates the nighttime conditions [6].

In addition to the reflection, ionosphere can also attenuate or absorb the HF radio waves depending on the density of the both electrons and also neutral atoms. This happens mostly in the D region of the ionosphere where the number of neutral atoms is more than the number of electrons. Electrons transfer the energy they receive from the radio wave to the neutral atoms through collisions. Depending on the amount of electrons and neutrals, electrons either totally absorb the radio energy or attenuate some and let the rest pass through (Figure 1.6). The transmitted part of the radio wave is weakened and thus they may not reach its destination. Therefore, the

daytime and night propagations of the radio waves differ depending on the number of electrons in the ionosphere. The daytime propagation should be chosen such that the signal can pass through the D layer. Thus, higher frequency is needed. On the other hand, since D layer is absent during the night, the signal strength should be decreased to prevent the interference of the signals. For a successful HF communication thus, the variations in electron density of the ionosphere should be taken into account. The high accuracy ionospheric electron density predictions are crucial in addition to the observational network of the HF transmitters over the world.

1.5 Ionospheric Variability

As stated in the previous section, daytime and nighttime profiles of ionosphere are greatly different. In the absence of incoming solar radiation, D region disappears at nighttime and E, F1 and F2 regions weakened. Difference between F1 and F2 regions become indistinguishable and they merged into one layer called as F layer. Path of a radio signal in daytime and nighttime showed below in Figure 1.2.

Electron density in the ionosphere varies with height and latitude. The result of the height variation is the ionospheric layers and this is illustrated in Figure 1.2. The main reason for this is the amount of solar radiation and the composition of the neutral atmosphere, i.e. density and type of the neutral atoms. The electron density in the ionosphere shows daily, seasonal, annual variations and variations with solar and magnetospheric activity.

Daily variations in electron density result from the variations in the amount of solar radiation with variations low during the night and high during the day with peak at noon or a little after noon at Local time. Figure 1.7 gives the daily variation of electron density during the wintertime and corresponding to solar maximum time over a mid-latitude station in Australian city, Canberra (35.3°S, 149.0°E) [1].

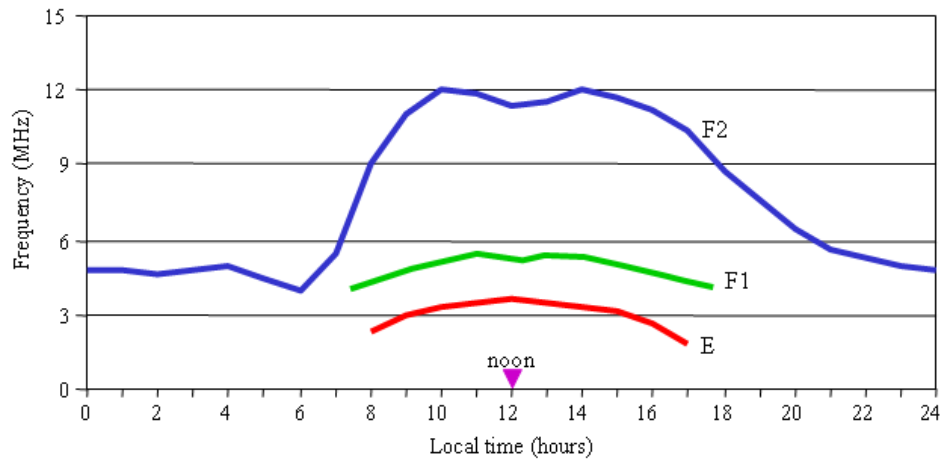


Figure 1.7: The wintertime daily variation of electron density over Canberra [1].

As seen in this figure, tracking the daily variation in solar radiation, D, E, F1 and F2 layers of ionosphere are observed during the day while only E and F layers are seen during the night. We can see that at this station, D, E and F1 layers disappear totally at night.

Figure 1.8 illustrates the latitudinal variation in electron density [1]. As seen in this sketch given, E layer (blue line) is seen at the low and mid latitudes and it mostly disappears over high latitudes above 60-70° during the daytime although this latitude limit also vary with solar and magnetospheric activity. As the sketch shows, E layer is not present at all latitudes during the night.

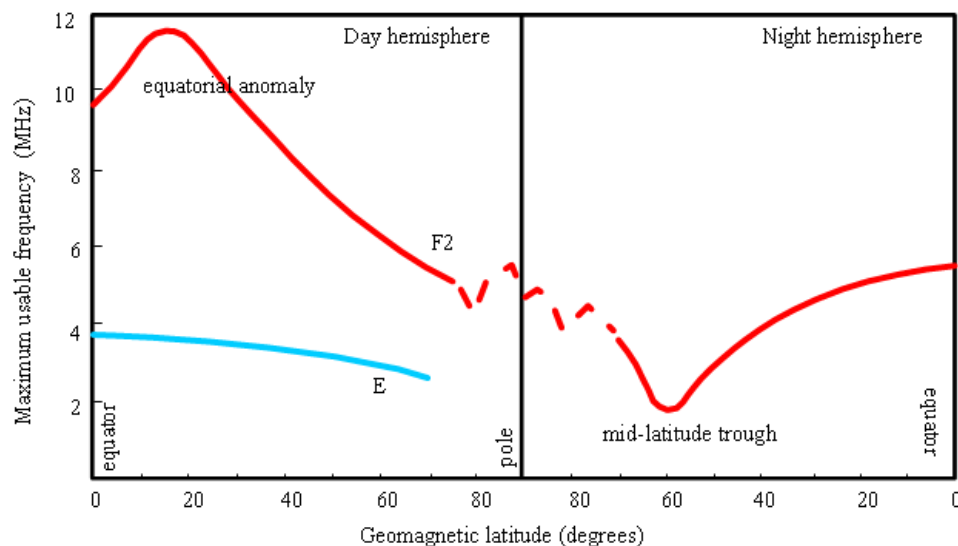


Figure 1.8: Sketch showing the latitudinal dependence of electron density at day (left) and night (right) [1].

In Figure 1.8, the electron density exhibits very different character at high, mid and low latitudes as especially because of the ionosphere-magnetosphere coupling. Specific structures and events are seen at different latitudes and during the day and night such as equatorial anomaly in the low latitudes, polar cap events at high latitudes, mid latitude trough and dusk phenomena at mid latitudes.

The solar and magnetospheric activities are the main cause of electron density other than solar radiation flux. Figure 1.9 demonstrates solar cycle variation in electron density over Canberra.

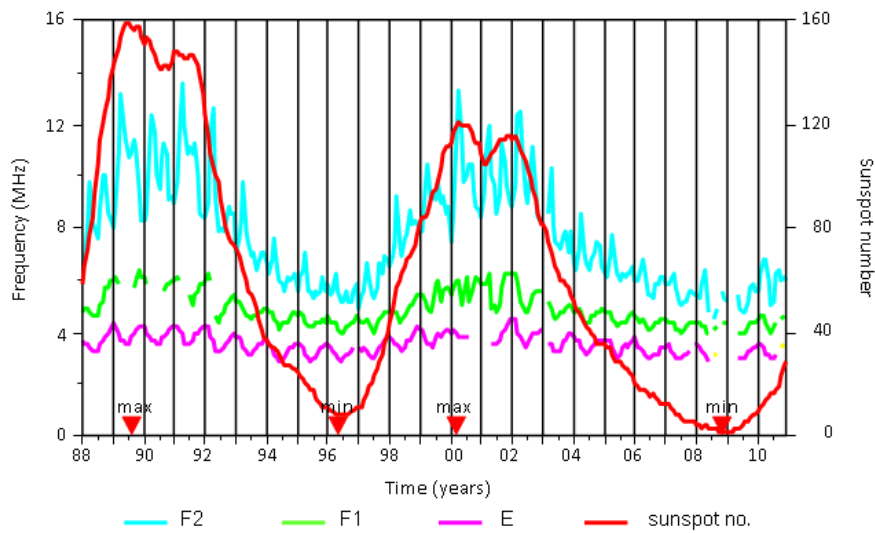


Figure 1.9: Solar cycle dependence of HF frequency waves over Canberra [1].

In the figure, red solid line is the number of sunspots showing two typical 11-year cycles and the scale is given on the right. The blue, green and pink colors give the variations at selected HF frequencies. As can be seen in the figure, HF frequencies become weaker during the low solar activity while they become stronger during the high solar activity so that the communications in these frequencies should be adjusted accordingly depending on the solar activity periods.

1.6 Ionospheric Observations

Current observations of the electron density of the ionosphere are made by:

1. using ionosonde
2. using incoherent scatter, such as EISCAT in Scandinavia
3. using coherent radars such as, that in Peru

4. using rockets
5. using satellites
6. referring from GPS signal delay

In this study, since we use ionosonde observations only ionosonde instrument described below:

Ionosondes are radars, which uses radio pulses to study the electron density of the ionosphere. The history of ionosondes goes back to 1925s. The principal components of any radar like ionosonde include the circuits or devices which:

1. define the signal to be transmitted
2. amplify the signal to a useful power level
3. radiate (as antennas) the signal generally upward and accept the down coming echoes
4. receive the signal (or 'echo'), by appropriate amplification, filtering and noise- rejection;
5. Record the echo information in some suitable form.

Unlike more familiar radars, the ionosonde does not attempt to direct its "beam" to locate its "target". Ionosonde antennas scan the "whole sky" between 1-20 MHz. The ionosphere is continuously tilted, wavy and irregular. These properties of the ionosphere determine the location (or locations) from which reflections occur [7]. Figure 1.10 illustrates an example of ionosonde, which sends a vertical beam.

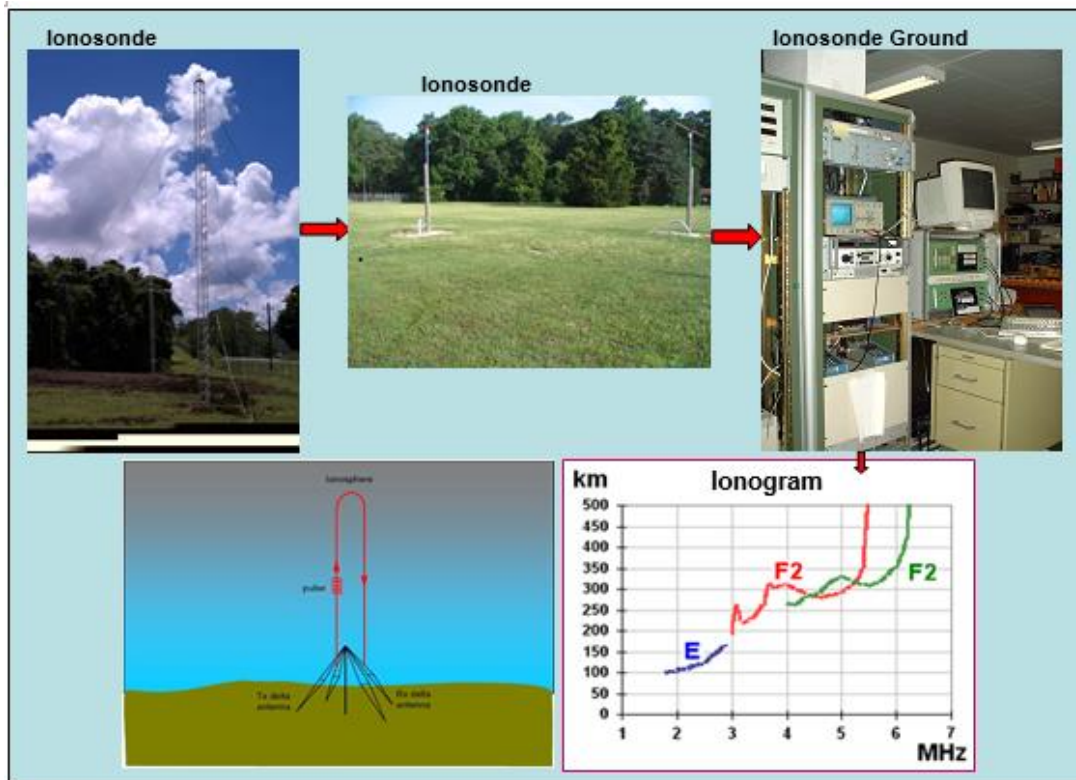


Figure 1.10: Components of an ionosonde (top row); transmitter, receiver and ground station. Virtual height concept and Ionogram are given at the bottom row [1].

Radio waves may be totally reflected in the ionosphere, giving strong echoes even with rather low transmitted power (a few kW). This is the fundamental principle of the 'ionosonde'. The ionospheric reflection process is strongly 'dispersive', or frequency-dependent, each frequency being reflected by one, two, or even three specific ionization densities, because the ionized plasma is 'magnetoactive'. Classical 'ionograms', simple graphs of signal travel time (a few milliseconds) vs radio frequency, directly display details of ionospheric structure. Figure 1.11 gives an example of real ionogram recorded in MileStone Hill observatory. They require only a little interpretive skill to recognize the usual stratification of the ionosphere, and to estimate the peak ionization densities. Estimation of the actual height of the ionosphere is difficult and requires extensive 'inversion' calculations [7].

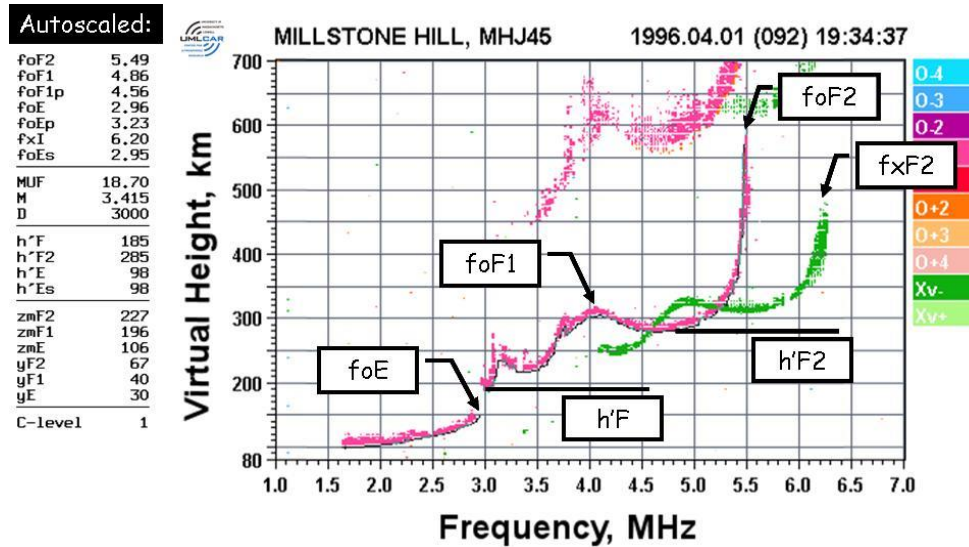


Figure 1.11: An example of a real ionogram [8].

1.7 Unusual Events in Ionosphere

1.7.1 Sporadic E

Sporadic E layer and spread F layer are two of the phenomena recorded by the ionosonde. Sporadic E occurs at altitudes ranging from about 90 to 140 km, that is, at E region altitudes. While the normal E region is controlled by solar EUV radiation, sporadic E is the result of wind shears, meteors and other phenomena. Sporadic E may form day or night and tends to appear for a few hours then disperse. The horizontal extent of sporadic E is probably of the order of tens to a few hundreds of kilometers with a vertical depth of a few kilometers. Sporadic E is illustrated in Figure 1.12.

The E region has an electron density that increases in the morning hours and decreases after noon. While sporadic E occurs at the same altitudes, it can often have far greater electron density than the E region, and at times, the F region. Such high electron density allows sporadic E to refract quite high frequencies as seen Figure 1.12. On oblique paths, sporadic E with high electron density may cause the radio wave to be refracted from it rather than the higher F region. This in turn can alter the location that the radio signal is received at the ground [1].

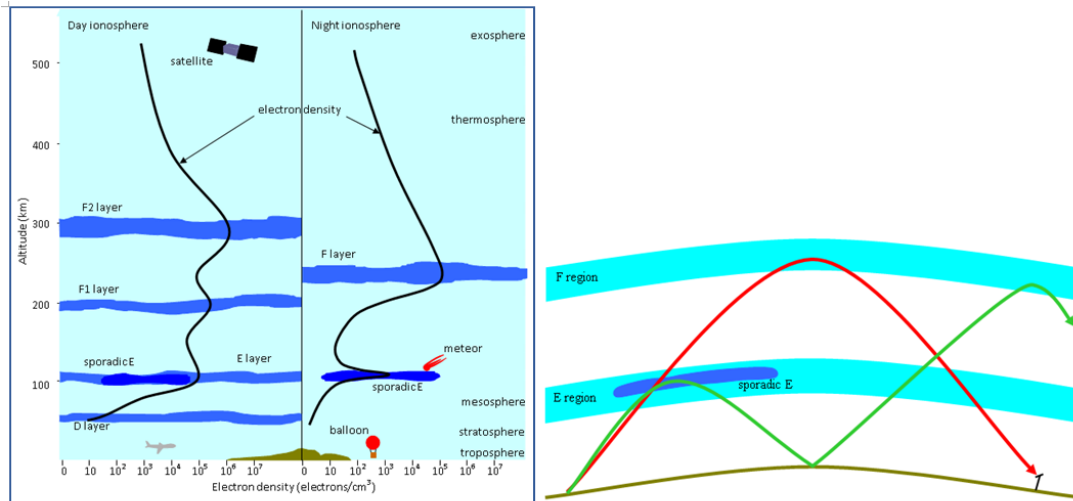


Figure 1.12: Illustration of Sporadic E layer [1].

1.7.2 Spread F

Spread F, on the other hand, is caused by electron density irregularities in the F2 region. The irregularities may last minutes to hours with a horizontal extent of a few to hundreds of kilometers. These irregularities distort signals passing through the affected region causing flutter fading on HF and scintillation (variations in signal strength and time of arrival) on higher frequencies used for ground-to-satellite communications. Figure 1.13 illustrates the spread F occurrence and its effect on signal propagation.

Spread F occurrence is greatest at night at all latitudes and at the equinoxes. At high latitudes, spread F can be prevalent during the day. Spread F occurs least at mid-latitudes. At all latitudes, there is a tendency for spread F to occur when there is a decrease in F region frequencies. That is, spread F is often associated with ionospheric storms [1]

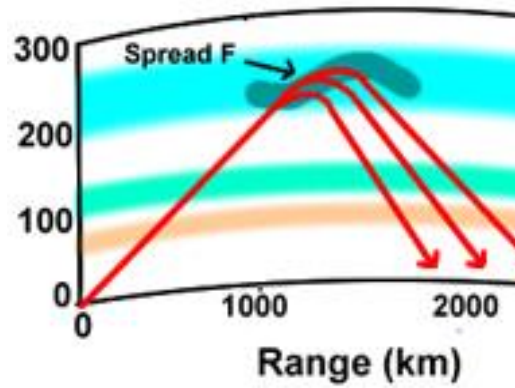


Figure 1.13: Illustration of Spread F [1].

1.7.3 Sudden ionospheric disturbances

Sudden Ionospheric Disturbance (SID) is a sudden increase in ionization in the D region of the ionosphere caused by a solar flare or gamma ray bursts. When a solar flare occurs on the Sun, intense ultraviolet and x-ray radiation from the flares intercepts the dayside of the Earth after a propagation time of about 8 minutes. This high-energy radiation absorbed by atmospheric particles immediately increases the electron density of the lower ionospheric layers over the entire dayside. The sudden increase in electron density will increase the radio wave absorption, especially in the upper MF (300 kHz - 3 MHz) and lower HF (3MHz - 30 MHz) ranges, and as a result often interrupts or interferes with telecommunications systems causing radio blackouts. For VLF (3 kHz - 30 kHz) waves, the reflection coefficient will increase which will cause a stronger reflection from the bottom of the D layer. Due to interferences between ground wave (direct propagation) and reflected by the D-layer, the VLF signal strength can increase or decrease during a SID event. As soon as the event ends, the SID and radio blackout end as the electrons in the D-layer recombine and signal strengths return to normal. Scientists on the ground can use this enhancement to detect solar flares by monitoring the signal strength of a distant VLF transmitter. It is thus possible to detect SIDs by monitoring the variations or the signal level of a distant VLF receiver. Therefore, variations in VLF strength can be used both indicators for the occurrence of solar flares and also for detecting the SIDs and monitoring the state of the lower ionospheric layer, i.e. variations in the D layer [9-10],

1.7.4 Travelling ionospheric disturbances and gravity waves

Another effect that causes variations in the electron density comes from the lower atmosphere. Even during the geomagnetically quiet (undisturbed) days, ionosphere can show variations in response to the passage of a gravity wave driven from the lower atmosphere, troposphere [14].

Gravity waves are the perturbations created in the lower atmosphere and propagated to the upper atmosphere above heights of 100 kms where they deposit their energy by wave breaking. They are also called buoyancy waves. They may be caused by the flow over mountain, Kelvin-Helmholtz instability, and flow over a convective cloud, and as a result of geostrophic adjustment in the lower atmosphere. These waves can propagate both vertically and horizontally from their source to sink. Their wavelengths vary from 10s to 1000s kms and their periodicity is on the order of minutes to hours. Typical wavelength in the mesospheric height at about 70-80kms is 2-3 km to 30km. Waves propagate vertically into the stratosphere and mesosphere. Wave amplitudes vary as $\rho^{-1/2}$ density decreases so waves grow in amplitude with height. Waves can be dissipated when their phase speed matches background wind speed. Gravity waves transport momentum vertically. This momentum transfer is crucial to the large-scale momentum balance of the stratosphere (10-50 km) and mesosphere (50-85km) [15].

Gravity waves in the ionosphere are detected as Travelling Ionospheric Disturbances (TIDs). TIDs are wave-like structures seen in the ionospheric plasma density, in the mid-latitude ionosphere, TIDs have been observed by using various techniques [16]. TIDs have been believed to be an ionospheric manifestation of atmospheric gravity waves caused by geomagnetic activity at high latitude and/or propagated from the lower atmosphere. TIDs may have horizontal wavelengths of 100–250 km which are classified as medium-scale TIDs (MSTIDs) [17].

1.7.5 Solar Activity

The conditions on the Sun cause variations on the electromagnetic radiation at different levels. When solar flares and Coronal Mass Ejections (CME's) occur, strong hard rays, extreme ultra-violet (UV) radiation, energetic particles from the

Sun released from the Sun. The Sun provides the radiation that governs the state of the ionosphere and thus affects the radio propagation. Under some circumstances, these can enhance radio communications and the HF radio propagation conditions while under other circumstances they can disrupt radio communications on the HF bands. However, at the same time they can also provide some radio propagation conditions that can be used at VHF by radio amateurs. Therefore, the occurrence of flares or other disturbances and their predictions are very important to assess on the state of the ionosphere for a successful radio communication.

1.7.5.1 Solar flares

Solar flares are explosions that occur on the surface of the Sun. They release large amounts of energy at the very short wave band of the electromagnetic spectrum and energetic high-speed protons. Flares are not predictable and erupt in just a few minutes. This leaves no time for the human to get prepared for its consequences. They occur as a result of magnetic reconnection thus the material is heated to millions of degrees Celsius. Flares generally last for about an hour. The flares affect radio propagation and radio communications on Earth and the effects may be noticed for some time afterwards. Flare occurrence correlate well with the sunspot cycle, increasing in number towards the peak of the 11-year sunspot cycle [12]. Figure 1.14 shows Sun in active time.

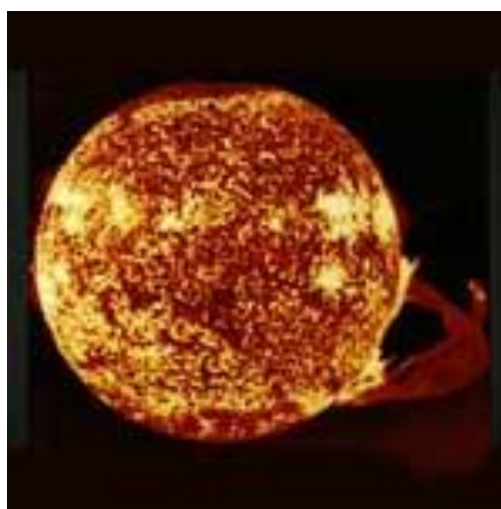


Figure 1.14: Active Sun [12].

Flares are classified by their intensity at X-ray wavelengths, i.e. wavelengths between 1 - 8 Angstroms. The X-Ray intensity from the Sun is continually monitored by the National Oceanic and Atmospheric Administration (NOAA) using detectors on some of its satellites. GOES satellite series are used to monitor the X-ray flux from the solar flares. By using this data, it is possible to classify the flares. The largest flares are termed X-Class flares. M-Class flares are smaller, having a tenth the X-Ray intensity of the X-Class ones. C-Class flares then have a tenth the intensity of the M-Class ones. Table 1.3 below gives the classification of the solar flares according to their intensity [11].

Table 1.3: Solar flare classifications.

Class	Peak (W/m^2) between 1 and 8 Angstroms
B	$I < 10^{-6}$
C	$10^{-6} < I < 10^{-5}$
M	$10^{-5} < I < 10^{-4}$
X	$I \geq 10^{-4}$

Below sketch (Figure 1.15) summarizes the effects on the radio wave propagation.

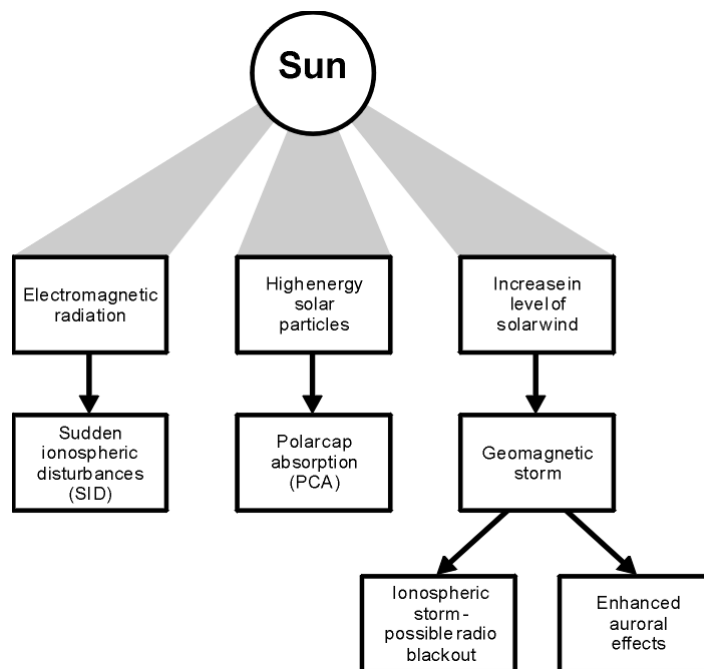


Figure 1.15: Effects of radio wave propagation [13].

1.8 Purpose of the Thesis

In this thesis, we study the variations in the electron density using VLF signals recorded by a SID monitor and HF variations recorded by ionosonde both which are at Istanbul technical University campus. We first drive the general structure of the variations and then we study the specific events, solar activity and substorm dependence with selected Cases. We both study the temporal variations over Istanbul and also the vertical profiles of the electron density. We compare our results with the available ionospheric models such as IRI and TIEGCM. We then give discussion on the observed variability of the electron density over Istanbul, a mid-latitude station.

In Chapter-1, we introduce general information on ionosphere. In Chapter 2, we explain SID-VLF system in ITU data descriptions. Chapter 3 contains the results from SID-VLF data. In Chapter 4, has the summary of the results of SID-VLF data. We introduce HF radar and the data recorded in Chapter 5. Chapter 6 presents the results from Dynasonde radar data and introduces the models and presents the results from the models and comparisons with Dynasonde radar. Final chapter, Chapter 7, gives discussions on the results obtained and ends with suggestions and future works.

2. SUDDEN IONOSPHERIC DISTURBANCES (SIDS) AND VLF WAVES

Sudden Ionospheric Disturbances (SIDs) are abnormally high ionization/plasma density regions/structures in the D region of the ionosphere caused by a solar flare. SIDs are often observed in the HF or short wave bands. They cause absorptions of the HF signals and as a result often interrupt or interfere with telecommunications systems. Therefore, they are sometimes called as blackouts or short wave fades (SWF). SID events occur suddenly and last for a few hours. As a result, they cause collapses in ionospheric radio propagation for a number of hours as well. The blackout can cover part, or all of the HF radio spectrum depending on the strength of the events. SID may only last for a few hours, however, they may be a precursor for a longer blackout. Generally a SID is caused by a large solar flare. Along with the flare, the level of radiation that is emitted by the Sun increases as well. It takes about 8 minutes for the radiation from the Sun to reach the Earth. As soon as the radiation reaches the Earth, the effects start to be noticed and the SID begins. Because the timing is very short, there is no time to warn about the events prior to their occurrence [18].

The solar radiation covers all ranges of electromagnetic waves including the X-Rays as seen in Figure 1.3 in Chapter 1. The X-rays, especially intense hard X-rays have the ability to penetrate through to the D layer or D region of the ionosphere. As a result, high levels of X-rays give rise to a high level of ionization in the D region. The ionization by solar flares becomes the dominant ionization source exceeding the other means of ionization in lower ionosphere. The result of this additional ionization is not only the increase of electron concentration, but also the change of the ionization height of the D layer [19]. The electron density can increase by up to two orders of magnitude and the lower edge of D layer can decrease by a few kilometers [20]. Both of these effects increase the D region absorption and attenuation of the radio waves significantly and change the characteristics of VLF waves.

Although the increase in the level of radiation is rapid, it takes time for the level of ionization to rise. As a result, in the electromagnetic spectrum, the lower frequencies

are affected first. As the degree of ionization in D layer increases, the higher frequencies are affected as well. During a normal day, the D region normally affects frequencies up to two or three MHz, but the increase in radiation from a flare can cause much higher frequencies to be affected. Often it can result in a complete black out of the HF bands. At other times, a SID may only affect the lower frequencies [18].

There are a number of other side effects that may be noticed, especially at the onset of a Sudden Ionospheric Disturbance, SID. The D region is affected by the large increase in X-rays, but other forms of radiation, including ultra-violet also increase in intensity. This gives rise to an increase in the degree of ionization in the higher regions of the ionosphere. This can result in an increase in the maximum usable frequency, especially at the beginning of a radio blackout when the D region attenuation is not as high.

The duration of a SID event last only a few hours. As recovery starts, the high frequencies are affected first. After the flare, as the level of radiation falls, D region ionization decreases as well. As its intensity falls, this will affect the higher frequencies less, and HF propagation conditions will slowly return to normal.

Since the D layer is present only during the day, SIDs only affect only the dayside of the Earth. Areas in nightside when the flare occurred do not experience the effects of the effects [18].

An indirect way of studying the SIDs, thus the effects of the solar flares, is to use the variations in VLF waves typically in 10-100 kHz radio band. Monitoring a strong and stable signal from a fairly distant radio station and recording the variations in emissions in time provides a permanent monitoring of the solar flares and the SIDs.

Figure 2.1 shows an illustration of VLF propagation.

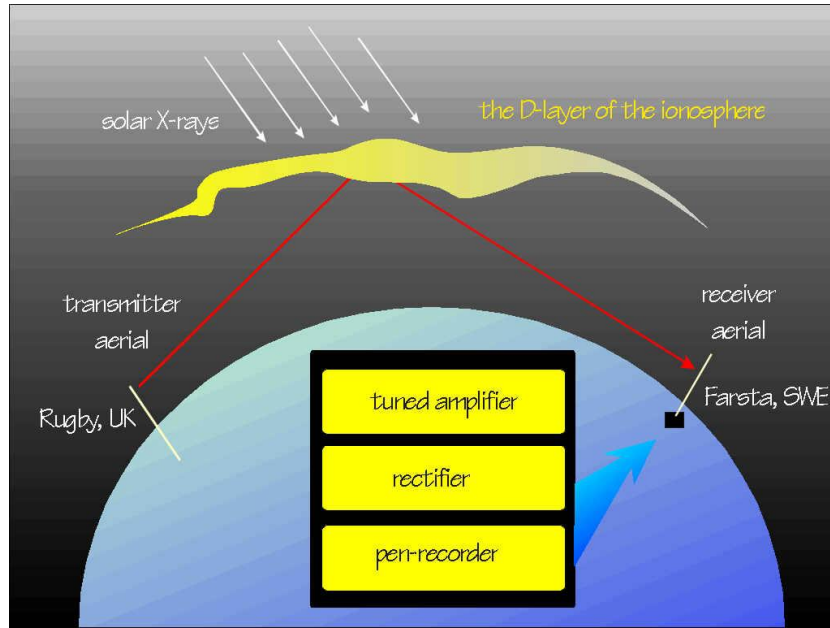


Figure 2.1: Illustration of VLF propagation in the presence of solar glare and increased ionization in D layer [21].

As mentioned in Chapter 1 the VLF signals are strongly reflected from the bottom of the ionosphere, which is the D layer, during the day owing to the increased ionization as a result of X-rays from the solar flares. Figure 2.2 below illustrates the day (right) and night (left) propagation of a VLF wave sent from a VLF transmitter. Chapter 1 provides detailed background information about VLF waves and their basic properties. Here we give how we can use VLF measurements to study the ionosphere, specifically the SIDs.

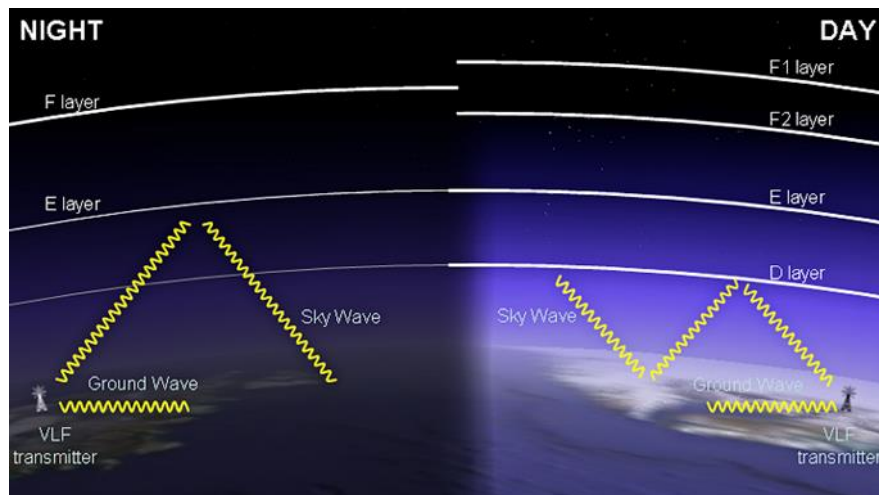


Figure 2.2: VLF propagation under the day (right) and night (left) ionospheric conditions.

VLF transmitters distributed over the globe are used to send VLF signals to the ionosphere, which are received by stations with VLF receivers. These stations record the reflected VLF signals and interpret the variations in signal strength. Figure 2.3 gives the distribution of the VLF transmitter around the globe while Table 2.1 lists the stations and their characteristics. Most of the transmitters are located in Europe. There is one station in Bafa, Turkey that uses VLF frequency at 26.7 kHz.

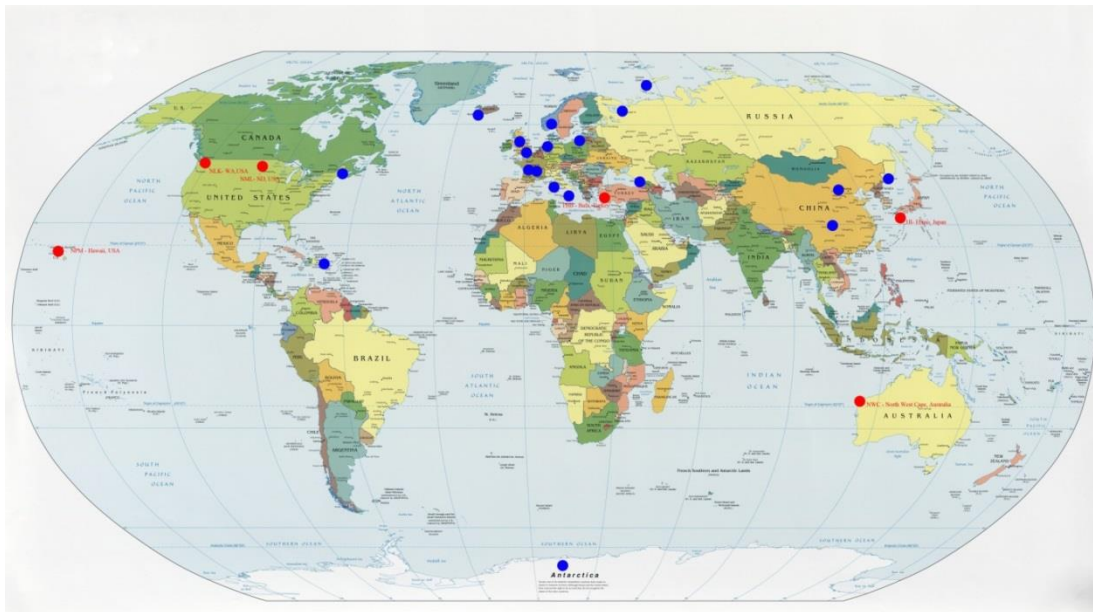


Figure 2.3: Distribution of the stations with VLF transmitter over the globe. Red circles indicate the transmitter sites used to monitor the ionosphere at ITU SID station.

Table 2.1: Characteristics of the VLF signals transmitted by the VLF stations seen in Figure 2.2. The highlighted cells indicates the stations that ITU VLF station records.

Country	Location	Name	Frequency	Power(kHz)	Latitude	Longitude
USA	Cutler, ME	NAA	24.0	1000	44.65N	-67.3W
	Jun Creek, WA	NLK	24.8	250	48.2N	-121.92W
	Lualualei, HI	NPM	21.4	566	20.4N	-158.2W
	LaMoure, ND	NML	25.2	500	46.35N	-98.33W
	Aquada, Puerto Rico	NAU	40.75	100	18.4N	-67.18W
Antarctica	South Pole	VLF	20.0			
Australia	North West Cape	NWC	19.8	1000	-21.8S	114.2E
China	Changde	3SA	20.6		25.03N	11.67E
	Datong	3SB	10.6		35.6N	103.33E
France	Rosnay	HWU	20.9	400	40.7N	1.25E
	St.Assie	FTA	16.8			
	LeBlanc (NATO)	HWV	21.75		40.7N	1.25E
Germany	Rhauderfehn	DHO	23.4	500	53.1N	7.33E
Iceland	Keflavik (US Navy)	NRK	37.5	100	65N	18W
	Keflavik	TFK	37.5			
India	Katabomman	VTX3	18.2		8.47N	77.4E
Italy	Tavolara	ICV	20.27	43	40.88N	9.68E
	Sicily	NSC	45.9		38N	13.5E
Japan	Ebino	JJI	22.2		32.04N	130.81E
Norway	Kolsas	JXN	16.4	45	59.51N	10.52E
Russia	Arkhangelsk	UGE	19.7	150 input	64.24N	41.32E
	Batumi	UVA	14.6	100 input		
	Kaliningrad	UGKZ	30.3	100 input		
	Matotchkhinchar	UFQE	18.1	100 input		
	Vladivostok	UIK	15.0	100 input		
Turkey	Bafa	TBB	26.7		37.3N	27.55E
UK	Anthorn	GBZ	19.6	500	52.71N	3.07W
	Anthorn (NATO)	GQD	22.1	500	52.4N	1.2W
	London	GYA	21.37	120	51N	2E

The VLF signals are recorded by a relatively small and fairly economical VLF receiver called SID monitors or AAVSO instruments, which are provided by Stanford University. Space Weather Monitor of Stanford University is essentially a VLF radio receiver. Instead of decoding the VLF signal, SID monitors measures the change in the signal strength itself. Two main scientific goals of the SID Monitor are 1-) For daytime data, to find out the reasons and effects of solar activity and to reach the ability to predict it on the Earth and 2-) For nighttime data, to understand the relationship between troposphere, mesosphere and ionosphere ruled by lightning and thunderstorm processes [22]. SID monitor distributed by Stanford University Solar Center, USA is given in Figure 2.4.



Figure 2.4: SID Monitor to detect the solar flare effects on ionospheric D-region [22].

2.1 SIDs as Seen in VLF Signals

Below, we present several examples of SID detected in VLF signals. Since SIDs are results of intense X-ray flux in the D region of the ionosphere, these signals indicate the presence of the solar flares on the Sun.

Figure 2.5 illustrates a typical example of daily variation of VLF signal power recorded with Stanford SID monitor, when there is not any solar flare activity on the Sun [22]. With no disturbance in ionosphere, power output of the monitor at nighttime must be higher than daytime values. During sunrise and sunset, there usually exists a bipolar fluctuation, which indicates the signature of sunrise and sunset times

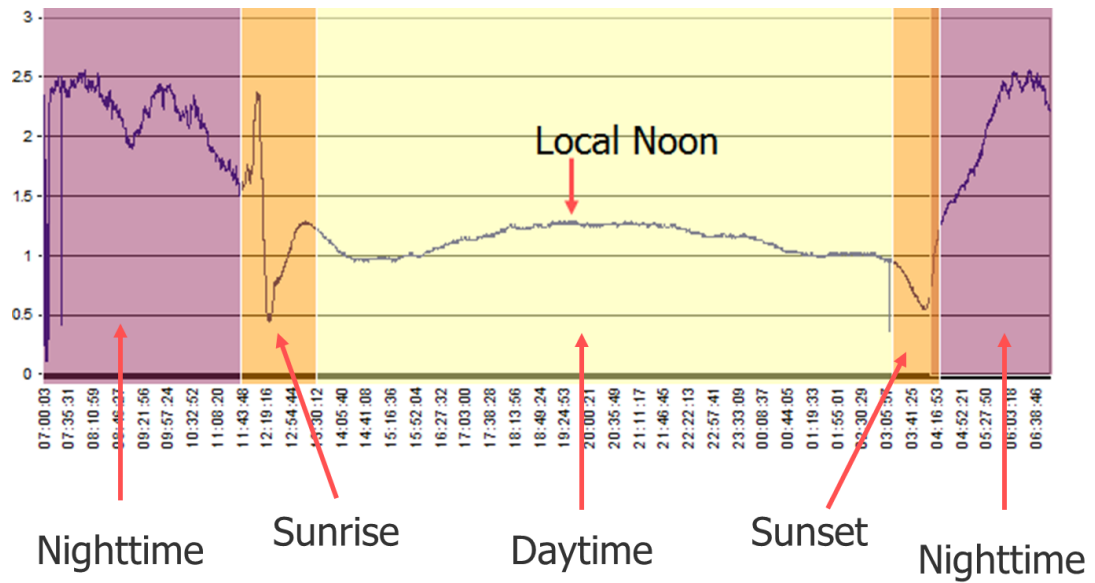


Figure 2.5: An example of daily variation of SID data for quiet conditions [22].

On the other hand, Figure 2.6 gives an example of SID detected in VLF signals [18].

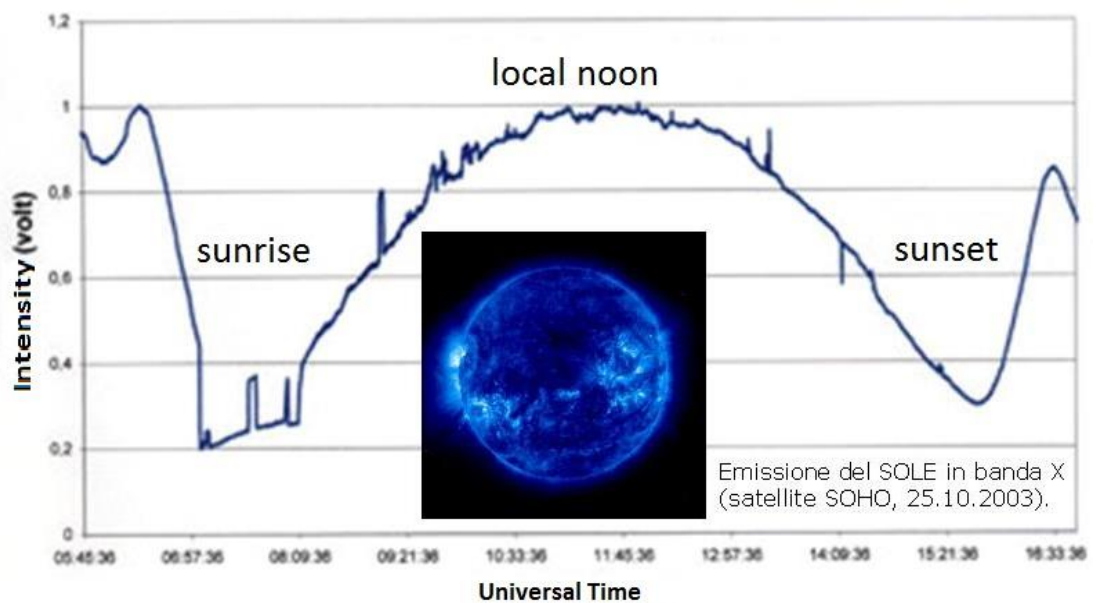


Figure 2.6: Daily typical VLF recording of SID events with an active Sun picture [22].

Significant characteristics of this VLF recording in Figure 2.6 is the presence of a maximum in the intensity of the signal received during the central hours of the day, minimum during the rise and fall of the sun, with a high signal level during the night. When there are solar flares with intense X-ray flux discharge during the day, typical daily curve overlap spikes (SIDs) with amplitude and duration that are directly related to the intensity of the phenomenon [23].

Another example plot of VLF that reflects effects of solar flares and thus occurrence of SID is given in Figure 2.7 [22]. The intensifications during solar flares in power strength overlapped on undisturbed daily variation. These power intensifications in VLF signal are correlated with the flares. In the figure, the type of the solar flares are also indicated. Solar flares are classified according to their flux released into the space. The C, B, M and X are the types of the solar flares which are currently used. X shows the strongest flare while C indicates the weakest. The corresponding solar flare flux is taken from GOES spacecraft at the geosynchronous orbit. The small rectangular inlet, with red and blue lines in the figure gives the shortwave and longwave flux during the solar flares respectively.

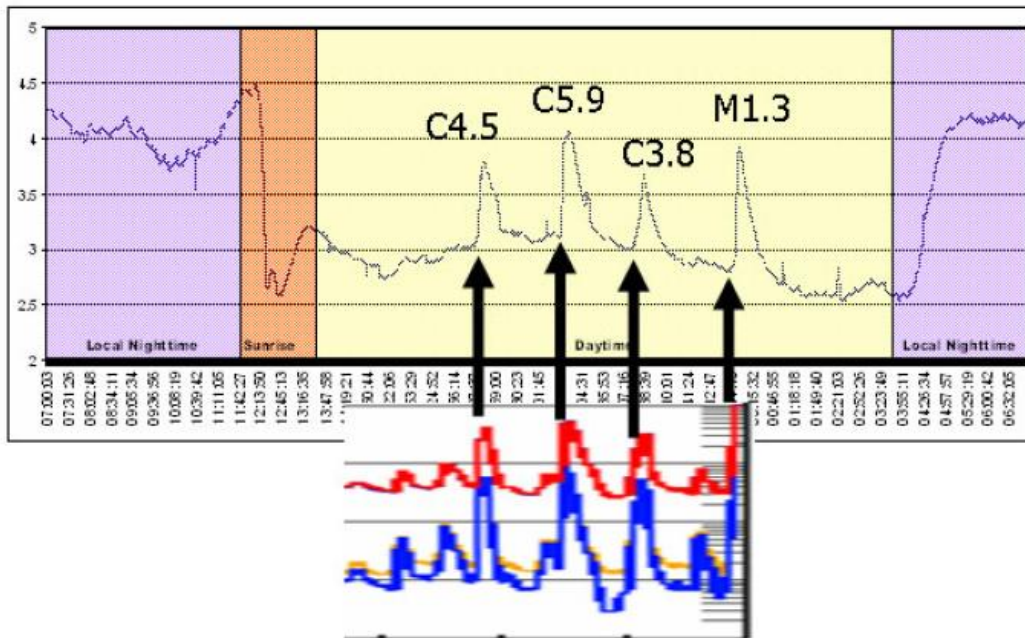


Figure 2.7: An example of SID data for disturbed conditions with solar flare association[22].

VLF recordings can also be used to refer to the occurrence of lightning, especially during the nighttime. The VLF recording given in Figure 2.8 gives an example of such recording. The spikes shown by red arrows indicate the lightning signatures in the VLF data.

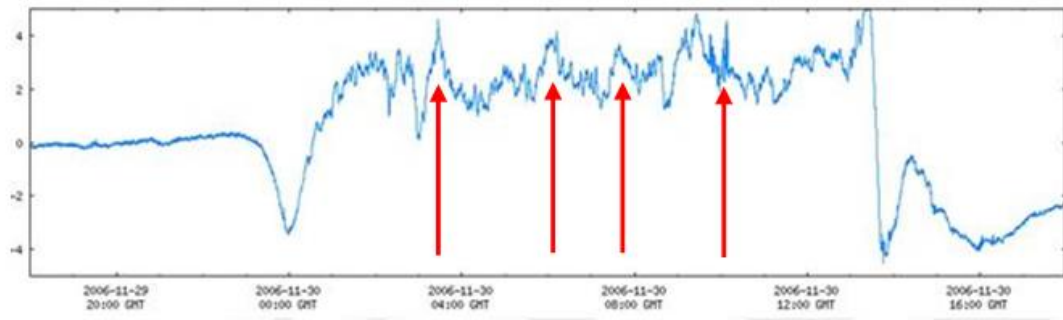


Figure 2.8: An example of VLF data showing lightning signatures (red arrows)[22].

In this part of our study, we use VLF data to investigate the SID/Solar flare signatures recorded with Stanford SID-VLF Monitor instrument at ITU, Upper Atmosphere and Space Weather Laboratory. The lightning events are reserved for a further research and not included here.

2.2 Literature on SID and VLF Relation

The studies of SID using VLF waves do not go as much back long in the history of the radars, and in the analysis of the behavior of the ionosphere. In this part, we will give some closest examples from the conducted studies in the literature on this subject.

Thomson and Cliverd used VLF signals recorded in Cambridge, UK (52°11' N, 0°2'W) from a transmitter with frequency at 18.3 kHz in France. They analyzed the height of the D region electron density characterized by H' and electron density gradient β . They showed that the solar flare induced changes in the electron densities and VLF reflection height in the D region have quantitatively related to the intensity of the X ray flux from the solar flares. They further showed that the increased ionization from the flare decreases the effective reflecting height of the D region in proportion with the logarithm of the X-ray flare intensity. They found that the flares also significantly increase the gradient or the sharpness of the lower edge of the D region. The sharper the boundary, i.e. the higher the β , the less the attenuation occurs, causing a mirror reflection in VLF waves. During the normal, unperturbed conditions, early or late in the day, or at solar minimum, the lower edge of the D region is determined by the background ionization mostly driven by the solar radiation alone. This results in a lower sharpness in electron density profile and thus resulting in a higher attenuation of VLF signal. When the X-rays from a

significant solar flare arrive, they become the dominant source of ionization in D region and thus produce a sharper profile and less attenuation [19].

Grubor et al analyzed the VLF amplitudes and phase delays recorded at their station in Belgrade, Serbia for six VLF ranges below frequencies 30 kHz. For their analysis, they picked the signal transmitted from Anthora, UK at the frequency of 22.1 kHz. They carried out a detailed correlative study with the solar flares using GOES X-ray flux data and determined the effects of the flares on the propagation characteristics of VLF waves. The results of their analysis brought out the solar flare characteristics as observed by the VLF signatures, and physical mechanisms behind the variations in the D layer ionosphere. They showed that the responses in the VLF amplitude and phase delay are very different for each type of solar flare from the Sun, sketched the outline of the each VLF signal response recorded, and discussed the associated process behind them. Their findings may be summarized as follows [24]:

1. The small decreases of the VLF signal amplitude, caused by C class flares are due to the deviative absorption of wave energy in the D region. Namely, the VLF wave penetrates into the D region in which the ionization by X-ray burst slightly increases the electron concentration. In this case, due to slightly increased ionization as the reflection points of the wave is located higher up within the D region, the wave takes a longer path before they reflect compared to the undisturbed conditions. This is called deviative reflection.
2. As the X-ray flux increases both the electron density in the medium (D-layer) increases and also the electron redistribution with height occurs. In this case, the height of the reflection point decreases and the reflection point of VLF waves occurs at a sharp boundary even before the wave enters the ionosphere. This is called mirror reflection.
3. Transition from deviative reflection to the mirror reflection happens in a few minutes. This is controlled by the X-ray flux to reach a certain value before the wave mirror reflects. This value ranges from 5×10^{-6} to 10^{-5} W/m². Therefore, the C5 to M1 class flares cause the drop of VLF signal amplitude to the minimum in first few minutes (due to deviative absorption), followed by the rise of the amplitude to a small peak (due to the mirror reflection), delayed few minutes after the peak X-ray irradiance. Decreasing of the X-ray

flux causes ascending and diminishing of the sharp boundary, allowing the penetration of the wave deeper into the D region. The deviate absorption occurs again and the value of amplitude decreases to the second minimum.

4. The variation of amplitude during the flare as described above, generally holds for greater M class flares and for X class flares. The greater the X ray peak flux, the higher the amplitude peak above the level of regular diurnal value. If the peak X ray flux approaches 10^{-3} W/m^2 , the amplitude change is pure positive.
5. If the X class solar flare occurs at high solar zenith angle with respect to the mid-point of the VLF wave trace (dusk or dawn hours), the effect on the VLF signal amplitude will be negative. Namely, the electron concentration even if increased by X ray ionization, is still insufficient to form the sharp upper boundary at a low altitude within the D layer. Therefore, the deviative absorption of VLF wave takes place.

Another study on the VLF signatures of solar flares and their effects on D layer characteristics are carried by Sulic et al. [25]. They used the same VLF data as in [24] and studied effects of a solar flare and solar eclipse phenomena on VLF 22.1 kHz waves transmitted from Scotland, UK and recorded at Belgrade some 2000 km away. They showed that the flare and eclipse has opposite effects on electron density distribution in the ionosphere. During the flare event, the ionizing solar radiation is largely increased which results in higher electron concentrations and lowering of the wave reflection points in the D layer. A solar eclipse causes a reversed effect of a reduced ionization radiation resulting in lower electron densities and higher locations of radio wave reflection points in the D layer.

The results from these studies, the principal effect of a solar flare on the D region is that X-rays from the flare typically greatly increase the ionization rate at and below the height of the normal D region (~70 km). Thus, the effective height of the D region decreases. This motion of the bottom edge of the D layer toward the ground, i.e. towards the transmitter, causes a strong VLF signal at the receiver site.

These studies are good examples in demonstrating the relationship between the solar activity, VLF wave signatures and D layer characteristics. They clearly show the different characteristics of D layer under different solar conditions and VLF waves

constitute a good way of studying both the solar flares themselves and their ionospheric effects as well as how the ionosphere behaves under different solar conditions.

3. SID ANALYSIS USING VLF DATA RECORDED AT ITU SID MONITOR

3.1 ITU SID-VLF MONITOR

SID-VLF monitor (Figure 2.4) has been obtained from Stanford SID Monitor Center in June 2011. The VLF antenna shown in Figure 3.1 has been built by the members of the Upper Atmosphere and Space Weather Laboratory at ITU (Figure 3.2). It is located on the roof of ITU Astronautical & Aeronautical Faculty (40.58°N, 28.5°E).



Figure 3.1: ITU-SID antenna on the roof of the Astronautics and Aeronautics Faculty, ITU..

The antenna is recording VLF signals from six transmitting stations; which shows distinct signal power at our receiver site. These stations are shown in red circles in Figure 2.3. One of these stations locates in Bafa, Turkey, TBB, (41.1N, 29.0E), and transmitting at the frequency of 26.7 kHz. The system is operating and collecting data since June 2011. However, in this study, we analyzed one year of SID VLF

data. In addition to the VLF signal power data, X-ray flux data from GOES 15 satellite.



Figure 3.2: ITU-UASW Lab Group members performing the antenna setup: sitting from left to right are Doğa Can Su Öztürk, Zerefşan Kaymaz, Emine Ceren Kalafatoğlu Eyigüler, and İklim Gençtürk Akay (Photo taken by Ayşegül Ceren Moral).

The signals from the transmitter regions follow different paths in the ionosphere before they reach the receiver in Istanbul at ITU. Therefore, these signals present a good opportunity to study the electron density structure of the ionosphere in the vicinity of Istanbul. The amount of the absorption/attenuation of the VLF signal occurs strongly in the D region. The amount of absorption in the D region is closely related to the frequency of the transmitted signal, being inversely proportional with the square of the frequency, and the amount of electron density in the region, being positively correlated.

In this part of our study, we investigate the solar flare effects on VLF signals recorded at ITU SID station to derive the characteristic properties of D region and its behavior in response to the solar activity. Signals transmitted from six stations are recorded at ITU but only the signals from BAFA station will be presented in the following chapters.

3.2 Results From SID-VLF Observations

3.2.1 General structure

To determine the general variations in the VLF signals observed at ITU SID VLF station, more than two years of archived data were visually scanned. We used the VLF signals from BAFA station (37.3N, 27.25E) which transmit at frequency of 26.7 kHz. Figure 3.3 gives an example of the daily variation in our data set.

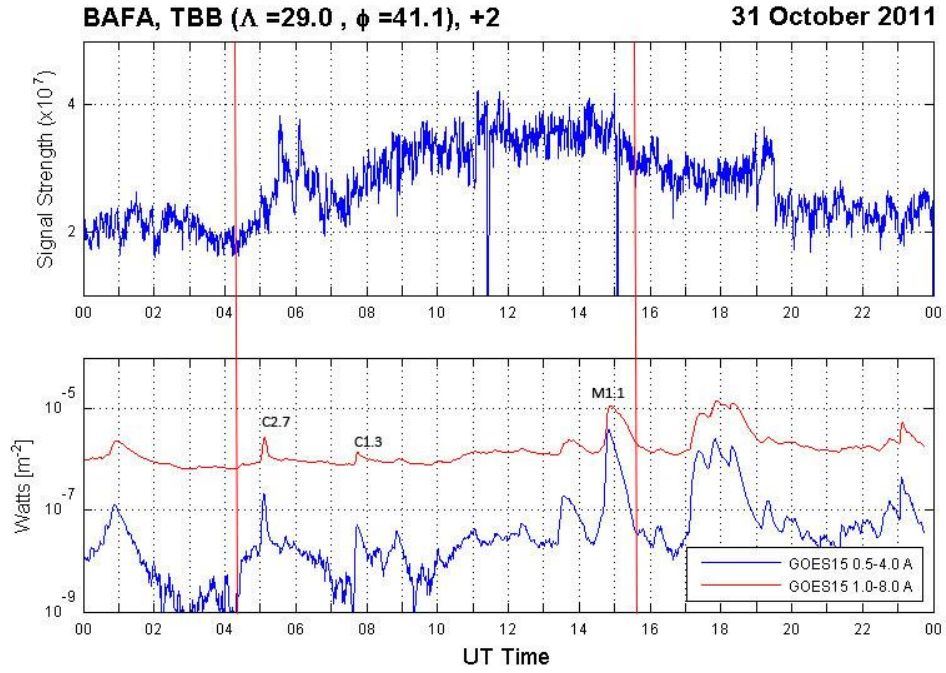


Figure 3.3: Top: An example of VLF recording from ITU station on the day of October 31, 2011. The signal transmitter is the BAFA VLF station. Bottom: GOES15 X-ray flux. Red lines indicate the sunrise (left) and sunset (right).

In the figure, horizontal axis is the time in UT and the vertical axis is the VLF strength received at ITU station. The signal strength is recorded in arbitrary units. We are mostly interested in determining the trends and carry out a qualitative analysis rather than the quantitative, therefore, the numbers on the vertical axis for the strength are not as important at this stage of our analysis. That is why we ignore the number at the vertical axis in many of our plots presented in this study. To obtain local time for this day, we need to add +2 to UT times given on the horizontal axis. We can see that the signal power is stronger during the day reaching its peak around noon times but decreases during evening and morning hours. Around the

dusk and dawn there seen to be increases in VLF strength as well. Except the dawn and dusk, the signal strength tracks the solar radiation curve. Nighttime variation is from the higher regions of the ionosphere, from E (100-150 km) and F regions (150-350 km) while the variations during the day are recorded in the presence of D layer.

If we examine the X ray flux data from GOES spacecraft, which is also given at the bottom of Figure 3.3, we can see that there are several C and M type solar flare events occurred at the same day on the Sun. If we closely examine the two figures, we can notice that the increases in VLF signal strength at various levels occurred at some delay after the flare occurrence. Dawn and dusk increases in strength seem to be happened after the solar flare.

Scanning through approximately two years of data, we determined four types of variations in the VLF signal strength. These variations are presented in Figure 25. Figure 3.4 shows these daily variations of VLF data corresponding to these four types. In the figure, horizontal axis gives the time of the day and the vertical axis shows the normalized signal strength. The variations in the upper left panel in Figure 3.4 follow again the solar radiation throughout the day in all months and seasons. As the Sun rises in the sky, VLF signal strength increases. It decreases as the Sun sets down during the evening hours and during the Sun set up in the morning hours. In the upper right panel of Figure 3.4, we see that the VLF signal show two shoulder type variation during the Sun rising and setting but a very low variation throughout the day. Lower left panel is similar to upper left panel but with a drop at noontime. The lower right panel presents a special structure with a wavy pattern after sunset.

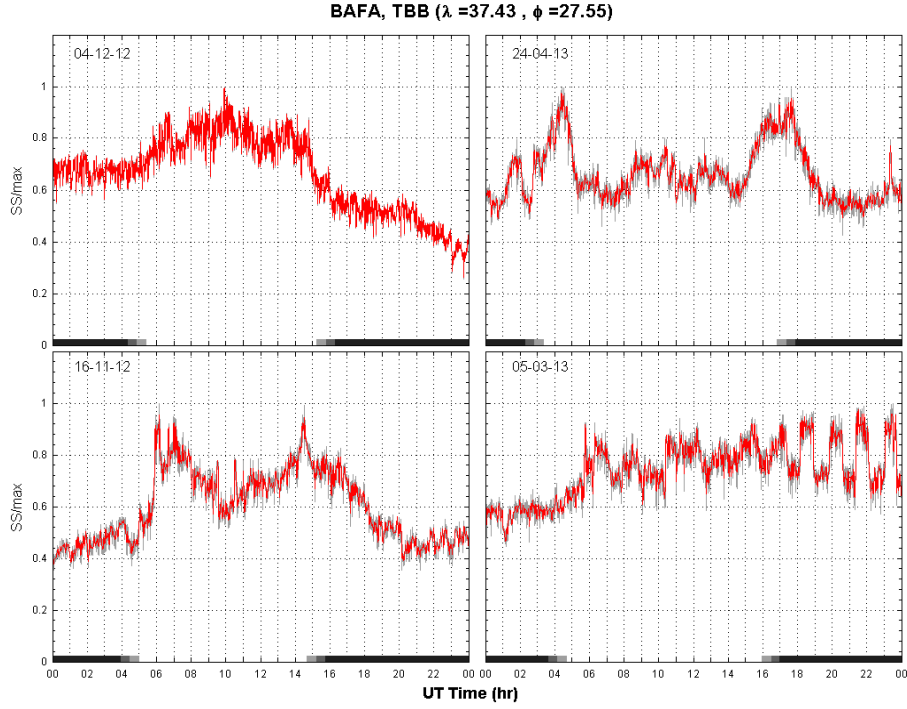


Figure 3.4: Four examples of VLF variations recorded at ITU SID station.
Transmitting station is BAFA, Turkey.

Figure 3.5 demonstrates the monthly variations in bar plots given for each month. The horizontal axis in the plots is the time of the day and the vertical axis is the normalized in signal strength according to daily maximum. Figure also illustrates the seasonal variations in VLF signals. The three panels from top to bottom on the most left give the months of June, July, and August from top to bottom and present the variations in Summer season; similarly September, October and November are presented in the next column from top to bottom and present the variations in Fall; then follow the Winter months, December, January and February from top to bottom. The most right panel gives the distributions in spring months March, April, and May from top to bottom. The data during the summer has a problem resulting from the transmission problems in Bafa. Therefore, it is not correct and reliable but it is included here in the figure for the completeness.

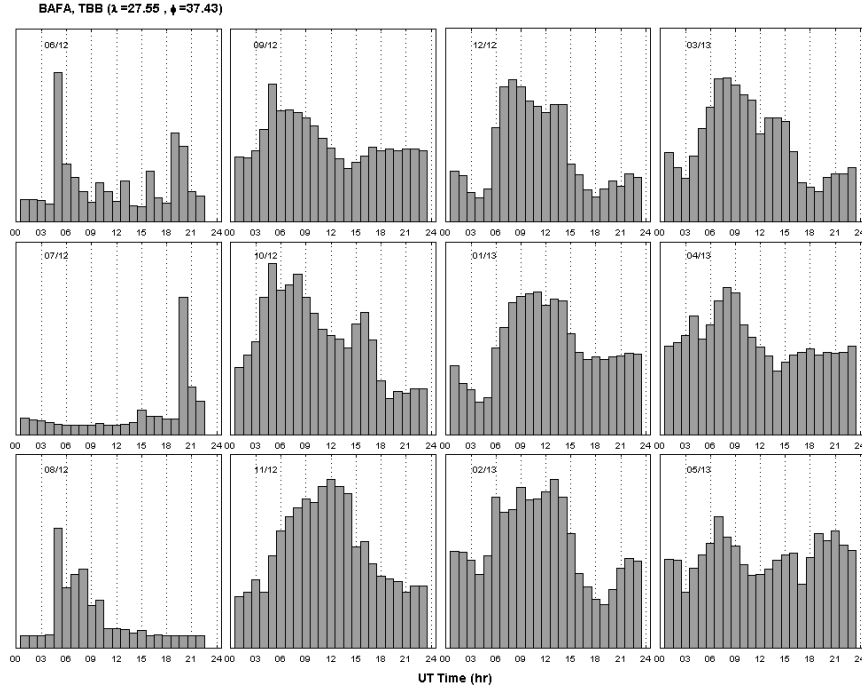


Figure 3.5: Monthly distributions of VLF signals transmitted from Bafa and received at ITU.

When the monthly panels in Figure 3.5 are examined, it is seen that some of the months exhibit a Gaussian type normal distribution (autumn months) but others present skewed Gaussian (winter months). Some of the months, especially autumn months, show a clear daily asymmetry skewed toward the morning hours. The signal strength during the sunset times are higher than the signal strength during the sunrise times. This reverses during the spring months. A second maximum in autumn months is seen in addition to the noon peak in signal strength. The lowest signal strength during the daytime is seen in spring months while the highest signal strength is recorded in autumn months. Clearly, the autumn months seem to be the most appropriate months to communicate with VLF waves during the daytime as the signal strength is higher compared to the those in other months. In addition, statistical properties for the data given in Figure 3.5 are given in Table 3.1 below.

Table 3.1: Statistical properties for the data given in Figure 3.5 .

		Mean $\times 10^{14}$	Median $\times 10^{14}$	Max $\times 10^{14}$	Min $\times 10^{14}$	Skewness
Summer	June	3.32	2.52	9.2	1.54	1.72
	July	5.83	5.53	9.66	1.28	-0.24
	August	2.74	2.16	8.52	1.08	2.65
Fall	September	1.83	1.75	2.43	1.55	1.23
	October	2.99	2.98	3.77	2.37	0.15
	November	8.52	8.35	9.59	7.86	0.38
Winter	December	7.81	8.52	9.83	1.01	-2.2
	January	3.88	1.15	9.95	1	0.76
	February	3.57	1.11	9.95	1.01	0.98
Spring	March	8.25	8.08	9.23	7.47	0.36
	April	5.38	5.25	6.35	4.79	1.19
	May	7.9	7.89	8.7	7.15	0.04

Figure 3.6 demonstrates the seasonal variations in VLF strength. The same problem exists with summer time data and thus we do not interpret the variations in summer. Here, we can see clearly that the distribution becomes skewed from winter, which exhibit more Gaussian distribution, towards spring season. The peak in strength is seen dispersed around 12 UT noon in spring. This noon peak seems to be shifted to 06 UT to the dawn in autumn and a second peak appears at around 18 UT in addition to peak at 06 UT. As in the previous figure, we find the lowest signal strength in spring and the highest in winter. Statistical properties of Figure 3.6 are given in Table 3.2.

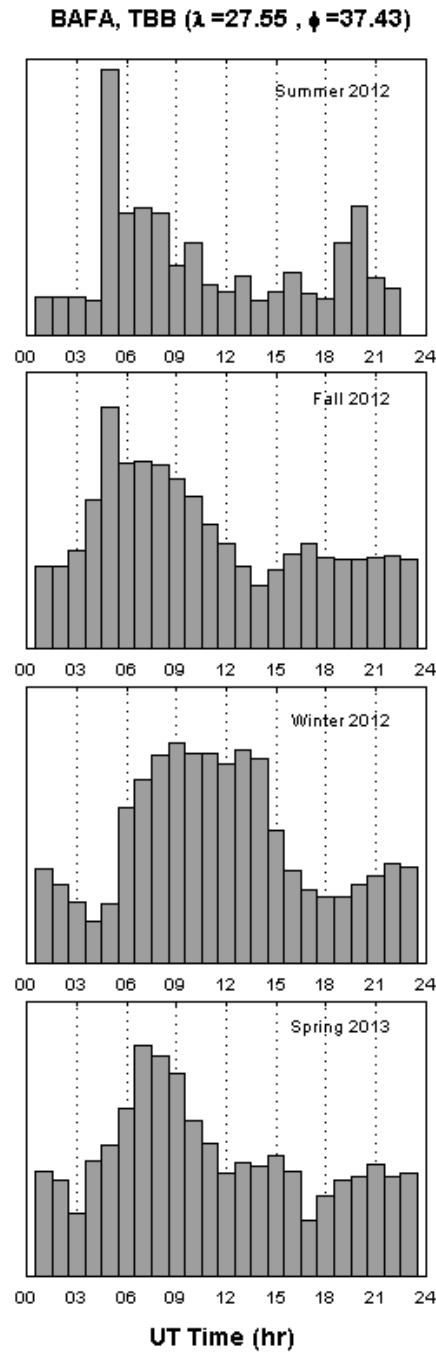


Figure 3.6: Seasonal variations of VLF data received at ITU VLF station of 1-year data.

Table 3.2: Statistical properties for the data given in Figure 3.6.

	Mean	Median	Max	Min	Skewness
	$\times 10^{14}$	$\times 10^{14}$	$\times 10^{14}$	$\times 10^{14}$	
Summer	2.86	2.19	6.03	1.23	1.15
Fall	7.1	6.68	9.35	6.14	1.25
Winter	6.27	9.18	9.96	1.02	-0.54
Spring	7.18	7.06	8.01	6.68	1.29

3.2.2 Effects of solar flare

Figure 3.7 gives an example where we observe the solar flare effect on the VLF signal strength on the day of October 17, 2012. The top panel is the VLF data while the panel at the bottom is the GOES 15 X-ray flux data. The red line shows the stronger x-ray flux and blue is the weaker x-ray flux. The degraded gray lines on the inner edge of the horizontal axis in the morning and evening times shows the sunlit part of the day when the Earth goes into night. Two peaks in X-ray flux are seen at about 06 UT (08 LT) and 08 UT (10 LT). We can also see an increased signal strength corresponding to these increases in X-ray flux. Actually, one can notice that during this day, the signal rate does not really tracks solar radiation. The peaks are found at dawn. We can also see a broader increase in signal strength from 14 UT to 18 UT during the evening. Although weaker, several small solar flares occurred during this period as well but none causes sharp rises in signal rate. Considering the fact that the broader peak in signal rate occurs around and after sunset makes one consider probably the cause is different from the solar radiation.

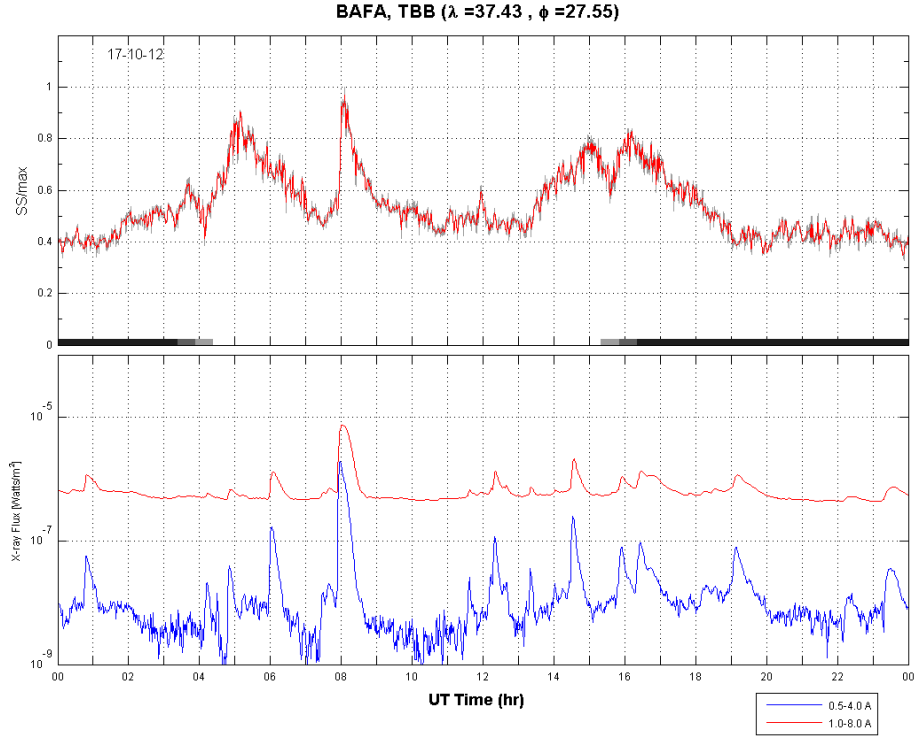


Figure 3.7: VLF signal strength (top) and the GOES 15 X-ray flux data (bottom).

Figure 3.8 shows an example of VLF data where we do not see any correspondence in solar flare occurrence. In this figure, solar flare is recorded at 13UT, but we do not find a corresponding increase or decrease in VLF data. This variation is very interesting were the VLF signal rate shows a large broader drop during the noontime at mid-day. Therefore two broader peaks appear at about 05 UT dawn a Local time and 15 UT dusk at local. There appears also though small, midday variations. These may be resulting from the local ionospheric dynamics in D region.

In Figure 3.9, there are four sudden sharp enhancements in SID-VLF data during the daytime with no association with solar flares.

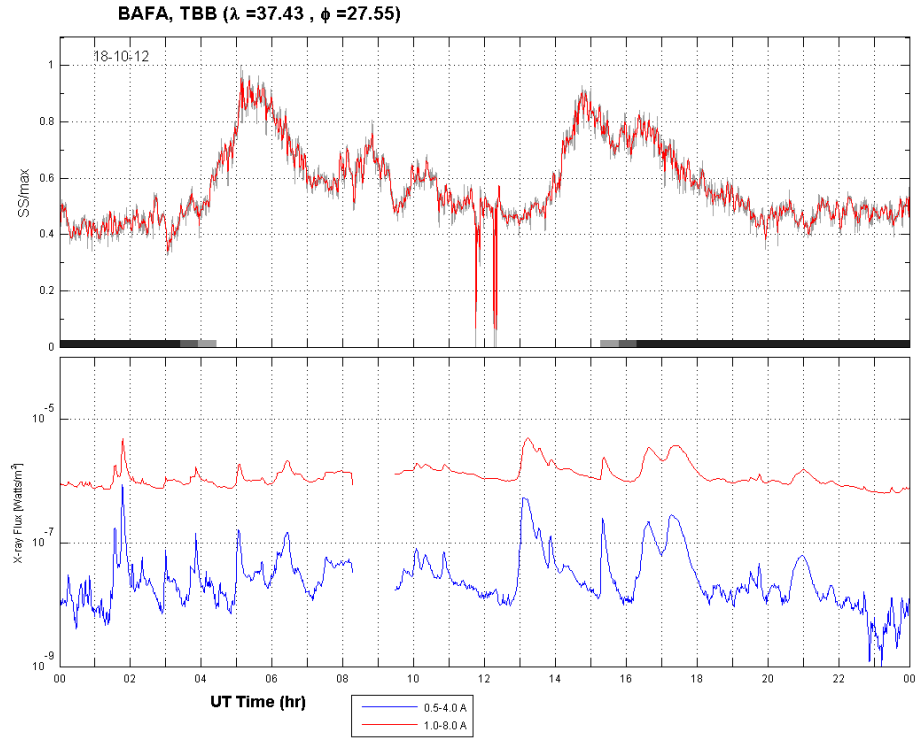


Figure 3.8: Top: Example of VLF data on 18th of October 2012. Bottom: Corresponding GOES 15 X ray flux data.

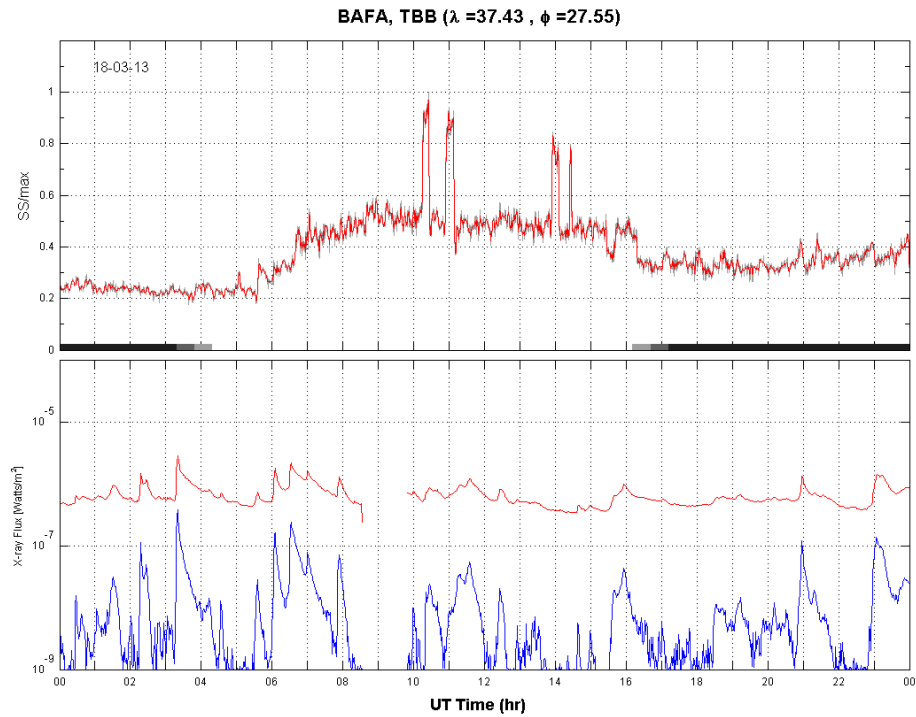


Figure 3.9: Example of ITU SID-VLF data on day March 18, 2013 with no solar flare association.

As seen from the examples above, the effects of solar flares in ITU-VLF data are not consistently and clearly observed. Sometimes even a small flare gives rise to a large increase while at others no relations were found. The reason behind this is not as clear at this time but is a detailed research subjected to a broader investigation and comparisons with the VLF data received at ITU SID from other transmitting stations at different geographical locations in order to conclude and sort out the effects from the solar flares. As the signal will follow a different path while reaching Istanbul from these stations, it may also point at different D region dynamics and may be help to sort out local variations.

3.2.3 Wave structures

Another type of variation observed in ITU VLF station transmitted from BAFA is the wavy structures seen through or part of the day. Most of the time these variations start at the mid-day and continue towards dusk and nighttime or sometimes seen only during the nighttime and can last throughout the night. One of these examples is given in Figure 3.10. Figure gives three days of VLF signal from top to bottom. These variations show periodic structures, especially seen in the middle panel of Figure 3.10. For this example, the periodicity is about one hour but they vary from 20 minutes to 1 hour. The magnitudes of the variations are also seen to be considerably high. We did not find any such variations in VLF signatures reported in the current literature and it is our next project to search on the cause of these variations seen in ITU SID VLF data.

Figure 3.11 gives a week continuous record of the same data in Figure 3.10 to emphasize these periodic variations do not occur all the time. Given weekly data in Figure 3.11, it is also seen that they are not related to the solar flare either. Above all, they occur during the night in this example.

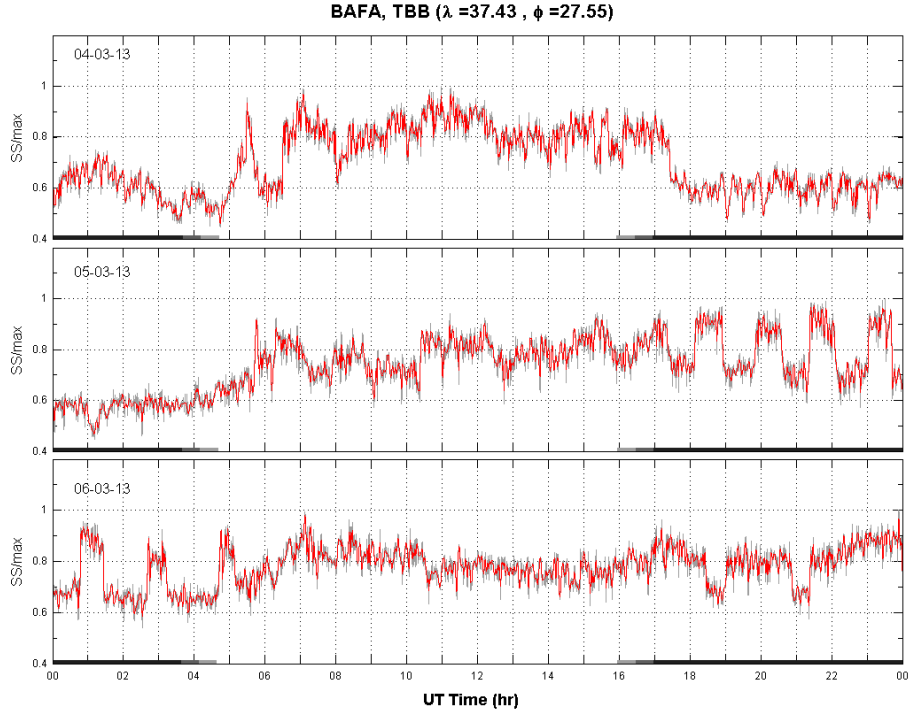


Figure 3.10: Example of wavy structures in ITU VLF data plotted in three successive days from March 4 to 6, 2013.

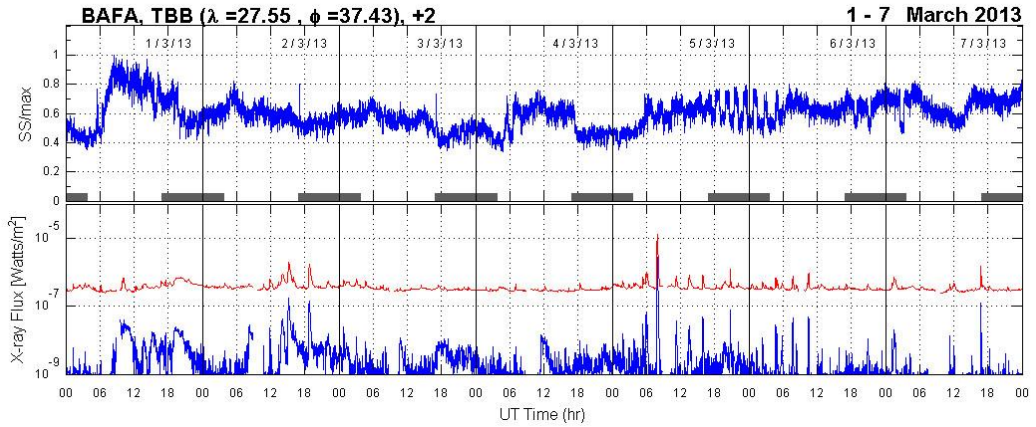


Figure 3.11: Example of wavy structures in VLF data plotted for a week (March, 1-7 2013).

Next chapter gives the summary and conclusions of SID-VLF observations measured by ITU-VLF antenna.

4. SUMMARY AND CONCLUSION FROM ITU SID-VLF OBSERVATIONS

In this part of our study, about two years of VLF data received at ITU using the SID monitor obtained from Stanford University. We record signals transmitted from 6 VLF transmitting sites over the world which one of them is BAFA at 26.7 kHz. Here we presented the variations in the VLF signal strength from BAFA station recorded for about 2 years. The main purpose of this part was to drive the general characteristics of the variations we have seen in VLF strength and look for the explanations behind these variations when possible. At first, we have looked at the solar flare association as the main cause of the VLF signal rate variations is the variations in the D region of the ionosphere caused mainly by solar flares. The effects can sometimes be resulted from the deviative structure of the D region and sometimes mirroring type structure of the D region, which are determined by the magnitude of the X- ray flux from the solar flares. We can summarize our findings in this part with brief discussions as follows:

1. Four general variations are observed in VLF signal rate received at ITU from BAFA transmitting at 26 kHz. These are daily variations tracking the solar radiation variations, which show a large drop during the midday and thus causing two broader shoulders around dawn and dusk, wavy periodic variations, which do not track solar radiation during daytime, wavy a periodic variations during throughout the day with two sharp rises at dawn and dusk.

These types of variations are very different than reported in the literature to this date. The VLF reflections during the day are expected to be from D layer. They are caused by the additional ionization in D layer as a result of the X rays flux in the lower atmosphere deposited from the solar flares. X rays can cause two types signatures in VLF waves. Sometimes decreases but sometimes increases in the signal rate corresponding to other solar flare, which occurs at the time either of the solar occurrence instantly or with some delay. We find several examples in our VLF data set that shows increased

level of VLF signal corresponding to solar flare but to our surprise these examples are not as many one would expect. Considering the theory and the available literature this is unexpected. Therefore, we plan to investigate this by comparing these results from BAFA with the VLF signals from other 5 stations we record at ITU. One thing, which is very clear, is that VLF signals received at ITU track the solar radiation during the day meaning high signal strength during the day and low at night following the increase and decrease in the ionization resulting from the solar radiation. This is a signature with no D layer effects and the signal is reflected from the higher layers of the ionosphere, like E, and F.

2. Another common variation seen in the VLF strength is the dawn and dusk enhancements with large drops during the mid-day. In other words, increases in signal rate around sunrise and sunset when the solar radiation just started to increase and start to decline. Decreases during the mid-day can be attributable to the local variations in electron concentrations resulting from ionospheric dynamics.

Wavy structures with periodic variations from 20 min to 1 hour are reported for the first time here and no corresponding in the available literature. Characteristics of these structures are: their periodicity varies from 20 min to 1 hour, the amplitudes are considerably high, and they occur dominantly at night and may last throughout the night. The detailed investigation of this property of VLF waves is deferred to our next study on the radio wave propagation.

5. ITU HF RADAR, IONOSONDE, AND IONOSONDE OBSERVATIONS

The ionosonde system in Istanbul (41.1N, 29E), called Dynasonde, is situated within the Ayazağa Campus of İstanbul Technical University. The system is operated by Upper Atmosphere and Space Weather Laboratory in Faculty of Aeronautics and Astronautics. It is set up in May 2012 and the continuous measurements started in October 2012. Any system, which transmits within the frequency band from 1-30 MHz, is also called as an HF-radar since these frequencies fall in the HF range of electromagnetic spectrum.

The basic concept related to the ionosonde is briefly explained in Chapter 1. A Dynasonde is a digital form of ionosonde. The difference between Dynasonde and Digisonde comes from the assumptions that they use to obtain the ionospheric parameters. A Dynasonde provides the hardware and software to obtain complete parameters that characterize the radio echoes returned from the ionosphere by sounding throughout the LF/MF/HF bands, 0.1-30 MHz. Following the transmission of the radio pulse, returned signals are digitized (12 bits) every 10 microseconds of "Time of Arrival", ToA, within a 467 - 5333 microsecond (70 - 800 km) listening window. Pulses are transmitted in groups of 4 or 8 designed patterns of receiving antenna selection and small (1 kHz) frequency offsets. Echoes are recognized in real time an algorithm which discards false echoes (noise from broadcast signals, rain or electrostatic noise, vehicle ignition etc.) and retains the ToA values corresponding to real echoes (corresponding to the amplitude of the complex part of the transmitted signals). It is the collection of these complex amplitudes and the independent variables of radio frequency, time, antenna location, and a few system parameters, which constitute a Dynasonde Echo. Following this, this information is transformed into physical quantities that define the echo parameters more explicitly and their estimation accuracies. The principal parameters are 'echolocations' (or the apparent direction-of-arrival, and the precise 'stationary-phase-group-range'), a line-of-sight Doppler estimate, one or more echo polarization parameters, an average phase value,

the echo peak amplitude, and (depending on the pulset design) several other echo characteristics. It is the collective assembly of these echoes with all of their physical attributes, which is considered to comprise the Dynasonde Digital Ionogram [7].

This is where the distinction between the dynasonde and other digital-ionosonde concepts holds. In Dynasonde case, these steps in data acquisition are made with minimal model assumptions and with no data pre-processing. An echo is an echo; it is not a selected Doppler peak following FFT processing and it is not even an amplitude peak. When amplitude is used to recognize echoes, it is the required ToA consistency among amplitude peaks within the pulset, which rejects false echoes and identifies true echoes [7].

The Dynasonde system at ITU was obtained from Scion Associates. It consists of two transmitting antennas with towers of 25 meters height, and 4 receivers with 5 meters. The ionograms are created using NeXtYZ software obtained from Colorado University. Software creates 79 ionospheric parameters relieved at ITU for each transmitted radio signal that vary from 1 to 20 MHz. The ionograms from the software are created at predefined intervals which chosen as every four minute. Figure 5.1 shows (a) a photo of the transmitters and the Dynasonde site at ITU Campus, (b) a photo of one of the receivers, and (c) rack that contains the Dynasonde software. The resulting parameters are presented at the web site <http://istanbul.ionosonde.net> with a special request for access.

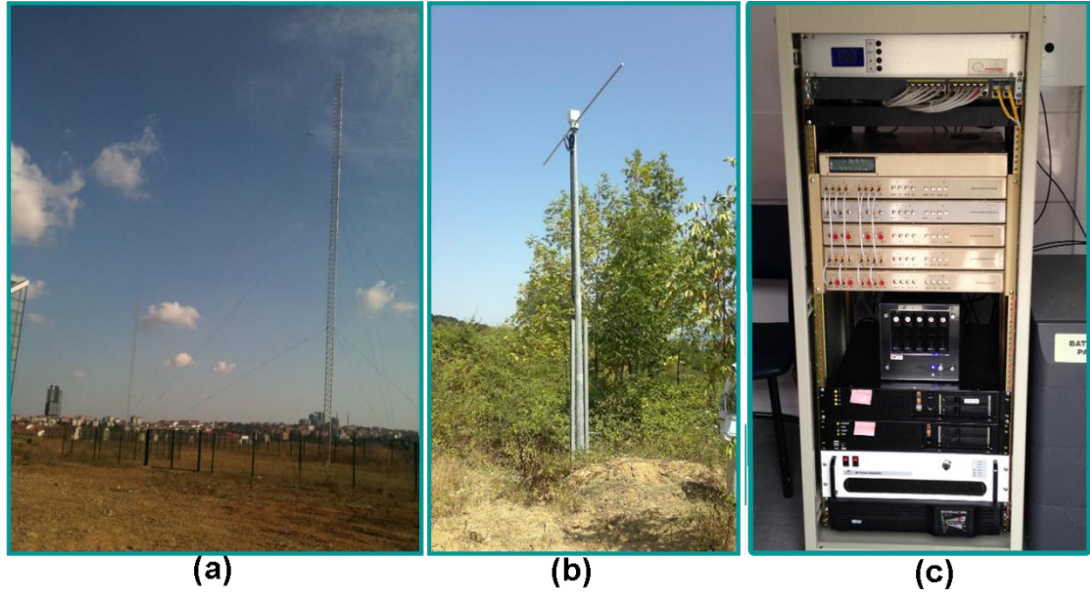


Figure 5.1: Photo of the ITU Dynssonde components: (a) transmitter site and transmitters, (b) one of the four receivers, (c) rack containing the Dynssonde software.

Figure 5.2 below gives an example of daytime ionogram produced by NeXtYZ on day Dec 15, 2013. In the figure, the left panel contains the frequency-height profile with echoes shown in color, selected echoes with numbers, and the software produced height profile with solid red line. The inset on the right gives the geometry that causes echoes in the north-south (N-S) and east-west (W-E). The inset just below the ionogram gives the signal levels in which the black is the background noise. We can see that the E and F layers on the ionogram. Two modes, ordinary and extraordinary modes of the radio signal are seen around 300 kms while E layer is seen to present as patches at about 120 kms. The signal hops, which are the reflection from the Earth's surface, are also seen in the ionogram above the associated ionospheric layer.

In the previous chapter, we made clear that the lowest part of the ionosphere (D layer-60-90 kms) is investigated by using low frequency radio signals, usually VLF. High frequency waves are used to study the ionosphere above D layer, i.e. above 90 kms up to 300-400 kms. Therefore, it is more suitable to study the E and F layers using HF signals as the critical frequencies of these layers determined by the electron concentration at these heights are within the frequency range of HF radio waves.

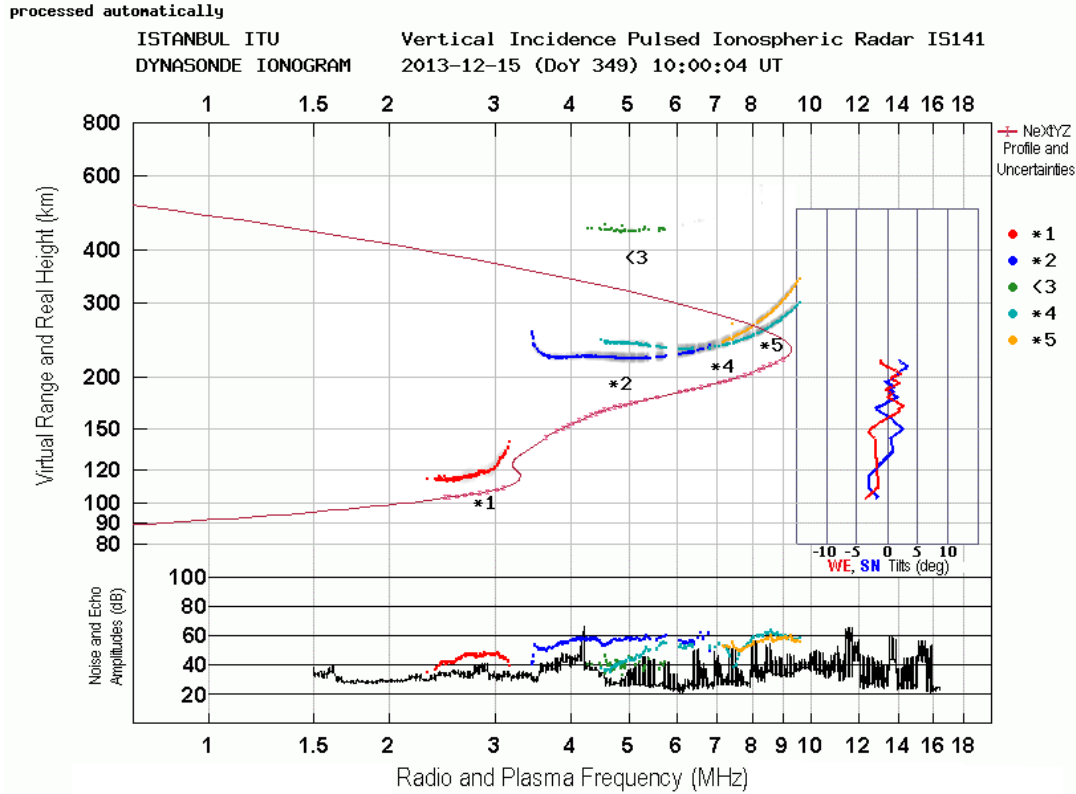


Figure 5.2: A daytime ionogram example produced by NeXtYZ at ITU on day Dec 15, 2013.

In this study, our main purpose is to determine the character of the ionosphere at Istanbul's location (41.1N, 29E) using the ionospheric parameters including critical frequency (thus maximum electron density) and critical height for each layer, Total Electron Content (TEC), and other 79 parameters produced by NeXtYZ from our Dynasonde. Especially, of interest are the E and F layer behavior and their response to magnetospheric activity. Once we determine the general structure of the ionosphere over Istanbul, we will compare our results with those from the current ionospheric models. Below, before we give our results, we present a brief literature survey on the ionosphere and on the mid latitude ionosphere. The subject is very broad and therefore we will restrict ourselves with a few very basic articles that serve toward our purposes.

5.1 Background Work On Ionosphere By HF Radars: E And F Layers

The ionosphere is subjected to both temporal, i.e. diurnal, seasonal, solar cycle, and spatial variations. In Chapter 1, we already reviewed some of this variability. It is well established that the formation of the ionosphere is primarily due to the

ionization of the upper atmosphere by solar X-ray and extreme ultraviolet (EUV) radiations, which vary according to the solar cycle. Observations indicate that parameters of the Earth's ionosphere, such as the critical frequency (f_oF_2), the peak electron density of the F region (NmF_2), and the total electron content (TEC), are strongly controlled by solar activity. We summarize the parameters that affect the ionospheric electron density as follows. These are the parameters that we also search dependence of the electron density at Istanbul.

1. Solar activity measured by the number of solar flares and the sunspots. During the solar flares, X-ray flux affects the ionization level by increasing the electron concentration, thus the ionization.
2. Magnetic storms and substorms: Energetic particles, mostly electrons, from the magnetosphere influence the electron density in the ionosphere. The polar ionosphere is affected by the auroral energetic particles coming from the magnetosphere, while equatorial ionosphere is affected by both the plasmaspheric particles and also substorms.
3. Gravity waves: Gravity waves are mainly driven from the tropospheric levels. These waves break in the ionospheric heights. From the troposphere, it is the acoustic gravity waves that affect the electron density distribution which result in what is called Travelling Ionospheric Disturbances.

Liu et al. studied the solar activity effects on the maximum electron density of F2 layer at 20 stations in the Asian-Australian sector using SEM/SOHO EUV data. They tried to quantify the solar activity dependence of NmF_2 in the east Asia/Australian sector and evaluate the dynamic effects and the atmospheric consequences of the solar activity effects of NmF_2 . They find that SEM/SOHO EUV observations show a nonlinear relationship between solar EUV and F107, and the solar activity factor $P = (F107 + F107A)/2$ better represent the intensities of SEM/SOHO EUV than F107 alone itself. At high values of the solar EUV flux, they observe saturation in NmF_2 . They further indicate that the saturation in NmF_2 cannot be explained only by the nonlinear representation of EUV by F107. The atmospheric consequences as well as the ionosphere itself via the dynamical effects contribute on the saturation process. Seasonal and latitudinal dependences are found in the solar activity variation of NmF_2 at these 20 ionosonde stations in the east Asia/Australian sector. They show

that besides solar EUV changes, the atmospheric consequences and the solar activity effects of hmF2, as well as the dynamical effects contribute to the solar activity changes in NmF2. They conclude that the extent of the contributions from dynamic effects (from neutral winds and electric fields) to the solar activity variations of NmF2 needs further investigation [26].

Yoon-Kyung Park investigated the F2-layer electron density variations in the middle latitudes depending on the solar activity using the foF2 observed by the ionosonde at Kokubunji in Tokyo, Japan, in the high solar activity interval (2000-2002) and the low solar activity interval (2006-2008). Their result showed that the semi-annual variation of the daily average foF2 is more distinctive in the high solar activity interval than in the low solar activity interval. The contribution of the geomagnetic activity to the F2-layer electron density variation in the middle latitudes was investigated by the time series analysis and periodogram analysis of foF2, the Ap index representing the geomagnetic activity in the middle latitudes, the IMF Bs (IMF $B_z < 0$) that can affect the geomagnetic activity, the speed, number density and dynamic pressure of the solar wind, depending on the solar activity. They found that the semi-annual variations of the daily average foF2, Ap index and IMF Bs are more distinctive in the high solar activity interval than in the low solar activity interval. This finding led them to conclude that the semi-annual variation of foF2 is more distinctive in the high solar activity interval than in the low solar activity interval as a result of R-M effect in Bs data. R-M effect causes a semi-annual variation in IMF Bs, which is observed distinctively in the variation of the geomagnetic activity during the high solar activity interval, and thus it greatly contributes in the variation of foF2. However, they show that the short-period variations related to the solar rotation, changes in the corona holes and the high-speed solar wind streams are reflected in the variations of the geomagnetic activity more distinctively in the low solar activity interval than in the high solar activity interval. This in turn resulted in their conclusion that the short period variations in foF2 may be resulted from the short-period variation of the geomagnetic activity. They indicated that the ionospheric changes depending on the geomagnetic activity are varied by not only the solar activity but also by the latitude. Therefore, the latitudinal dependence of foF2 should be looked at in order to extract the geomagnetic activity effects on F2 layer electron density [27].

Lanzerotti et al. examined the latitude dependence in total electron density (TEC) between Hamilton (39°N, 70°W) and Arecibo (18°N, 67°W) during 12 magnetic storms. A TEC increase at pre-local midnight is frequently observed in the low latitude station Arecibo but it is seldom observed in the higher-latitude Hamilton station. They attributed the pre-local midnight increases at Arecibo to the electrodynamical drift effects associated with westward electric fields. They show that the large TEC enhancements are associated with large positive geomagnetic bays at middle to high latitudes [28].

Figure 5.3 was taken from their paper and shows normalized median TEC to quiet day TEC in three days period. In the figure, in response to the geomagnetic storm at 18 EST shown with a small arrow, we see a sharp large drop in TEC at about 18 EST at dusk and just after a negative decrease is observed in TEC at Hamilton. This variation is called positive effect followed by a negative effect following the geomagnetic storm. If we compare this variation with TEC at Arecibo, we can see that the effect of the storm is not as clear and at the time of the storm there is not any sharp decrease. The authors attributed these variations between two different cities to the effect of latitude.

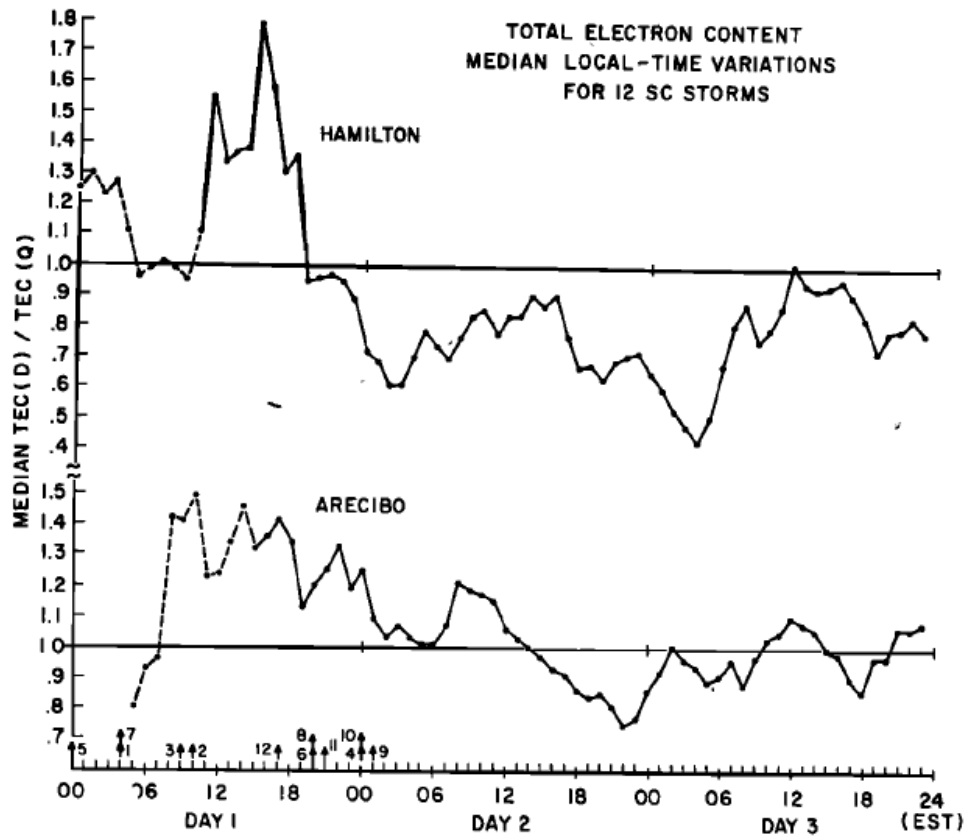


Figure 5.3: Normalized median TEC during geomagnetic storm at Hamilton (top) and Aerocibo (bottom) [28].

Klobuchar et al. studied the variations in the electron content in 10 stations in USA during ionospheric storm of March 8, 1970. The stations are distributed at about 45° latitude but separated in longitude. Thus their results represent the longitudinal variations of electron density during magnetically disturbed times. These stations are Hawaii, Stanford, Ft. Collins, Boulder, Urbana, Turkey Pt., Rosman, Norfolk, Hamilton and Arecibo. Aerocibo is located in US but included for comparison. The column density and average values (dashed) of electron content March 1 through 11, 190 covering the storm period have been shown in Figure 5.4 below. Arrow in the panels on the horizontal axis marks the beginning of the storm time. One can clearly see that the electron density at the stations in the west of Boulder (Hawaii, Stanford, Ft. Collins and Boulder) is seen to be depressed from their average values during the storm while the east of Boulder (Hawaii, Stanford, Ft. Collins, Boulder, Urbana, Turkey Pt., Rosman, Norfolk, Hamilton) shows an increase over average electron density [29].

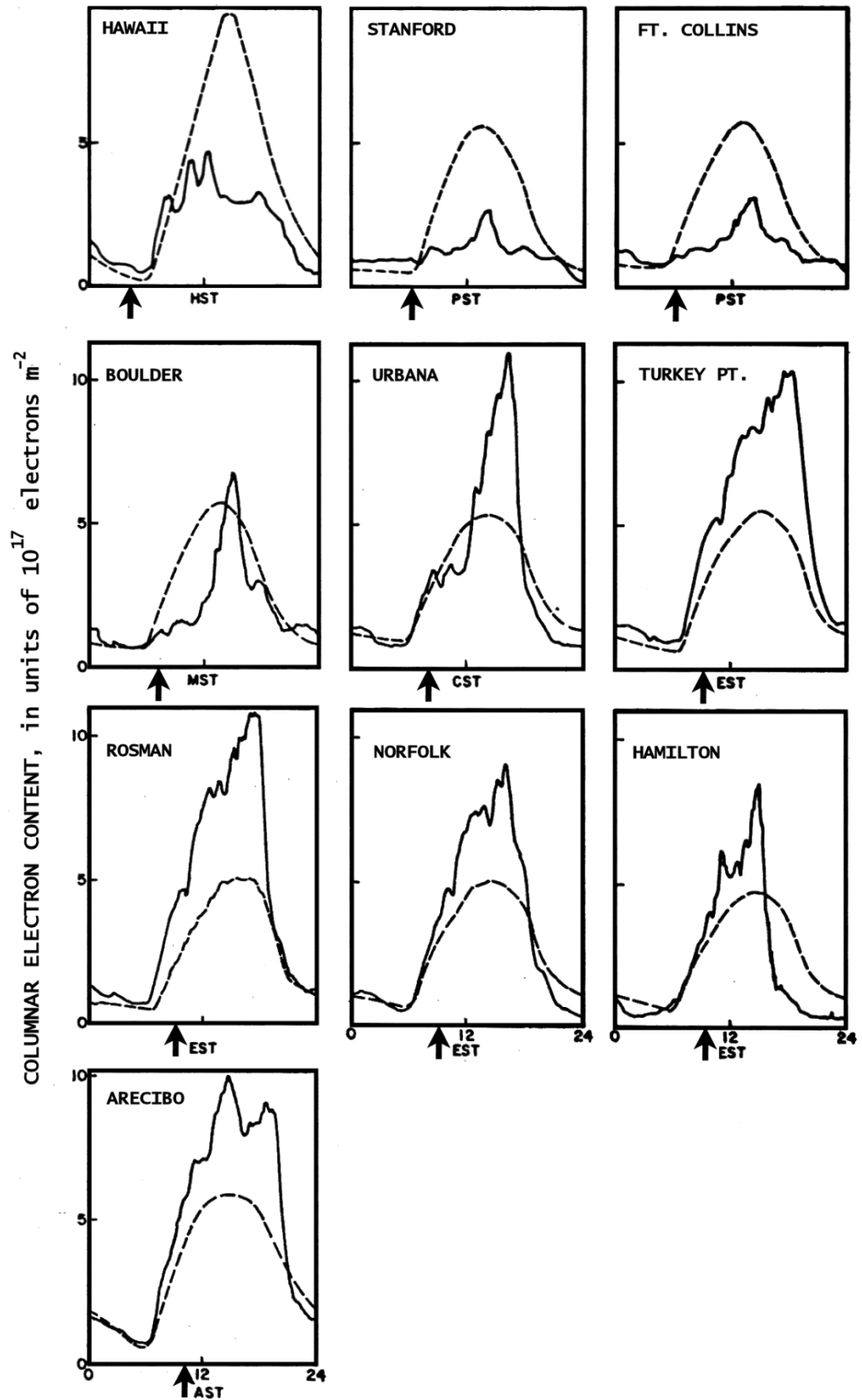


Figure 5.4:TEC variations at 7 stations in North US during March 8, 1990 ionospheric storm [29].

TEC patterns during magnetically disturbed times are found to show three main categories [14]. These phases are Regular Positive Phase (RPP), a Delayed Positive Phase (DPP) and No Positive Phase (NPP). RPP occurs when geomagnetic storm develops in daytime hours, between sunrise and midafternoon. If storms sudden commencement or main phase onset does not developed in daytime hours either a DPP is observed after dusk or NPP can occur.

To understand the nature of storm time TEC variations, Hibberd and Ross indicated that in the first 24 hours after storm, TEC values show a positive response, which can be twice as large as the quiet time values, and in the second day following the storm, TEC values start to decrease, even below to the quiet day background values [30].

TEC is the summation of electron density with height. F2 layer is the main contributor in TEC value; approximately 60% of TEC is coming from above of F2 layer density peak [14].

Many studies [31-32], examined the state of ionosphere during geomagnetically quiet and disturbed periods using long-term ionosonde data. These studies described the variations in the maximum electron density of the F2 layer. These studies showed that the principal sources of the variation of peak electron density are photo-ionization of neutral atmosphere by solar extreme ultra-violet (EUV) radiation and neutral composition of the atmosphere. Additionally, secondary sources are identified as neutral winds propagating from below, thermospheric winds, and ExB drift in the ionosphere.

Responses of TEC to geomagnetic storms are also studied by Bergeot et al. They concluded that there is a reduction in TEC values (with a 20% average) after geomagnetic storm time onset. This reduction is especially observed in higher latitudes, globally. At low latitudes a positive storm effect, increase in TEC values, and is observed. This is explained by the effects of the neutral wind activity in ionospheric heights. These variations in TEC values at geomagnetic storm time recover to pre-storm values within a 3-4 days period after storm onset [33].

Mendillo and Klobuchar showed that, for all seasons, there is a clear characteristic signature of TEC storm effect. This is seen in Figure 5.5. In all seasons including the winter, an increase in TEC during the storm time is obvious in Figure 5.5. The higher electron density observed in winter is attributed to the seasonal anomaly. In

their paper, they indicate that the positive phase of storm takes much longer time in winter months than summer. In the summer months, negative phase of the storm is more dominant. In their paper, they also showed that, it is more likely to observe “dusk effect” in winter months, resulting from the vertical motions, which are much larger in winter months than summer time [34].

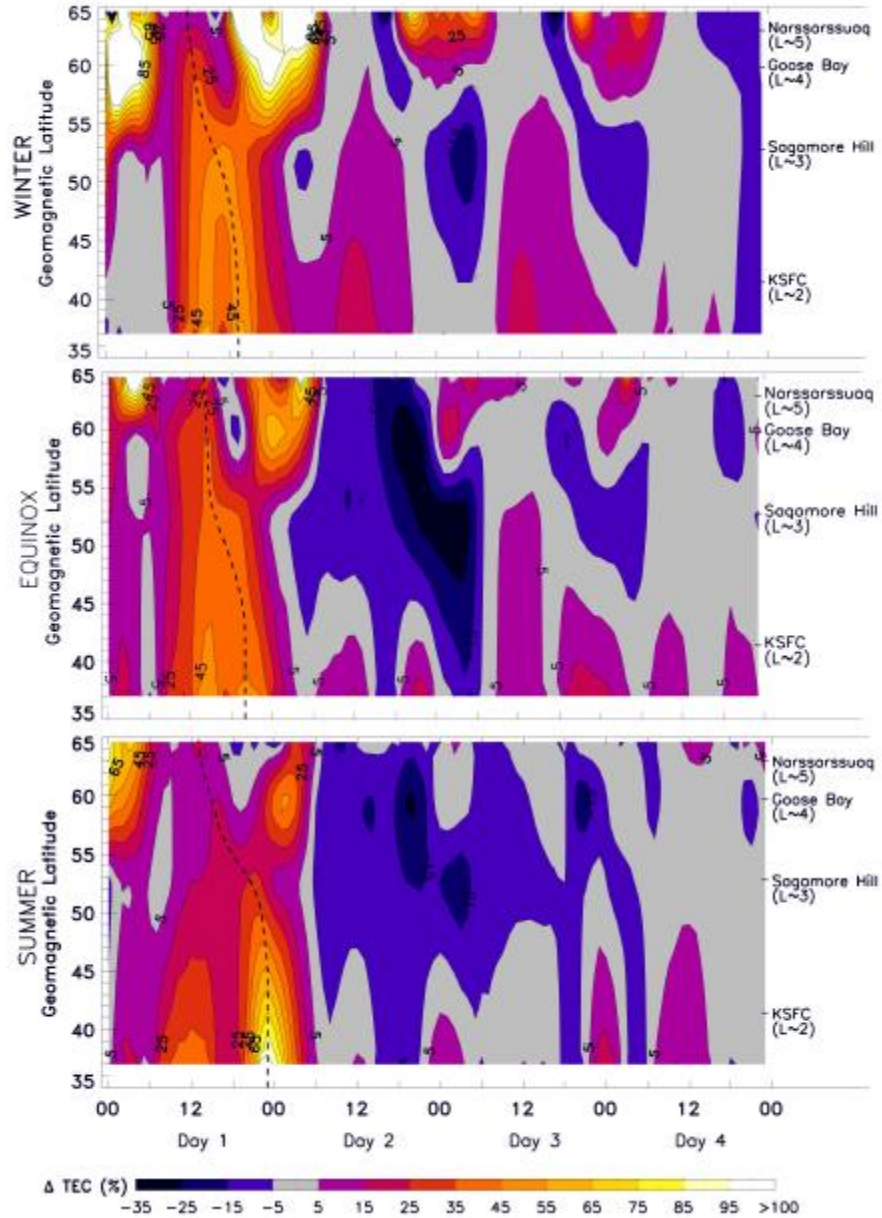


Figure 5.5: TEC variation at different seasons during the four days following the storm [34].

In the review by Mendillo [14], he compared the results from three studies by Mendillo [35], Hargreaves and Bagenal, [36], and Mendillo and Klobuchar [34] to

drive the TEC variation under different solar activity levels. The first panel of Figure 5.6 shows the results of [35]. He studied 28 storms when solar activity was high, $\langle F_{10.7} \rangle = 151$. Middle panel of Figure 5.6, examined 75 storm events with medium solar activity, $\langle F_{10.7} \rangle = 139$ [36]. The last panel at bottom of Figure 5.6 gives the work in [34], which they used 109 storms during low solar activity, $\langle F_{10.7} \rangle = 99$. Duration of the negative phase during disturbed times is different for all three solar activity levels. At solar maximum conditions, negative phase persists more than 4 days, and it lasts about or up to 4 days under solar moderate conditions, while it ends within 2 days under the solar minimum conditions.

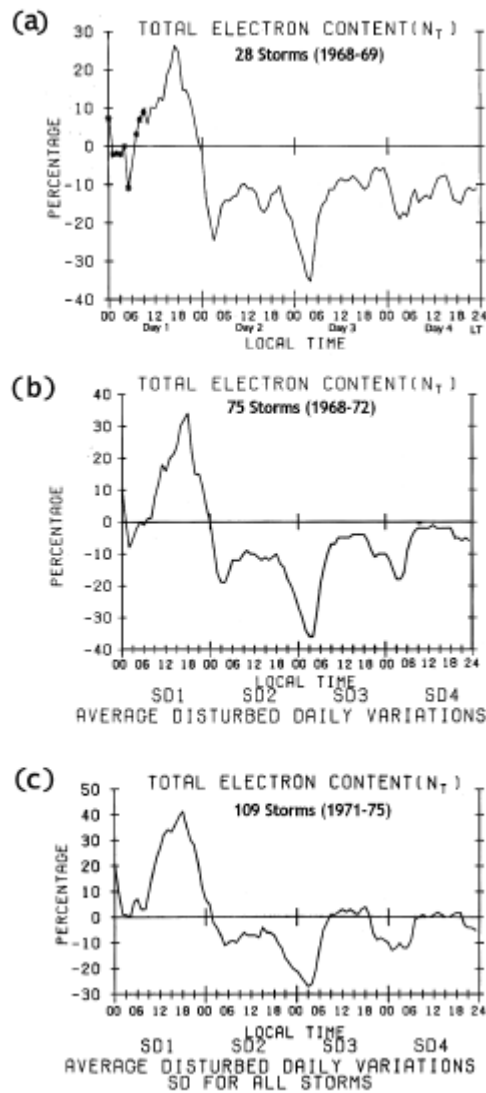


Figure 5.6: Averaged daily TEC variations under different solar activity periods [14].

Longitude effects of TEC under magnetic storms were also examined in Mendillo's review [14]. He compared three different low latitude stations with similar magnetic

In Figure 5.8, monthly variations of TEC data during the year 1971 at Sagamore Hills, Massachusetts, USA are presented [14]. Generally, highest curves in the plot are associated with positive phase of the storms while lowest curves are a result of the negative phase (a day after the storm). Even if these storm-days are removed from the data, there is still 15-20% of variability [14]. The reason for this variability is the coupling from below [37] and daily changes in solar irradiance [32].

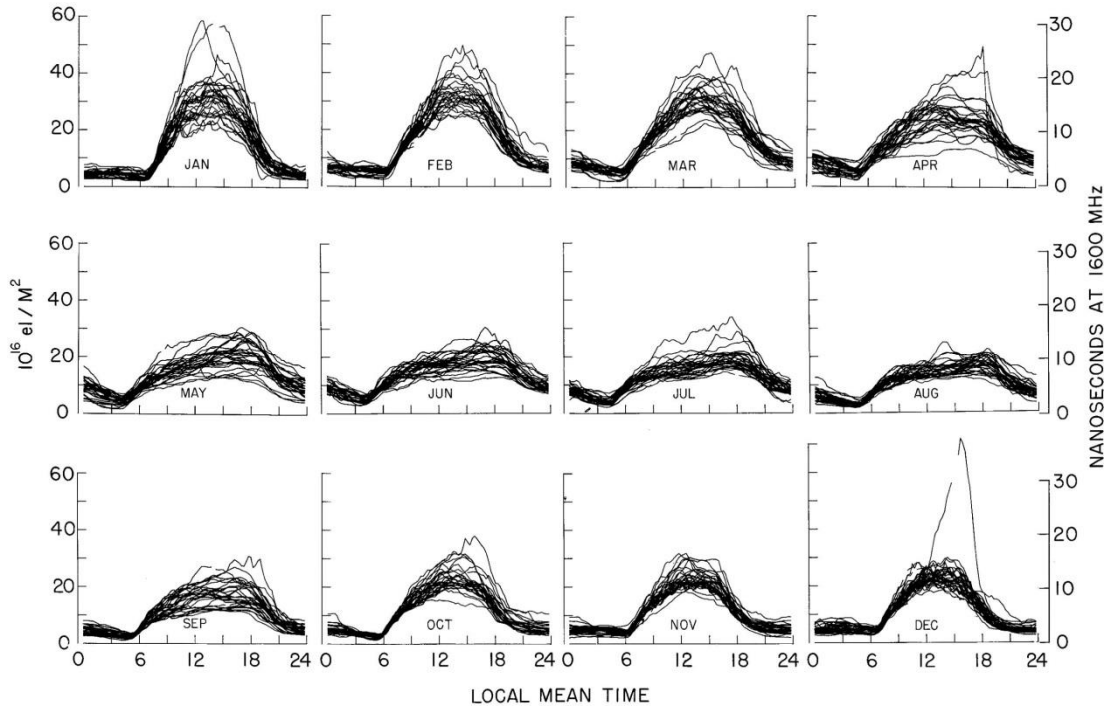


Figure 5.8: Monthly variations of TEC in 1971 at Sagamore Hills, MA, USA [14].

Nighttime variability of TEC at midlatitudes is examined in Klobuchar et al.'s study [38]. TEC observations are taken from two geostationary satellites, Canary Bird and ATS-3. In the Figure 5.9, left panels give the TEC variation and right panels show N_{max} . Magnetospheric activity index, K index, for the nighttime are indicated in every panel separately. In Figure 5.9, the plot in the middle of right panel is an example of quiet time conditions with a smallest K index. It is clear that all other panels show an increased TEC and N_{max} as response to the higher K during the course of the storm.

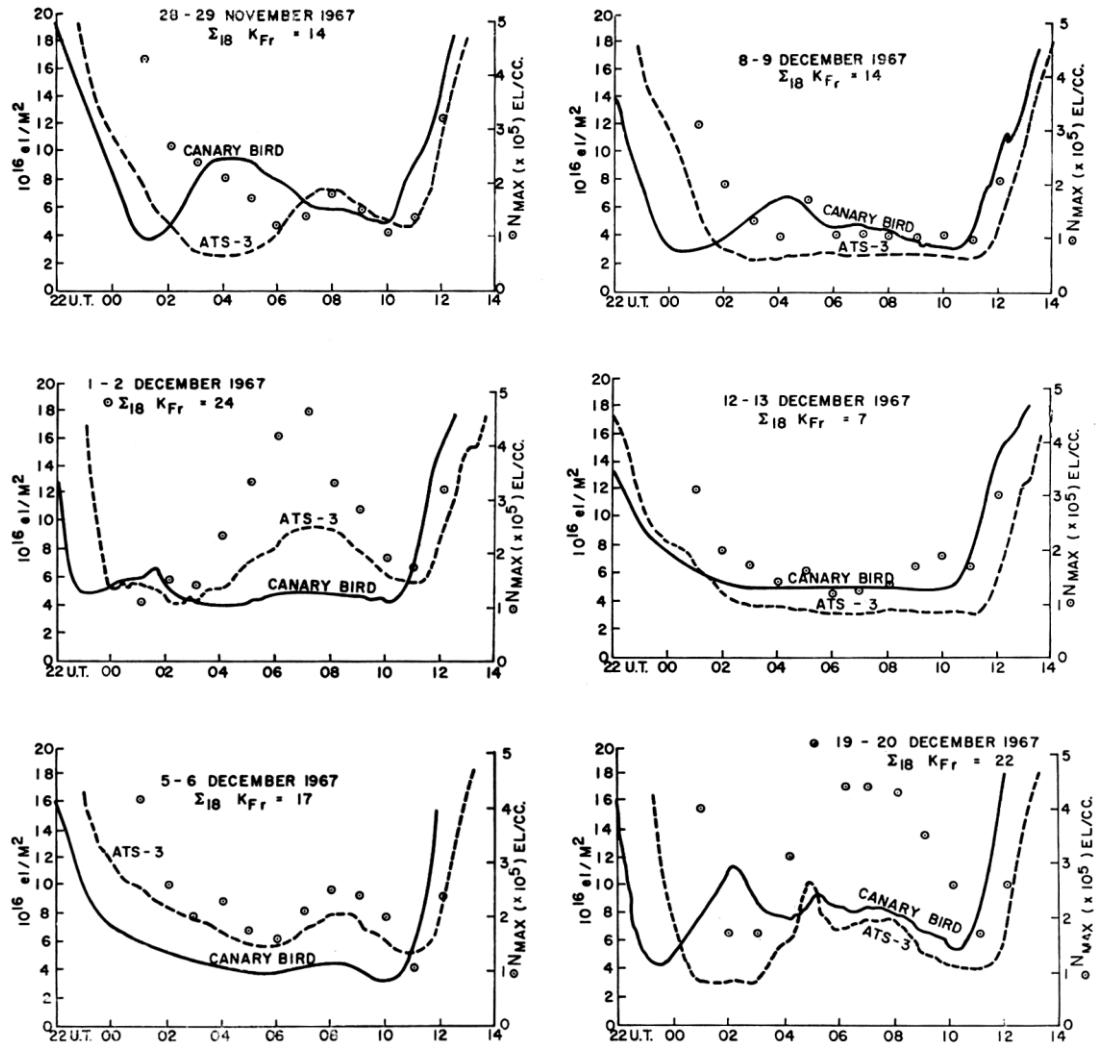


Figure 5.9: Nighttime variations of TEC for six different events. Quiet time conditions at middle right panel.

5.2 Ionospheric Models

5.2.1 International reference ionosphere (IRI)

The International Reference Ionosphere (IRI) is an international project that is used to produce an empirical standard model of the ionosphere, based on all available data sources. COSPAR and URSI are the supporting agencies for IRI as COSPAR needs such a specification for the evaluation of environmental effects on spacecraft and experiments in space, and URSI for radiowave propagation studies and applications. At the request of COSPAR and URSI, IRI was developed as a databased model to avoid the uncertainty of theory-based models, which are only as good as the evolving theoretical understanding. Being based on most of the available and reliable observations of the ionospheric plasma from the ground and from space, IRI provides

monthly averages of electron density, electron temperature, ion temperature, ion composition, and several additional parameters in the altitude range from 60 km to 2000 km. Additional parameters given by IRI include the Total Electron Content (TEC), the occurrence probability for Spread-F and also the F1-region, and the equatorial vertical ion drift. A working group of about 50 international ionospheric experts is in charge of developing and improving the IRI model. Over time as new data became available and new modeling techniques emerged, steadily improved editions of the IRI model have been published [39].

The major data sources are the worldwide network of ionosondes, the powerful incoherent scatter radars (Jicamarca, Arecibo, Millstone Hill, Malvern, St. Santin), the ISIS and Alouette topside sounders, and in situ instruments on several satellites and rockets. IRI is updated yearly during special IRI Workshops (e.g., during COSPAR general assembly) [40].

The parameters, input and height range of IRI are given below:

IRI Parameters: Electron density, electron temperature, ion temperature, ion composition (O^+ , H^+ , He^+ , N^+ , NO^+ , O^+_{2} , Cluster ions), equatorial vertical ion drift, vertical ionospheric electron content (vTEC; a user can select the ending height for the integration along the electron density profile), F1 probability, spread-F probability, auroral boundaries, effects of ionospheric storms on F and E peak densities.

IRI Inputs:

Required: solar indices (F10.7 daily, 81-day, and 12-month running mean; sunspot number 12-month running mean), ionospheric index (ionosonde-based IG index 12-month running mean), magnetic index (3-h ap, daily ap). The indices are found internally by IRI for the user-specified date and time. In the case of F10.7D, F10.7_81, F10.7_12, R_12, and IG_12 a user can input his/her own values.

Optional: The user can provide a number of input parameters and the IRI profiles will then be adjusted to these input parameters:

1. F2-peak height (hmF2) or propagation factor M3000F2,
2. F2-peak plasma frequency (foF2) or electron density (NmF2),

3. F1-ledge height (hmF1), plasma frequency (foF1) or electron density (NmF1)
-peak height (hmE), plasma frequency (foE) or electron density (NmE)
4. D-ledge height (hmD), plasma frequency (foD) or electron density (NmD)

IRI Height Range:

Electron density: daytime: 65-2000km, nighttime: 80-2000km

Electron and ion temperature: 60-2500km (IRI-95 option: 60-3000km)

Ion composition: 75-2000km (DS95/DY85 option: 80-2000km)

Disadvantages of IRI:

As IRI represents the monthly average behavior of the ionosphere at a given place and time, for a given level of solar activity, it can predict the changes from one month to the next but not from day to day. More and more applications, however, require a description of the day-to-day variations. There is an IRI effort underway to include a quantitative description of ionospheric variability in IRI in the form of the monthly standard deviation [41,42,39]. A more accurate description of the changes from day to day requires the use of real-time data and of updating or assimilation techniques to combine IRI with these data and in the process produce the Real-Time IRI (IRI-RT). There is also the need for real-time ionospheric specification and forecast for space weather applications [39].

Therefore, in IRI model, the magnetic storm or the substorm effects cannot be expected to be seen. However, the model results help us to drive the deviations from an average variation and thus quantify the difference caused by the storms/substorms. There is also an ongoing effort in IRI community to include the storm/substorm effects in terms of integrating AE auroral index into the model, which in turn may provide more realistic comparisons between the data and the model during magnetically disturbed times.

5.2.2 TIE-GCM

The NCAR Thermosphere-Ionosphere- Electrodynamics General Circulation Model (TIE-GCM) is a comprehensive, three-dimensional, non-linear representation of the coupled thermosphere and ionosphere system that includes a self-consistent solution of the low-latitude electric field. The model solves the three-dimensional momentum, energy and continuity equations for neutral and ion species at each time step, using a

semi-implicit, fourth-order, centered finite difference scheme, on each pressure surface in a staggered vertical grid. It has 29 constant-pressure levels in the vertical, extending from approximately 97 km to 500 km in intervals of one-half scale height, and a $5^\circ \times 5^\circ$ latitude-longitude grid, in its base configuration. The time step is 120 s.

Hydrostatic equilibrium, constant gravity, steady-state ion and electron energy equations, and incompressibility on a constant pressure surface, are assumed. Ion velocities are derived from the potential field created by combining the imposed magnetospheric potential with the low-latitude dynamo potential, and then calculating ion velocities from ExB drifts, rather than solving the ion momentum equations explicitly. Some minor species are not currently included in the model, including hydrogen and helium and their ions, and argon. Several parameterizations are used in the TIE-GCM: an empirical model is used to specify photoelectron heating; the production of secondary electrons is included using an empirical model derived from two-stream calculations, the effects of mixing by gravity waves are included using an eddy diffusion formulation; CO₂ is included by specifying a lower boundary condition and assuming that it is in diffusive equilibrium. The upper boundary conditions for electron heat transfer and electron number flux are empirical formulations. At the lower boundary, atmospheric tides are specified using the Global Scale Wave Model (GSWM) [43].

The model inputs are given below:

- **Solar EUV inputs:** F107 (current daily F10.7 solar index) and F107A (81-day center-averaged F10.7 solar index)
- **Particle precipitation:** Hemispheric Power in GW, obtained from 3-hour Kp index
- **Ionospheric electric fields at high latitudes:** Provided by Heelis model and Weimer model.
- **Inputs for Heelis model:** Cross polar cap potential in kV, obtained from 3-hour Kp index Hemispheric Power in GW, obtained from 3-hour Kp index Optional (not implemented): y-component of the interplanetary magnetic field (B_y) in nT
- **Inputs for Weimer model:** Interplanetary magnetic field, B_y and B_z , in nT Solar wind density and speed, ρ and v , in cm^{-3} and km s^{-1}

- **Inputs for lower boundary:** Diurnal and semi-diurnal migrating tides, specified by the GSWM

The model outputs are:

- Primary timed-dependent output fields, specified in latitude, longitude, and pressure level:
 - Geopotential height: Height of pressure surfaces (cm)
 - Temperatures: Neutral, ion, electron (K)
 - Neutral winds: zonal, meridional, (cm s^{-1}), vertical (s^{-1})
 - Composition: O, O₂, NO, N(⁴S), N(²D) (mass mixing ratios - dimensionless)
 - Ion and electron densities: O⁺, O₂⁺, Ne (cm^{-3}), (NO⁺ is calculated from Ne - (O⁺ + O₂⁺))
 - Electric potential: (V)
- Other fields are available as secondary histories, which can be set as needed [43].

6. RESULTS OF HF RADAR

In this section, we will present the general structure of ionosphere at Istanbul obtained from ITU Dynasonde measurements described in previous section. Although we obtain 79 ionospheric parameters, in this study we only use foF2, NmaxF2, hmF2, and TEC. We calculate NmaxF2 from foF2. Although we also have E region electron densities, in this study, we mainly concentrate on describing features we observe in the F2 region electron density. Thus, the main focus will be to derive the height and temporal variability of the F2 layer at Istanbul, a midlatitude ionosonde station. We study the variability in terms of the solar radiation, substorm dependence, and the gravity wave effects. We have about 1 year of data from extending from October 2012 to October 2013. The resolution of ionograms created are 4 min though higher resolution of data can be obtained for special cases/requests when needed. Both the statistical and case studies are carried out by scanning through one year of 4 min data to select the cases. Statistical results based on 1 year of data that reveal the general character of F2 layer will be presented. This will be followed by the selected cases to study the substorm effects. We will also compare our results from those obtained using IRI and TIEGCM models.

6.1 General Character of F2 layer at Istanbul

Figure 6.1 gives an example of two ionograms to illustrate the day-night differences in F2 layer electron density. In the figure, while the left panels give the ionograms for the day April 21, 2013 at 09:00 UT representing the day (top) and 21:00 UT representing the night. 09:00 UT corresponds to 12 LT and 21:00 corresponds to 24 LT. The horizontal axis in the ionograms is the transmitting frequency ranging from 1 to 20 MHz. The returned signals (echoes) at different frequencies are converted to density as described in Chapter 1. The solid red line in the ionograms gives the density profile derived by NeXtYZ software. Two traces at F layer heights are seen. One of them (gray) corresponds to the ordinary mode of the wave and the other is the

extraordinary mode (green). The selected echoes by NeXtYZ is shown in stars on the right of the ionogram while the “<” indicates the rejected echoes. The time series plots on the right gives the daily variations of E and F2 layer parameters in the order from the top to bottom as foF2, hmF2, foE, hmE and TEC including both E and F layer electron densities. Time axis is given in UT and the Local noon (green) and local evening (pink) is marked by vertical lines.

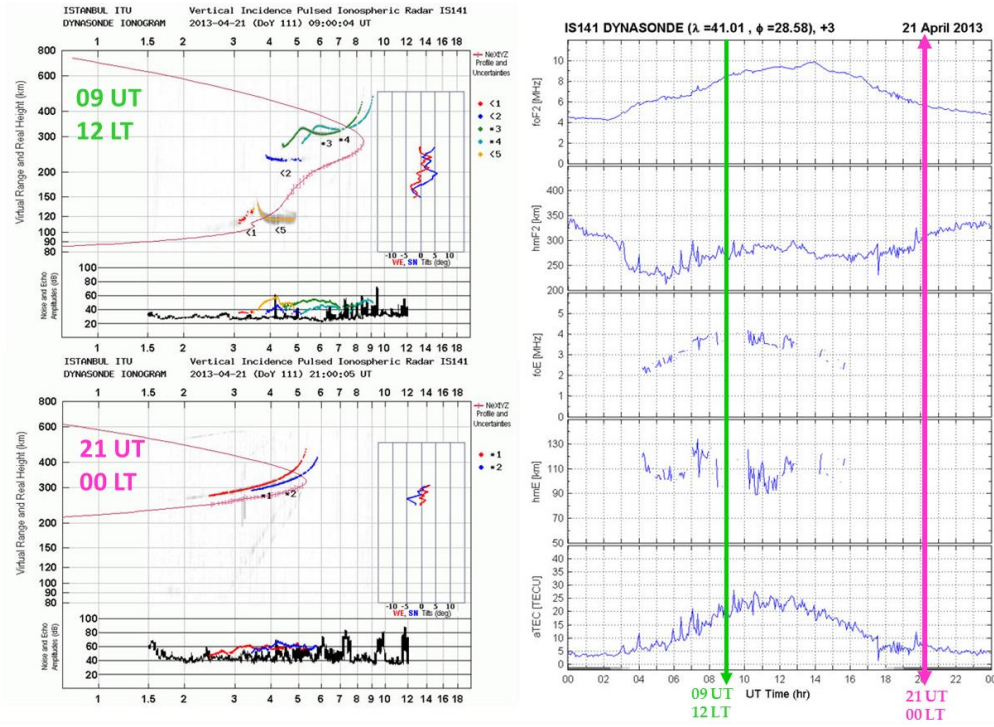


Figure 6.1: On the left is an example of two ionograms to illustrate the day and night differences at ITU station for the day April 21, 2013 at 12 LT and 00 LT times. On the right, daily variation is presented for the ionospheric parameters of F2, hmF2, foE, hmE and TEC on the same day.

In Figure 6.1, we can see that the daytime critical frequency for F2 layer, foF2, occurs at about 8.5 MHz for ordinary mode and 9 MHz for extra ordinary mode. These frequencies decreased to 5.7 MHz and 5.9 MHz during nighttime for ordinary and extraordinary modes respectively. In our analysis, we use ordinary mode. We can also clearly see that the E layer disappears at night and the height of the critical frequency rises from 200 km during day to about 350 km at night. The daily variation given on the right panel of Figure 6.1, we can see that the electron density is higher during the day reaching a peak at about 14:00 UT while the height of the maximum electron density is lower from 03:00 UT to 07:00 UT and from 14:00 UT

to 18:00 UT. Height of the peak electron density is higher from 05:00 UT 14:00 UT and from 18:00 UT to 05:00 UT. It reaches its maximum at 00:00 UT at about 340 km, and it is lowest around 05:30 UT at about 220 km. The midday peak occurs around 13:00 UT. The gray highlight at the bottom of the horizontal axis indicates the course of the Sun's height in the sky. We can see that the sunrise and sunset times are the times when minima in peak height occurs. These daily variations are a consequence of the variations in the solar radiation during the day.

In Figure 6.1 we also see the traces from the E layer during the day from 04:00 UT to 16:00 UT in the third and fourth panels of the time series plot given on the right. Though patches, the traces indicate that the E layer electron density shows a maximum around 10:00 UT with a maximum of 4 MHz. The E layer's peak critical frequency varies from 2 MHz to 4 MHz. The maximum height of the E layer, on the other hand, varies from 90 km to 130 km. It is the highest at 04:00 UT while it is the lowest at 10:00 UT. The E layer height does not show a great variability and its average is about 100 km.

Figures 6.2, 6.3 and 6.4 below give the monthly variations of the critical frequency of foF2, maximum height where the peak critical frequency (hmF2) occurs and TEC throughout the year. Figure 6.2 illustrates the seasonal variation of these parameters at the same time for the year of 2013. The columns from left to right in the figure represent autumn, winter, spring and summer seasons respectively. We can see that the maximum daytime electron density occurs in October with peak reaching to 10 MHz while the minimum daytime electron density is seen in September at about 6 MHz. The maximum nighttime electron density is found in May with 5.5. MHz around 03:00 UT while minimum nighttime electron density is seen in December at 1 MHz, which is the default minimum frequency. During the spring months from March to May, in general but especially at the night, highest electron densities were recorded at ITU station. We can see that the electron density shows more variability during the day around noon times than during the night at all months and all seasons. The variability in electron density starts to increase from May to July. The variability starts about 05:00 UT and continues throughout the day and extends into the night till midnight at 00:00 UT. Starting from April through August, and small but visible in September and even in October, a second peak in electron density appears around sunset at about 18:00 UT and is called as the dusk phenomena in the

literature. The high variability reflects highly dynamic ionosphere recorded in Istanbul, a midlatitude station. The distribution of foF2 broadens starting from March to August and a flatting during the daytime is especially in August, obvious. The difference between night and daytime foF2 decreases in spring and summer months while it is greater in autumn and winter. The midnight and midday difference is rather sharply seen in October through April. The peak distribution occurs around 09:00 UT in September but it shifts toward noon to 12:00 UT by the month of May. The distribution is thus seen slightly left shifted around the peak in autumn and winter months. Statistical properties of Figure 6.2 are given in Table 6.1.

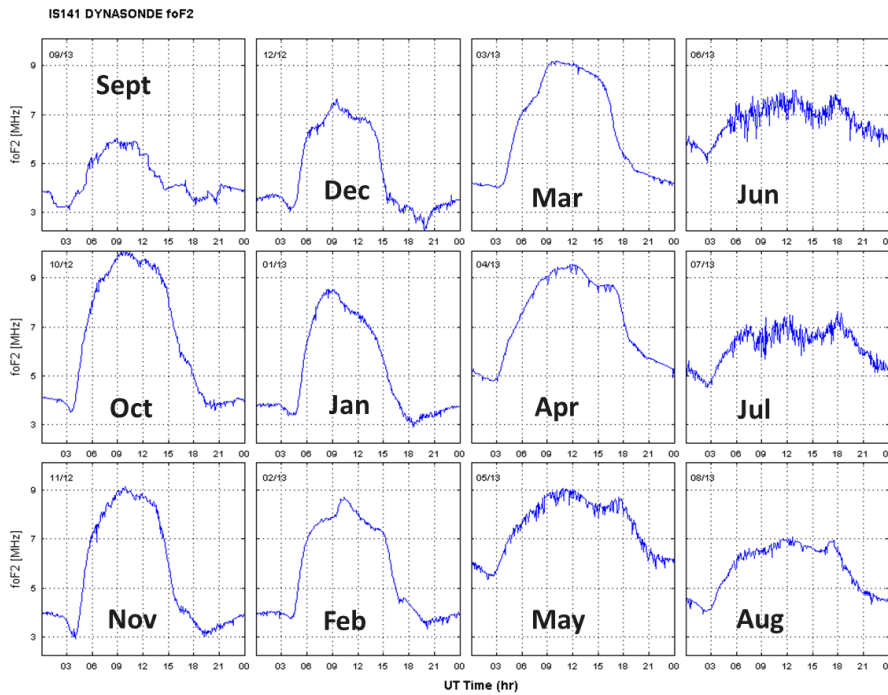


Figure 6.2: Monthly variations of foF2, the critical frequency of F2 layer.

Table 6.1: Statistical properties for the data given in Figure 6.2.

		Mean	Median	Max	Min	Skewnes
Fall	September	6,49	5,70	10,00	3,69	0,23
	October	5,57	4,10	8,96	3,19	0,45
	November	4,66	3,67	7,39	2,65	0,47
Winter	December	5,19	3,93	8,42	3,12	0,54
	January	5,64	4,70	8,57	3,62	0,29
	February	6,42	6,19	9,13	4,08	0,14
Spring	March	7,30	7,58	9,45	4,82	-0,16
	April	7,48	7,93	8,89	5,56	-0,41
	May	6,73	6,90	7,55	5,39	-0,57
Summer	June	6,21	6,53	7,03	4,70	-0,76
	July	5,76	6,17	6,89	4,09	-0,43
	August	4,37	4,05	5,89	3,23	0,63

Figure 6.3 is the plot of hmF2 according to months and the each column corresponds to the seasons. In general, we see that throughout all months, F2 layer occurs at higher altitudes during the daytime and lowers during the day. The highest altitude that the F2 peak occurs in April and May around 360 km at midnight, 00:00 UT. The lowest nighttime altitude is seen in August at 300 km at 00 UT. The F2 peak occurs at the lowest at dusk (15:00-16:00 UT) when the Sun sets in September at about 120 km. The variability in hmF2 increases during the summer months and during nighttime in general when compared to the daytime. During the midday, hmF2 rises again but never reaches the maximum height seen at midnight. It rises up to 290 km during midday in April when the highest was recorded in this year. In August, hmF2 stays stable at about 240 km during the day. Especially May, June and July are the months when hmF2 greatly fluctuates throughout the day and night while the lowest

variations are recorded in April. Day and night differences are the highest in September while the difference between day and night closes up in Spring and Summer months. Statistical properties of Figure 6.3 are given in Table 6.2.

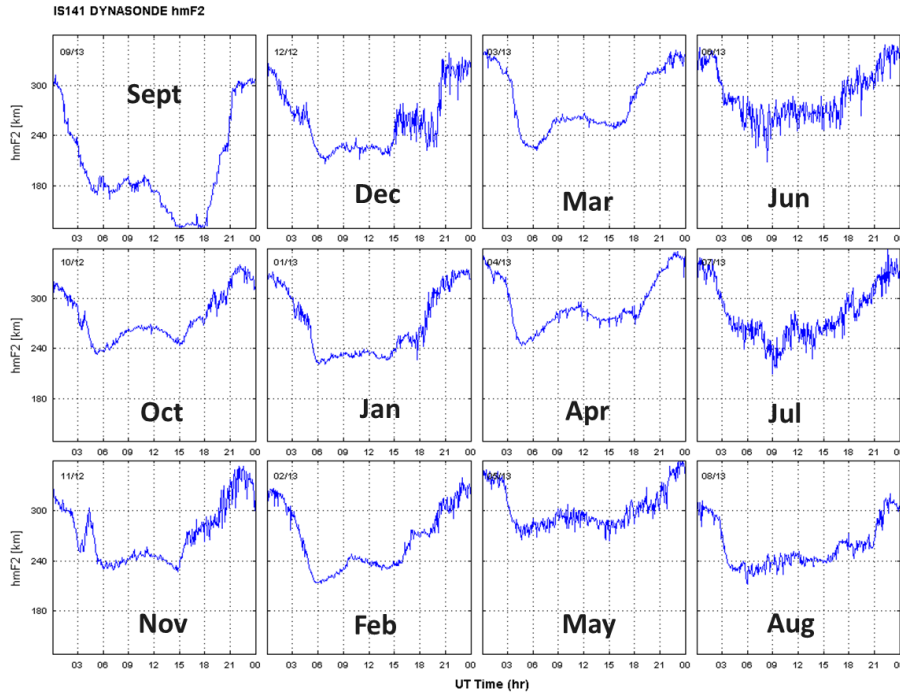


Figure 6.3: Monthly variation of hmF2, height corresponding to maximum electron density in F2 layer.

Table 6.2: Statistical properties for the data given in Figure 6.3.

		Mean	Median	Max	Min	Skewnes
Fall	September	277,24	267,66	331,94	236,11	0,55
	October	272,43	264,76	342,14	231,99	0,61
	November	257,10	251,68	321,61	214,08	0,65
Winter	December	268,10	252,15	329,17	224,18	0,44
	January	264,65	253,57	324,94	215,90	0,38
	February	279,70	260,97	335,57	227,23	0,30
Spring	March	293,40	283,01	349,71	248,42	0,56
	April	302,13	292,21	352,12	277,88	0,98
	May	287,72	276,04	339,61	250,06	0,59
Summer	June	282,13	269,22	338,07	230,31	0,45
	July	257,01	245,74	308,17	227,62	0,92
	August	199,37	181,38	305,40	132,06	0,79

Similar variations can also be detected in Figure 6.4 below, which shows the monthly variations in total electron density (TEC). TEC is calculated by taking the integral from the base of the E layer till the maximum peak of F2 layer. Therefore, variations in TEC also contain the variations in E layer as well. It is undoubtedly clear that the total electron content at İstanbul increases in spring months but it is as much higher in the month of October as well. The variability in TEC is also seen to be the highest during the summer months, especially in June and July. The dusk phenomena appear in months of May, June and July but also visible in Mar, April and August. The lowest daytime TEC is recorded in months of December and September while the highest daytime TEC is found in October, April, May and March. The lowest nighttime TEC is seen December at dusk at 18:00 UT while the highest nighttime TEC is found in June at noontime 12:00 UT. Peak TEC during the daytime is

observed at 10:00 UT in Autumn, and Winter while it is shifted to 12:00 UT in Spring and Summer. Statistical properties of Figure 6.4 are given in Table 6.3.

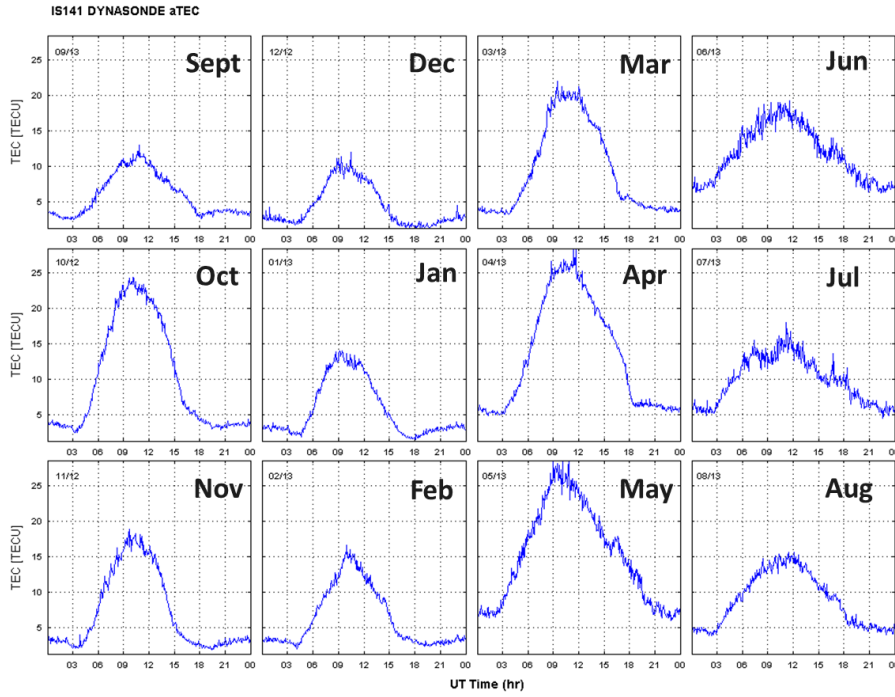


Figure 6.4: Monthly variations of TEC, Total Electron Content of 1-year data.

Table 6.3: Statistical properties for the data given in Figure 6.4.

		Mean	Median	Max	Min	Skewnes
Fall	September	10,17	5,54	23,21	2,98	0,67
	October	7,12	3,53	17,18	2,28	0,85
	November	4,39	2,82	9,72	1,61	0,90
Winter	December	5,75	3,38	13,35	1,83	0,89
	January	6,33	3,61	14,99	2,64	0,91
	February	9,43	6,35	20,04	3,54	0,68
Spring	March	13,49	11,38	26,02	5,26	0,42
	April	15,28	15,23	26,62	6,85	0,23
	May	11,85	11,80	17,83	6,78	0,16
Summer	June	9,93	10,09	15,41	5,61	0,06
	July	8,91	8,75	14,66	4,36	0,21
	August	5,96	4,65	11,47	2,78	0,62

Figure 6.5 illustrates the seasonal variations in foF2, hmF2 and TEC. Panels in this figure summarize the findings in the monthly plots of previous Figure 6.2, 6.3 and 6.4. It is clear that the highest electron density is found in Spring and the lowest is in Summer. As the solar radiation is expected to be highest in Summer, this result reflects the dynamics in the ionospheric electron density in F2 region. This is also supported by the highest variability seen during daytime in Summer. It is also noticeable that during the daytime in Summer, electron density in F2 region relatively flat though fluctuations are seen throughout the day. The electron density peaks at 06:00 UT, then decreases a bit and then rises again at 12:00 and then decreases some and then increases to a maximum at dusk at 18:00 UT. The peak densities in Fall, Winter and Springs seasons surprisingly very close to each other varying from 8 MHz in Autumn and Winter to 9 MHz in Spring. The Autumn and

Winter dynamics must be operating such that they add on the effects of solar radiation flux.

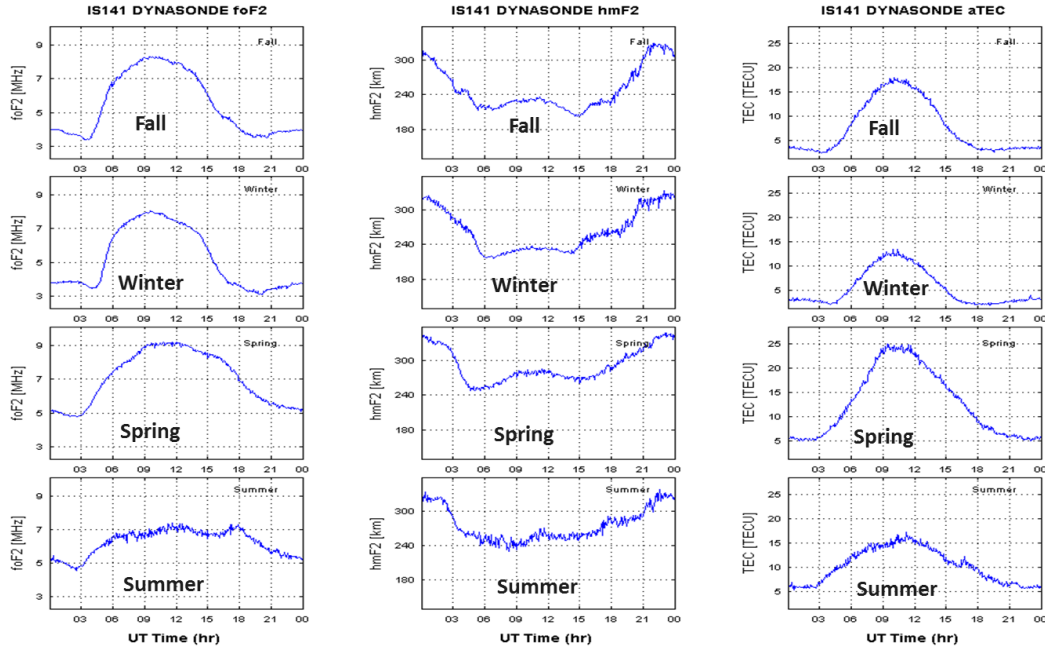


Figure 6.5: Seasonal variations of foF2 (first column), hmF2 (second column) and TEC (third column).

The nighttime F2 region electron densities are seen to lie below 6 MHz in all seasons except in Summer when they increase above 6 MHz. Winter distribution is narrower while the Spring and Summer distributions are broader. The differences between day and night electron densities are highest in Winter and smallest in Summer. We can see the seasonal statistic characteristics of foF2 in Table 6.4.

Table 6.4: Statistical properties for foF2 data given in Figure 6.5.

	Mean	Median	Max	Min	Skewnes
Fall	5.48	4.59	8.25	3.44	0.39
Winter	5.17	3.97	7.96	3.22	0.44
Spring	7.07	7.25	9.13	4.84	-0.07
Summer	6.24	6.6	7.12	4.72	-0.62

Figure 6.5 also shows that height of the foF2 shows rather similar variations in Autumn, Winter, and Spring such the highest altitudes occur during the night and lower altitudes are found during the day at midday. In Summer, the daytime variation disappears and height does not change much staying stable at about 240-250 kms. Table 6.5 gives the seasonal statistical properties detected in hmF2.

Table 6.5: Statistical properties for hmF2 data given in Figure 6.5.

	Mean	Median	Max	Min	Skewnes
Fall	249	231	325	205	0.93
Winter	263	258	325	218	0.51
Spring	291	280	344	251	0.57
Summer	275	262	326	241	0.73

Seasonal TEC behavior given in Figure 6.5 is that from Winter till Summer the midday TEC increases while in Summer it reaches its minimum. The distribution is broader and flatter during the day in Summer while it is narrower and sharper during the day in other seasons. The highest TEC during the day is found in May while the lowest is seen in Winter. Nighttime TEC in Summer is much higher than the nighttime TEC in other seasons. These results point again at a different dynamics that affect the TEC distribution at Istanbul during the course of the day. Table 6.6 gives the seasonal statistical properties detected of TEC.

Table 6.6: Statistical properties for TEC data given in Figure 6.5.

	Mean	Median	Max	Min	Skewnes
Fall	7.75	4.52	17.29	2.84	0.73
Winter	5.49	3.21	12.40	2.24	0.89
Spring	12.07	10.99	23.99	5.39	0.46
Summer	10.23	10.32	15.87	5.72	0.14

6.2 Typical Ionospheric Daily Variations Observed At Istanbul

Figure 6.6 gives the examples of daily variations detected by scanning 1 year of ionograms. These reflect the most typical variations observed during the day. First panel at the top is a typical solar radiation variation observed in September 19, 2013. The second from the top shows two shoulder around noon depression and it is observed in March 18, 2013. The third one is observed in April 30, 2013 and shows wavy fluctuations in the evening times on to of the daily solar radiation variation. Wavy variation are not always seen at dusk but also in the morning times as well. This is different than the dusk phenomena although sometimes an increase in the level of ionization as in the dusk phenomena is seen together with the wavy structure as well. The last panel shows the dusk or afternoon phenomena which is a secondary peak in the daily variation of electron density.

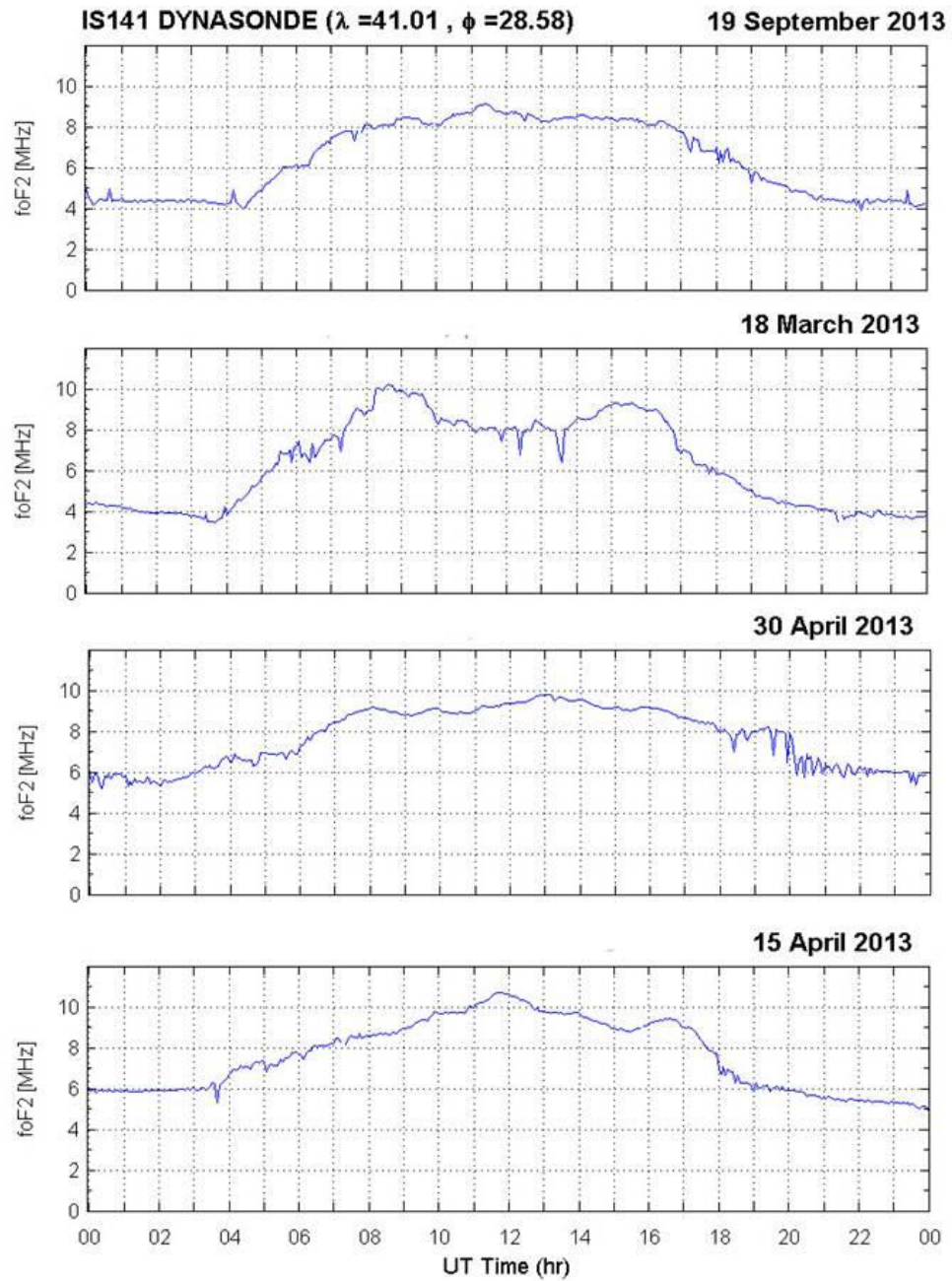


Figure 6.6: Four typical daily variations observed in foF2 in 2013 at Istanbul.

Figure 6.7 below is given to illustrate two different dynamics occurring in different days randomly selected, April 21 (top) and April 24, 2013 (bottom).

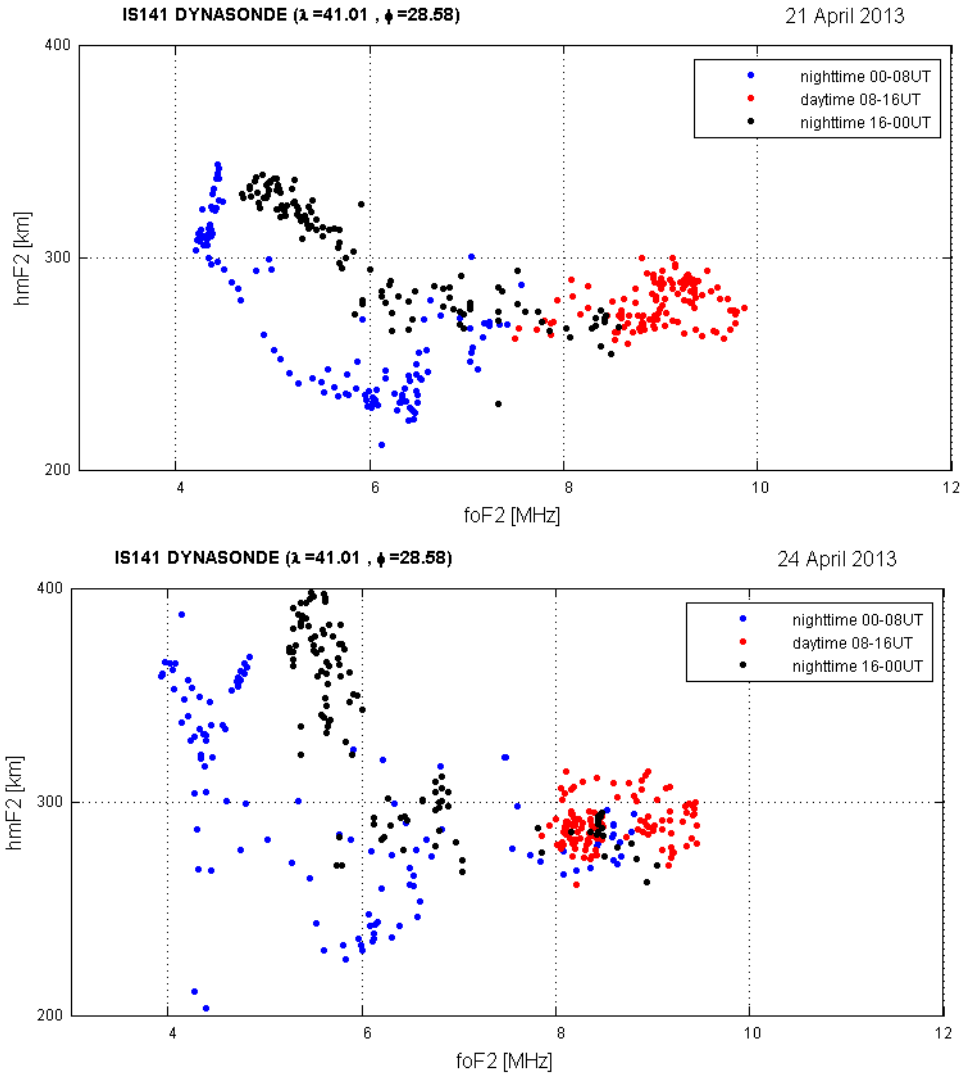


Figure 6.7: Variability illustrated with foF2 versus hmF2 for two events.

In the figure, foF2 on the horizontal axis is plotted against hmF2 in the vertical. Each plot represents a day. Blue and black dots in the figure present the morning hours from 00:00 UT to 08:00 UT and evening hours from 18:00 UT to 00:00 UT. Daytime from 08:00 UT to 18:00 UT is shown in red. It is clear that in the second panel there is a high scatter at night compared to the first one. In the first panel, during the day, the signals with higher frequencies than 6.5 MHz reflect from 20 km on the average. However, in the second panel we see that the signals with higher frequencies above 6 MHz reflect from about 300 km during the day. During evening hours in the first panel, the signals with frequencies between 4.5 and 6.5 MHz reflect from 260-330 kms while in the second panel during the evening hours, signals with frequencies from 5.5 and 6 MHz are reflected from regions varying between 260-400 kms. During the morning times (blue), on the other hand, on both plots, the

frequencies from 4 to 6.5 MHz are reflected from altitudes between 200-350 kms. Two types of clustering are obvious in the figure. One is the signals with frequencies less than 6-6.5 MHz and the other is those greater. During day, the reflection height does not change much and stays stable in both days.

Figure 6.8 gives an example of gravity wave influence in our data set. The disturbance seen at the top of the left ionograms, which are given in two sequential time intervals at 03:00 UT and 03:04 UT, at about 360 kms progresses downward to lower altitudes. The panels at right illustrate the daily variation on this day. In addition to the wave structure seen in the morning around and after 06:00 UT, the signatures of gravity waves are continuously are seen during the early morning at about 06:00 Local Time. The expanded version of the time of occurrence is given below in Figure 6.9. Although the variation in height range (bottom panel) is small and not sharply noticeable, the wave structure with decreasing frequency levels, indicating decreasing electron densities, is clearly seen at 4 min intervals.

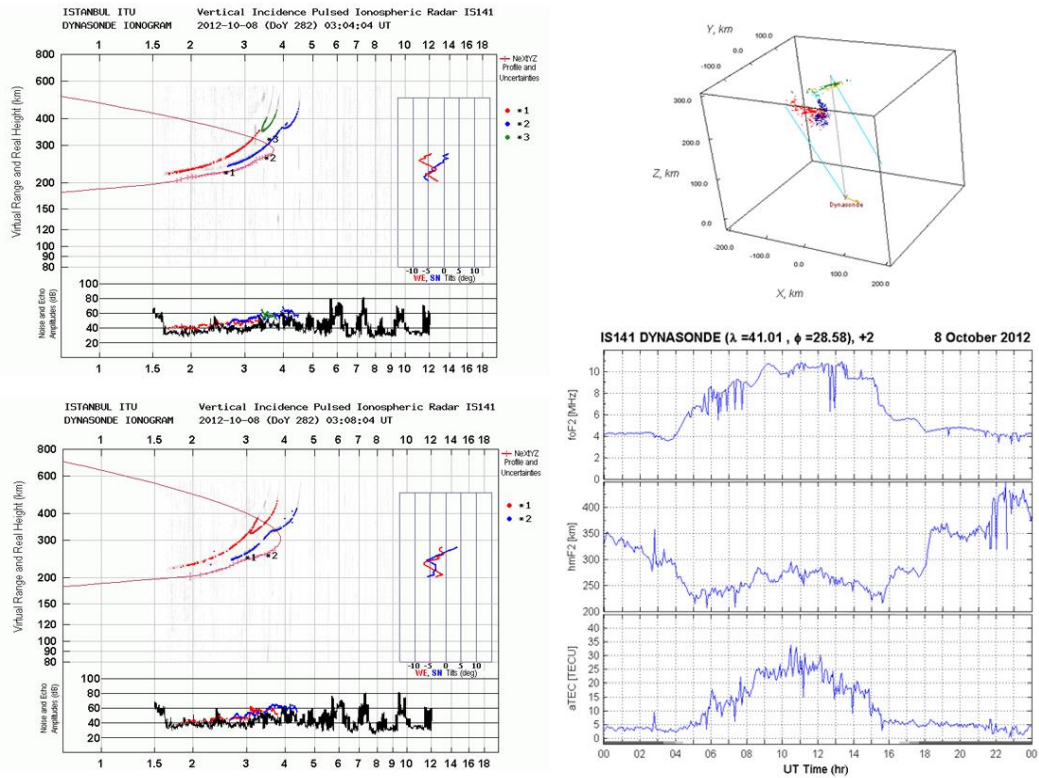


Figure 6.8: Gravity wave example seen on day of October 8, 2012.

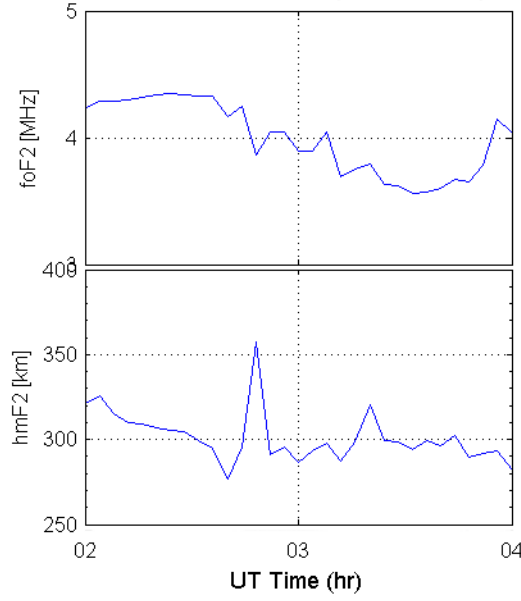


Figure 6.9: Expanded version of Figure 6.8 to show the gravity wave structure in detail.

6.3 Substorm Effects

The effects of magnetic storms and magnetospheric substorms are studied using selected Case. In order to determine when the storm or substorm occurs, magnetic indices are used. Below we first give a very brief information of the storm and substorm indices used in this study, which are Dst and AE, AU/AL.

Storm Index: D_{ST}

Disturbance Storm Time (D_{ST}) index is derived from four globally distributed equatorial magnetometer stations. D_{ST} index value reflects the variations in the ring current in the magnetosphere. It is calculated using the horizontal component of the magnetic field recorded by these four stations. When solar wind dynamic pressure first interacts with the magnetopause at the nose of the magnetosphere, it compresses the magnetosphere. This compression is transmitted through the field lines to the equatorial stations and an increase in the field strength as a result of the compression is recorded at those stations. This increase is called Sudden Commencement (SC) and it occurs just prior to the magnetic storm. Therefore, D_{ST} index is a good indicator to the global magnetic storms. The D_{ST} index values less than -40 indicate the storm occurrence.

Substorm Index: AE/AL/AU

AE index is Auroral Electrojet index. It is calculated by using AL and AU indices, which are also auroral indices. AL and AU, Auroral Lower and Auroral Upper indices are associated with westward and eastward electrojets. They are calculated using the magnetic field measurements of 13 high latitude Scandinavian magnetic stations distributed around 70° latitude. Variations in the magnetic field in these stations occur due to the intensifications in electrojets. These intensifications in the electrojet are caused by the reconnection in the magnetotail and thus referred as the magnetospheric substorm. They indicate the ejection of the particles into the ionosphere. The magnetic field variations from these stations are superposed during a day. The lower envelope of the variations caused by the westward auroral electrojet gives the Auroral Lower index, AL while the upper envelope of the variations makes the Auroral Upper index, AU. The total strength of the magnetospheric substorm is then found by adding these two as $AE = AU + |AL|$. AE index greater than 100 points to a substorm occurrence in the magnetotail

To examine the effects of magnetic storms and/or magnetospheric substorms, four cases were selected. One of these cases corresponds to magnetically quiet time conditions. That is, no magnetic storm and/or magnetospheric substorm occurred on that day. In other three cases, magnetospheric substorms occurred, thus those days are described as magnetically disturbed days. Quiet day was observed in April 21, 2013 with very low fluctuations in D_{ST} and AE indices. Disturbed cases are 17/03/2013, 29/03/2013, and 24/04/2013, which are given in the order of the strength of the magnetospheric substorm; strong, moderate and weak respectively. Table 6.7 shows the daily peak of the D_{ST} and AE values for all cases studied.

Table 6.7: Mean D_{ST} and AE values for selected cases.

Cases	Date	Peak D_{ST}	Peak AE
Quiet Day	21/04/2013	2	46
Disturbed-1	17/03/2013	-132	1019
Disturbed-1	29/03/2013	-60	723
Disturbed-1	24/04/2013	-49	668

In Figure 6.10, daily variations for these four cases are given from left to right as Quiet, Disturbed-1, Disturbed-2, and Disturbed-3 corresponding to April 21, March 17, March 29 and April 24 respectively. Panels from the top to bottom at each

column are auroral index, represented by AL and AU indices, D_{ST} index, foF2, hmF2 and TEC. The reference line at “0” is given in orange color. We can see that the foF2 during Disturbed-1 day resents higher values compared to other two less disturbed days and quiet day. One thing, which is clearly seen, is the increased level of fluctuations in the afternoon extending toward the evening. The substorms effects are more noticeable in the variations of peak foF2 such that hmF2 tends to be increased with increasing Dst index during Disturbed-1 while it rather flattens compared to the quiet day variation during Disturbed-2 and Disturbed-3. Since the dates of the selected cases are very close to each other, the solar radiation is not expected to cause these variations. While the quiet day TEC illustrates a symmetrical structure around noon, it shows a secondary peak in the afternoon started at around 14:00 UT during Disturbed-1. The highest peak occurs during Disturbed-1 and the lowest, lower than that in quiet day, daytime variation is found during Disturbed-2 while it shows humble double peak structure with a midday depression during Disturbed-3.

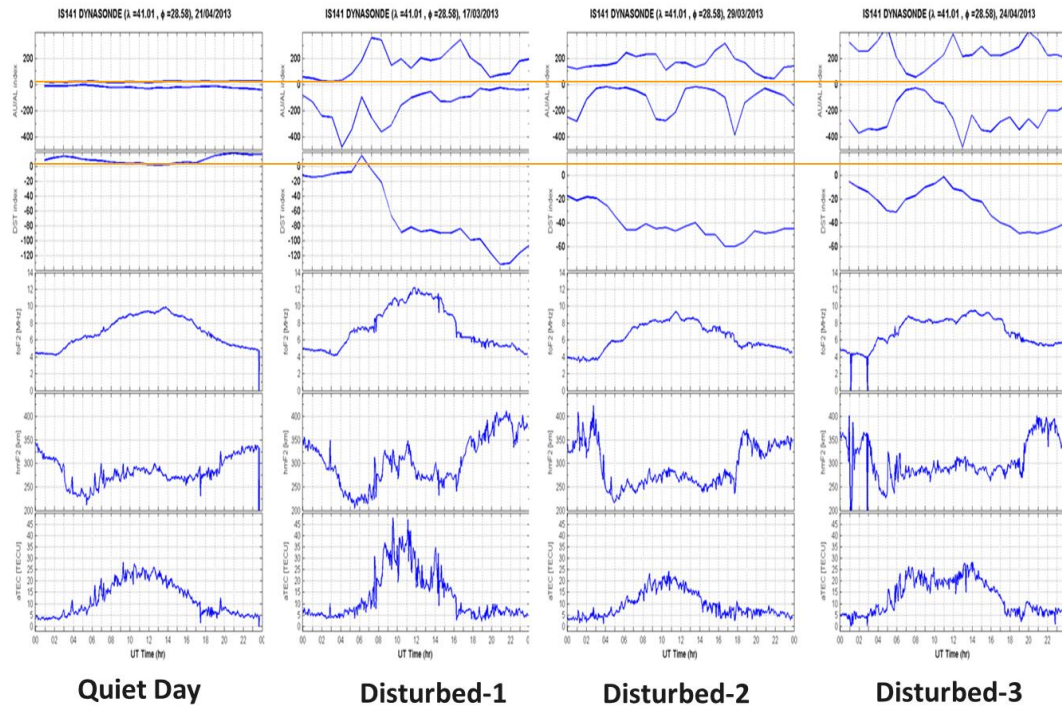


Figure 6.10: Daily variations of ionospheric parameters, foF2, hmF2 and TEC on selected quiet and disturbed days.

To extract the substorm effects, we use IRI and TIE GCM models. This way we both test the models against ITU data and eliminate the non-substorm effects, which are not included in both models efficiently. For this purpose, Figure 6.11 compares the daily variation of TEC of the selected cases with those of the models. In the figure, we can see that TIE-GCM model (blue) and ITU data agrees very well while IRI model overestimates the daily variation seen at ITU. Both models are good to predict the peak occurrence for the quiet day. However, both models do not represent the ITU data during the magnetically disturbed days. Still, TIE-GCM gives closer predictions to the data than that of IRI in terms of both magnitude of TEC and the timing of the peak occurrence. TIE-GCM model is better and closer to the data during the night from 18:00 UT till morning 08:00 UT than it is during the day. Fluctuations overlapped on the daytime variations are not found in both models. Both models give average variations in the ionosphere and are not expected to replicate the higher order fluctuations and the external effects, which are inherently found in the data like effect of the substorms. The solar activity is incorporated in both models through planetary Kp index. However, we can see from this figure that this is not good enough to predict the variations resulting from the solar and magnetospherically originated effects.

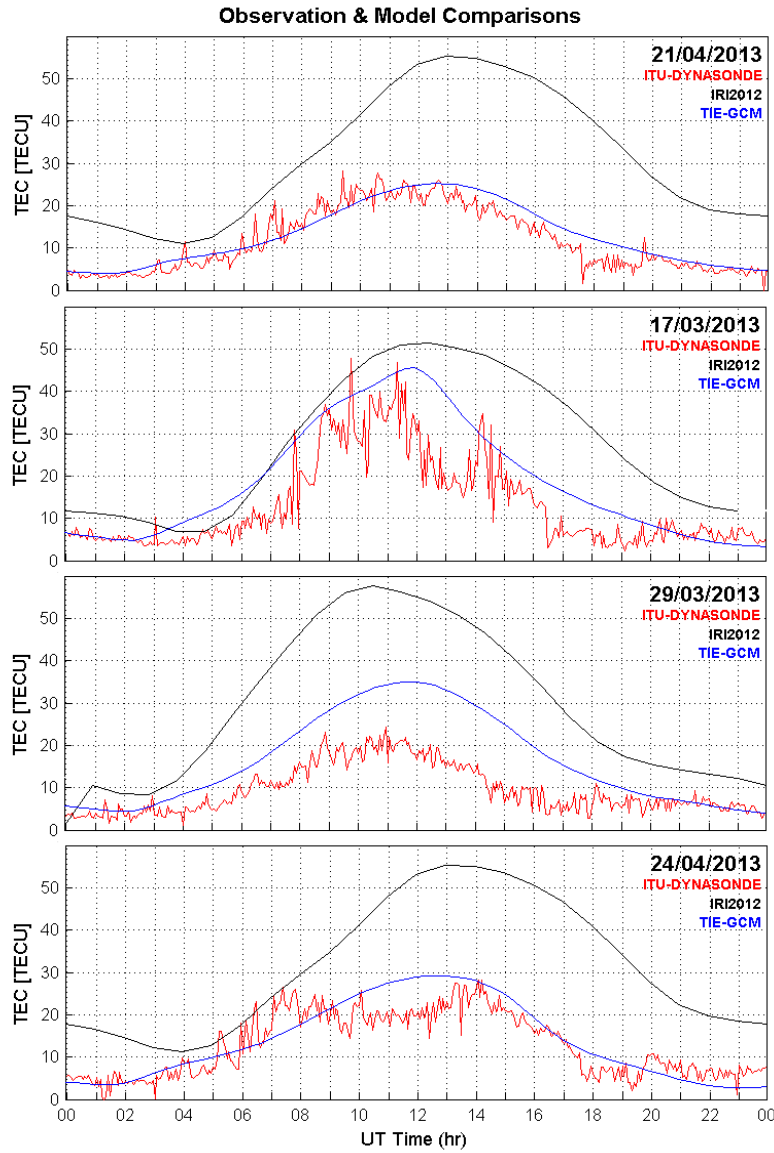


Figure 6.11: Comparison of the daily variation of TEC of the selected cases with those of the models.

Figure 6.12 gives the differences obtained by subtracting the predicted model values from the data. We can see that the vertical axis of the plot runs from 0 to -40, which means that the model predicts smaller values than the data. The difference is smaller with TIEGCM model than that with IRI model. Differences are also smaller during the night than that during the day. We can also see that the differences are also smaller during the most active day, Disturbed-1, while they are greater during the less disturbed day, Disturbed 2. Smaller difference indicates the models predict closer to the data. The largest differences for both models are seen during the quiet

day. However, TIEGCM agrees better with the data than IRI during the quiet day. As a result of this figure, we can say that the differences increase with increased activity level.

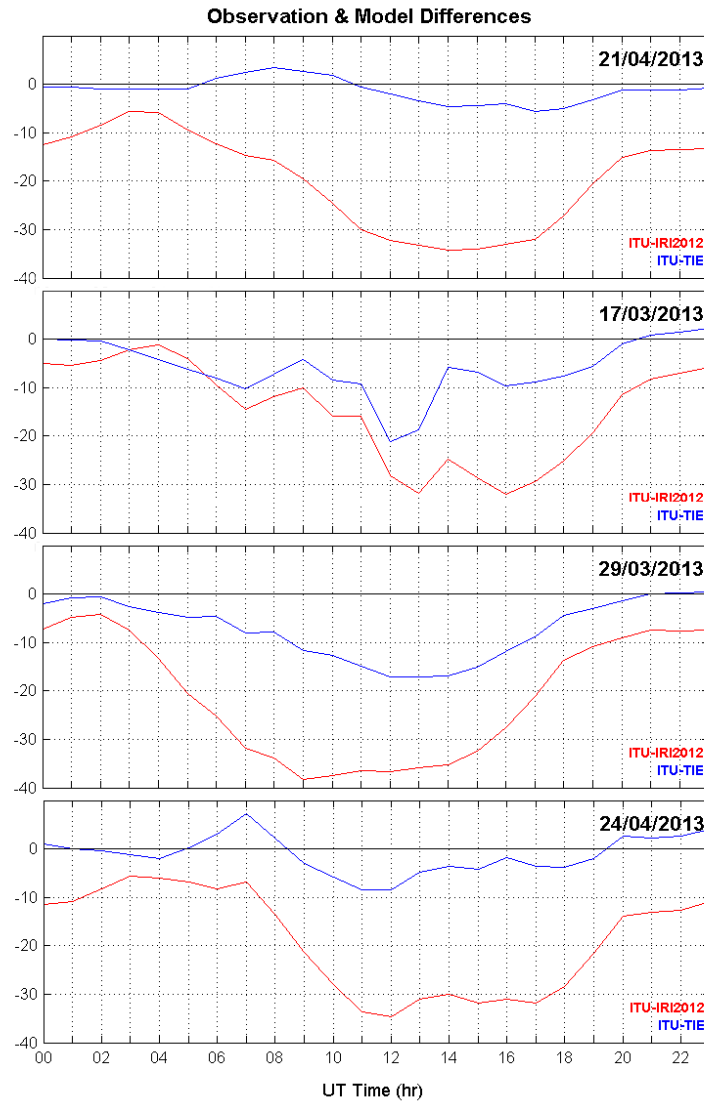


Figure 6.12: Differences between the model predictions and ITU Dynasonde data for selected quiet and magnetically disturbed days.

Figure 6.12 above, models differ even during the quiet day where one expects the agreement will be less than seen in this figure.

Figure 6.13 shows the electron density profiles produced by the software NeXtYZ for different phases of the substorms. The substorm phases are the beginning, expansion and recovery of the substorms and defined by examining the variations of

Dst and AE/AL/AU indices given in Figure 6.10. The beginning phase of the substorm is recognized when a decrease in Dst and AL index. This is seen just after the sudden commencement in Dst index. It occurs at 06 UT (for the Disturbed-1 case in Figure 6.10 second panel) in Dst and thus marks the beginning. The expansion phase of the substorm is the phase of the substorm when the energy transferred into the atmosphere and lasts from the beginning of the substorm until the recovery when the energy transfer from the magnetotail ceases and the magnetotail configuration starts to recover toward its background geometry. For representation of expansion phase, we took the mid occurs at 17 UT (for the Disturbed-1 case in Figure 6.10 second panel) and represents the expansion phase for our substorm events. Lastly, the recovery starts when both indices start to decrease/cease towards their background values. Both indices reach a negative peak at the beginning of the recover. This occurs at 23 UT (for the Disturbed-1 case in Figure 6.10 second panel) and gives the start of the recovery. For quiet day, for comparison purpose, we used the profiles plotted corresponding to the average time of the each substorm phase from 3 magnetically disturbed days. Thus, this way we compare about the same time of the day with the time of the corresponding substorm phase in each of the disturbed day as the quiet day does not include the substorm effects and we cannot define substorm phases for it.

In Figure 6.13 below, we can see the height of the peak in the profiles and the electron densities at these peaks differ at each phase of the substorm. E region is evident at about 100 km in both expansion and recovery phases but not seen in the beginning phase. In both of the disturbed days, we can see that the expansion phase is broader, and has higher density than that of quiet day (except Disturbed-3 when we do not have data). Especially, in the second panel, peak electron density is seen to increase from $0.9 \times 10^6 \text{ \#/cm}^3$ to $1.6 \times 10^6 \text{ \#/cm}^3$. It is also clear that the recovery phase electron density is the lowest in general (except the 3rd substorm, which is the weakest) and the height that it occurs is the highest when compared to the beginning and expansion phases.

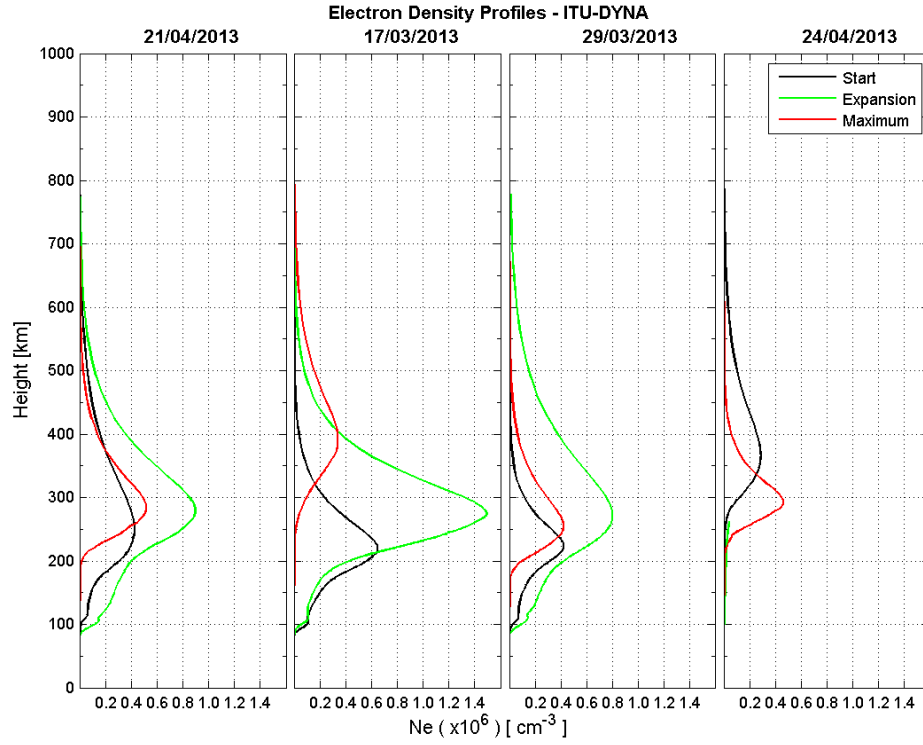


Figure 6.13: ITU electron density profiles produced by NeXtYZ at different phases of the substorms for the selected cases. Black, green and red denote the beginning, expansion and recovery phase of the substorms respectively.

Figure 6.14 examines the dependence of the electron density on the phase of the substorms further. In the figure, ITU-Dynasonde data are compared with the model results during the different phases of the substorms.

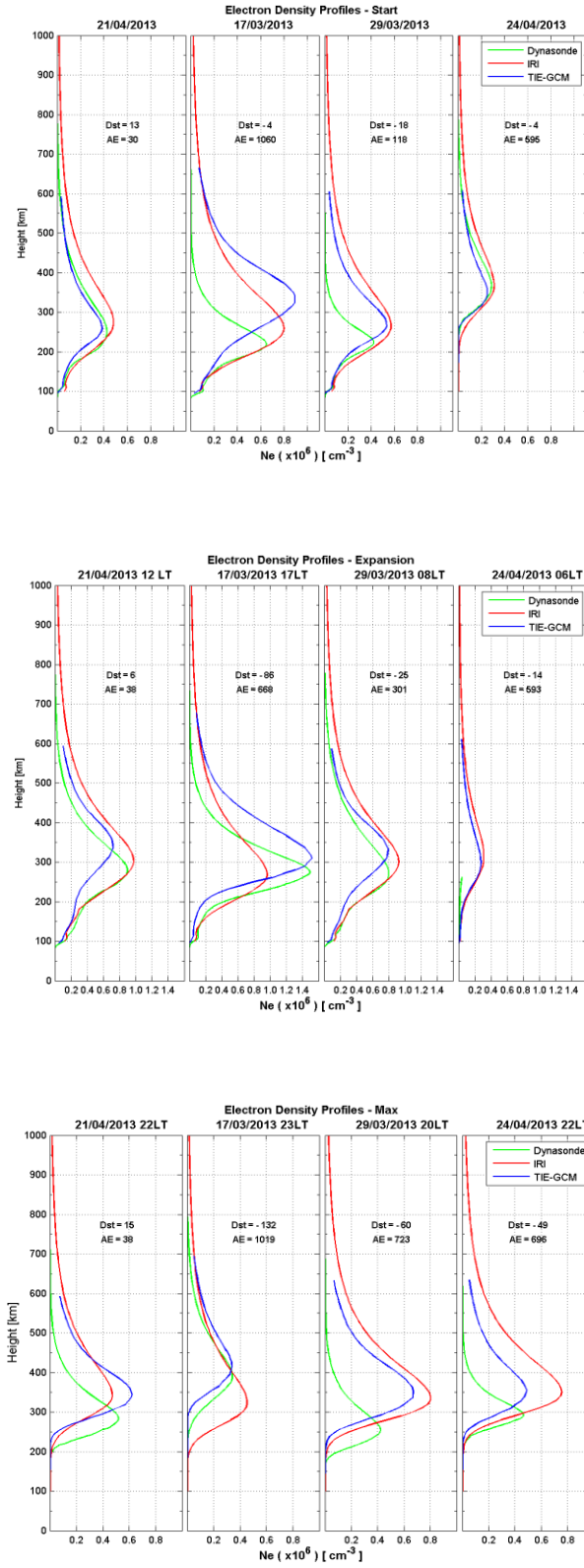


Figure 6.14: Model-Data comparisons during the different phases of the substorms during beginning (top), expansion (middle) and recovery (bottom) phases.

The agreement between the models and the ITU data during the expansion phase is better in that the peak height where the electron density is maximum is closer to each other while in the beginning and recovery phases the peak occurs at higher altitudes than that in the expansion phase. TIE-GCM gives the higher agreement than IRI model in predicting the height of the peak electron density. Also the models predict the peak electron density during the recovery phase much higher than that in other phases. Disagreements between the models and the data increases in recovery phase.

Figure 6.15 compares the daily profiles from the models at different phases of the substorms for comparisons. In the figure, we can see that the middle panel, expansion phase plots, is distinctly different from other two panels corresponding to beginning and recovery phases. The highest electron densities were obtained during the expansion phase of all substorms. The peak altitude is found to be almost the same in both data and the models. While Disturbed-1 electron densities are the highest during expansion phase, these reach to the lowest during recovery phase. Even though quantitatively there is a big difference between the peak altitudes and the peak electron densities, it can be said that there is a qualitative agreement between the models, and between the data and the models. Expansion phase presents much different structure than the other phases where both the peak altitudes agree though the peak electron densities are different. The disagreement is higher in beginning and recovery phases where the electron densities and peak altitudes display an unpredictable character.

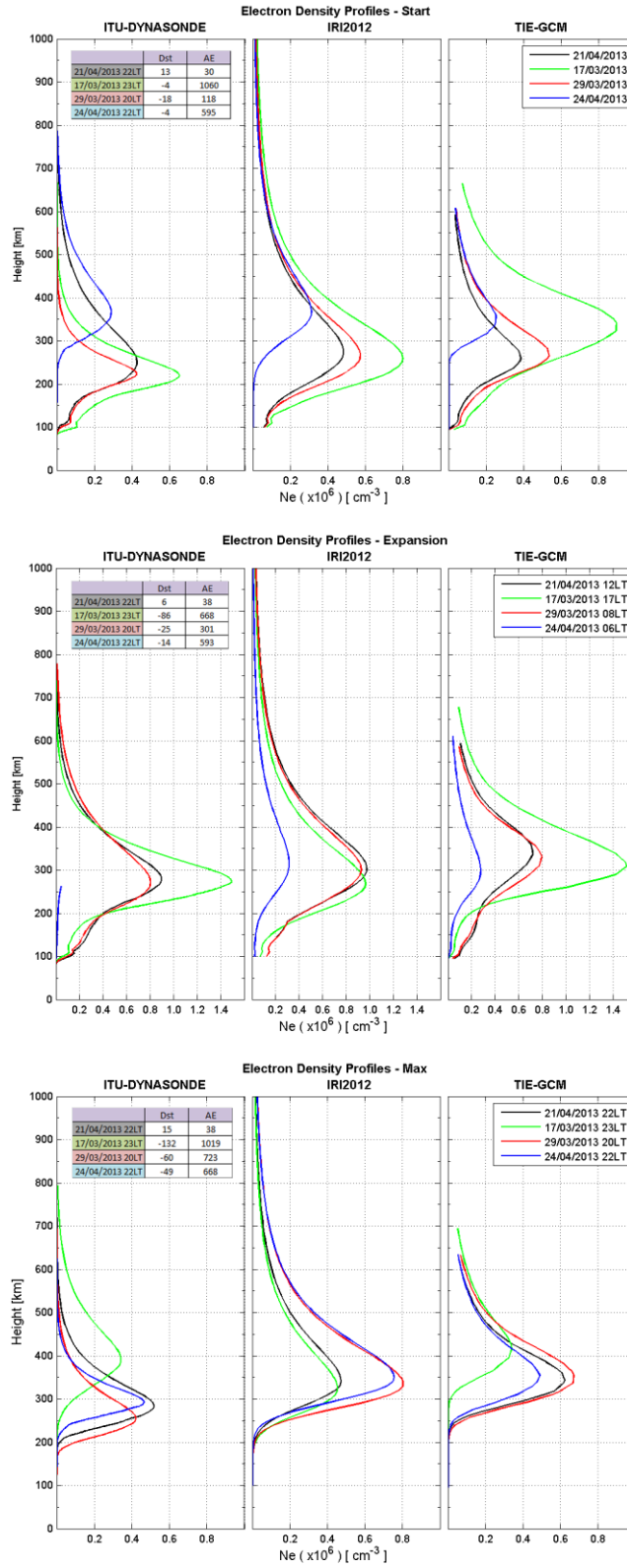


Figure 6.15: Comparisons between the models during the different phases of the substorms during beginning (top), expansion (middle) and recovery (bottom) phases.

In Table 6.8, we present the statistics from these comparisons between the model-data and model-model.

Table 6.8: Statistics from model-model and model-data comparisons.

Quiet Day	21/04/2013		
	ITU-DYNA	IRI2012	TIE-GCM
Maximum height (km)	283	330	344
Maximum Ne (10^6 cm^3)	0.98	2.04	0.9
Disturbed-1	17/03/2013		
	ITU-DYNA	IRI2012	TIE-GCM
Maximum height (km)	295	300	390
Maximum Ne (10^6 cm^3)	1.47	1.93	1.68
Disturbed-2	29/03/2013		
	ITU-DYNA	IRI2012	TIE-GCM
Maximum height (km)	274	310	354
Maximum Ne (10^6 cm^3)	0.83	1.99	1.42
Disturbed-3	24/04/2013		
	ITU-DYNA	IRI2012	TIE-GCM
Maximum height (km)	289	330	362
Maximum Ne (10^6 cm^3)	0.78	2.03	1.05

7. SUMMARY AND CONCLUSIONS

Determining the ionospheric structure and its variability is very important for the ionospheric predictions. The temporal and spatial variations in electron density affect the frequency of the radio waves used to communicate with satellites and with long distance communications. Ionospheric variability introduces range errors in GPS communication up to 100 meters if they are not corrected in GPS range prediction models/algorithms. Since the ionosphere changes with time of day, season, solar activity, and substorms, the resulting range errors changes with these parameters as well together with the viewing direction, location of the receiver. These range rate errors are caused by the rate of change of the total number of electrons along the line of site of the signal. During intense magnetic storms, auroral effects can extend down to the mid latitudes and cause unusual effects on GPS receivers. During these times, ionospheric range correction algorithms for single frequency do poor job of correcting range errors and rare and range-rate changes will be much larger during magnetically quiet times. GPS receivers are lack of following the rapid variations in TEC created by the magnetic storms exceeding for example 1 Hz changes within seconds [38]. Many technological systems on Earth, such as navigation, target detection, radar studies, geological surveys, position determination etc, as well as many of the technical appliances used in our life and already a unavoidable and vital for our daily habits such a cell phones, TV applications rescue systems, loss findings, etc. rely upon the accuracy of the GPS. Therefore, it is crucial to know and timely predict the variations in ionospheric electron density in order to assess the maximum and correct use of GPS data.

In this study, the main purpose was to drive the ionospheric parameters and determine their day-to-day and seasonal variability at Istanbul, a midlatitude location and during magnetically disturbed times using VLF and HF signals. Both measurement systems are located at ITU and record data at high resolution of their times ever available in Turkey. VLF signals from around the globe are received at

ITU and studied to determine the variations in D layer while HF radar signals from Dynasonde system at ITU are used to study the E layer structure and variations. Model comparisons with case studies are presented. The preliminary results are presented in this thesis. In this section, We can summarize our findings below;

1. Ionospheric D layer affects the behavior of VLF signals. Either it can reflect the signals like in the mirror case or it can let some portion of the signal pass in and causes some dispersion and then reflects. Both variations are controlled by the solar activity through the ionization caused by the X ray flux enhancements during the solar flares. These show up themselves as the Sudden Ionospheric Disturbances and the response of the ionosphere differs according to how the ionization created by the flares. Sometimes see an increase immediately after the solar occurrence or followed by the solar flare or none. The exact structure and physical processes behind these responses need a more detailed focus study with more cases and as well as the statistical.
2. We determined four basic type of ionospheric response by examining the VLF signal variation at Istanbul. These are solar radiation track, midday depression, dusk increase and wavy structure. Midday depression, dusk phenomena and wavy structures point to the dynamics in the D layer of the ionosphere. The variations that we see with VLF data are similar to the ionosonde HF data and do not always follow the findings in the literature. This behavior in VLF signal should be discussed on the physical grounds and are not at the moment as clear and subjected to further investigation.
3. Most of the time, we find that the background VLF signal vary in accordance with the background solar radiation in that the signal rate is highest during the daytime, peaks at noon and decreases at night.
4. During the sunset and sunrise times, broad depressions in VLF data are seen especially during winter.
5. Several of the clear increases in the signal strength are found to be associated with the solar flare effects in the D layer of the ionosphere. However, this is not always the case. Sometimes the signal rate increases with no corresponding solar flare observed at GOES spacecraft, or vice versa. A deep investigation of these behaviors is needed to be done related to the D-region

dynamics. These cases may be other external, like magnetospheric, or local dynamical, causes that change the electron density level in the D region which in turn increase the signal level. However, this is subjected to further investigation. The purpose in this part was to derive the general structure and what already present, and bring out the problems, which need to be addressed in the future.

6. The wave activity with bout an hour periodicities in VFL signal especially after dusk throughout midnight is not reported before and must be related to the dynamics as well.
7. Both daily and seasonal variations of electron density of F layer (foF2) and TEC and maximum height at the electron density peak show several structures. In addition to the solar radiation driven ionosphere where F2 region electron densities peak at noon, we see depressions during the noon causing double hump around noon time and periodic wave activity after and around sunset and sometimes in the morning. These indicate an active ionosphere at F region heights. The F layer electron distribution does not always follow the Chapman profile and the winds at F region heights play very important role in redistributing the electron density. A further analysis on the dynamics is deferred to a later study.
8. The lowest F2 region electron density is found during the summer months while the highest is in Autumn, especially in month of October, and Spring. Summer months are seen to be most active in that the electron density is highly fluctuating during the day and extending into the night. A second enhancement in electron density appears toward the end of May throughout Summer, until end of August, at sunset times, which is called Dusk phenomena at mid-latitudes. Distribution of F layer electron density is skewed toward morning hours while it is rather symmetrical around noon during the spring and summer months. The hmF2 behavior follows the variations expected from the theory, i.e. smaller when electron density is high and higher when electron density low. Daily during the night times and seasonally summer months are the lowest heights that F2 layer peak as observed. The peak height of electron density increases during the midday and peak around noon as well but this increase never reaches to the level recorded at night. This midday behavior of

hmF2 is not pronouncedly seen during summer months and almost lost in August with a stable but fluctuating F2 layer.

9. There are wave structures recorded during the early morning extending into the mid-morning. These are thought to be the gravity wave signatures driven from the troposphere. An example of this is given but more examples and analysis are needed to understand this interaction between the ionosphere and troposphere. Waves are progressing from upper layers of F2 region downward with electron densities gradually decreasing. A detailed analysis of this case and others is underway.
10. We have studied the substorm effects on electron densities on 3 cases. Generally we have seen that the electron densities can both decrease and increase during the substorms. In our first case corresponding to the strongest substorm, we have observed increased densities during the daytime and also a secondary increase around dusk. In our second and third cases, we have seen that the electron densities decrease being lower than those during quiet time.
11. IRI and TIEGCM model total electron density (TEC) were compared with ITU TEC data. Here we see that both models overestimate the TEC measured at ITU, a midlatitude station. However, differences between the TIEGCM model results and ITU TEC is smaller than that between IRI and data. Also, the model-data differences are larger during the day than during the night for both models.
12. Electron density profiles from both models and ITU data show that the models agree with ITU data during the beginning and recovery phases but differ during the expansion phase. The height of the peak electron density is also closer to the data at the beginning and recovery phases while large discrepancy is seen during the expansion phase.
13. Model-model differences for electron density were found to be larger during the day and larger during the expansion phase of the substorms.

FUTURE WORK

Several studies need to be carried out as follow up to the study we presented here. Ionosphere is very dynamic region of the atmosphere where both plasma motions and neutral-plasma interactions take place. Its variations can change in the range

from seconds to years and in local to large spatial scales. The ionosonde system at ITU is a newly established system with high resolution and it is the only one in this geography. It represents Middle Eastern and the West Caucasian areas where there are no ionospheric measurements are taken. Our measurements give support to derive the ionospheric variability in this region, and in addition, help to improve the ionospheric network at midlatitudes. Therefore, in this work, as a preliminary study, our focus was to determine the basic, general structure of the ionosphere at Istanbul (41.1 N, 29E). We have established the some of the essentials related to the general characteristics of the ionosphere, its day-to-day, seasonal variability as well as its behavior in response to the substorms. However, we have not really studied the physical or dynamical causes. Therefore, our next goal should be to look into the underlying physics and dynamics behind this variability observed by ITU Dynasonde.

REFERENCES

- [1] **Url-1** <<http://www.ips.gov.au/Educational/5/2/2>>, date retrieved 10.12.2013.
- [2] **Url-2** <<http://roma2.rm.ingv.it/en>>, date retrieved 10.11.2013.
- [3] **Url-3** <http://www.luminoruv.com/uv_101.php> , date retrieved 19.11.2013.
- [4] **Url-4** <<http://www.infocellar.com/networks>>, date retrieved 10.12.2013.
- [5] **Url-5** <<http://www.iap-kborn.de/Ionosondl>>, date retrieved 10.12.2013.
- [6] **Url-6** <<http://www.ukssdc.ac.uk/ionosondesl>>, date retrieved 10.12.2013.
- [7] **Url-7** <<http://www.ngdc.noaa.gov/stp/iono>>, date retrieved 05.12.2013.
- [8] **Url-8** <<http://dgn7.esoc.esa.int/studies/ionostud/>>, date retrieved 10.11.2013.
- [9] **Url-9** <<http://www.aavso.org/solar-sids>>, date retrieved 14.12.2013.
- [10] **Url-10** <<http://sidstation.loudet.org/>>, date retrieved 13.12.2013.
- [11] **Url-11** <www.spaceweather.com>, date retrieved 15.12.2013.
- [12] **Url-12** <<http://www.radio-electronics.com/info>>, date retrieved 10.12.2013.
- [13] **Url-13** <<http://www.radio-electronics.com/info>>, date retrieved 10.12.2013.
- [14] **Mendillo, M.** (2006). Storms in the Ionosphere: Patterns and Processes for Total Electron Content. *Reviews of Geophysics*, RG4001.
- [15] **Url-14** <cedarweb.hao.ucar.edu/workshop/>, date retrieved 10.12.2013.
- [16] **Hocke, K. and Schlegel, K.** (1996). A review of atmospheric gravity waves and travelling ionospheric disturbances: 1982–1995, *Ann. Geophys.*, 14, 917–940, doi:10.1007/s00585-996-0917-6..
- [17] **Y. Otsuka, K. Suzuki, S. Nakagawa, M. Nishioka, K. Shiokawa, and T. Tsugawa** , (2013). GPS observations of medium-scale traveling ionospheric disturbances over Europe, *Annales Geophysicae*, 31, 163–172, 2013, doi:10.5194/angeo-31-163-2013 .
- [18] **Url-15** <<http://www.radio-electronics.com/>>, date retrieved 10.12.2013.
- [19] **Thomson, N.R., and Cliverd, M.A.,** (2001). Solar Flare Induced Ionospheric D-region enhancements from VLF amplitude observations, *Journal of Atmospheric and Solar-Terrestrial Physics*, 63, pp. 1729-1737.
- [20] **McRae, W., & Thomson, N.R.** (2003). Solar Flare Induced Ionospheric D-Region Enhancements From VLF Phase And Amplitude Observations. *Journal of Atmospheric and Solar-Terrestrial Physics*, 66, 77-87.
- [21] **Url-16** <<http://user.tninet.se/~sdt522w/sid01.htm>>, date retrieved 10.12.2013.

- [22] **Url-17** < <http://solar-center.stanford.edu/SID> >, date retrieved 10.12.2013.
- [23] **Url-18** < <http://www.radioastrolab.it/> > , date retrieved 10.12.2013.
- [24] **Grubor, D., Sulic, D., and Zigman, V.,** (2005). Influence of Solar X Ray Flares on the Earth-Ionosphere Waveguide, *Serb. Astron. J.* No 171, 29-35, Doi.:10.2298/SAJ0571029G.
- [25] **Sulic, D., Cadez, V., Grubor, D., and Zigman, V.,** (2006). Space Weather Signatures on VLF Radio Waves recorded in Belgrade, *Publ. Astron. Obs. Belgrade.* No 80, 191-195.
- [26] **Liu, L., Wan, W., Ning, B., Pirog, O., & Kurkin, V.** (2006). Solar activity variations of the ionospheric peak electron density. *J. Geophys. Res.*, 111,, A08304.
- [27] **Park, Y.** (2010). *J. Astron. Space Sci.* 27(4), 319-327.
- [28] **Lanzerotti, L., Cogger, L., & Mendillo, M.** (1975). Latitude Dependence of Ionosphere Total Electron Content: Observations During Sudden Commencement Storms. *Journal of Geophysical Research*, 10, 1287-1306.
- [29] **Klobuchar, J., Mendillo, M., Smith III, F., Fritz, R., Da Rosa, A., Davis, M., and Flaherty, B.** (1971). Ionospheric Storm on March 8, 1970. *Journal of Geophysical Research*, 76, 6202-6207.
- [30] **Hibberd, F., & Ross, W.** (1967). Variations in Total Electron Content and Other Ionospheric Parameters Associated with Magnetic Storms. *Journal of Geophysical Research*, 72, 5331-5337.
- [31] **Tsagouri, I., Belehaki, A., Moraitis, G., & Mavromichalaki, H.** (2000). Positive and Negative Ionospheric Disturbances at Middle Latitudes During Geomagnetic Storms. *Geophysical Research Letters*, 3579-3582.
- [32] **Risbeth, H.** (1997). The Ionospheric E-layer and F-layer dynamos - a tutorial review. *Journal of Atmospheric and Solar-Terrestrial Physics*. Vol. 59, 1873-1880.
- [33] **Bergeot, N., Tsagouri, I., Bruyninx, C., Legrand, J., Chevalier, J., Defraigne, P., Pottiaux, E.** (2013). The Influence of Space Weather on Ionospheric Total Electron Content During the 23rd Cycle. *J. Space Weather Space Climate*, 3, A25.
- [34] **Mendillo, M. and Klobuchar, J.A.,** (2006). Total electron content: Synthesis of past storm studies and needed future work, *Radio Science*..
- [35] **Mendillo, M.** (1971). Ionospheric Total Electron Content Behavior During Geomagnetic Storms. *Nature Physical Science*, 234, 23-24.
- [36] **Hargreaves, J., & Bagenal, F.** (1977). The Behavior of the Electron Content During Ionospheric Storms: A New Method of Presentation and Comments on the Positive Phase. *Journal of Geophysical Research*, 82, 731-733.
- [37] **Mendillo, M., Risbeth, H., Roble, R., & Wroten, J.** (2002). Modelling F2-layer seasonal trends and day-to-day variability driven by coupling

with the lower atmosphere. *Journal of Atmospheric and Solar-Terrestrial Physics*, 64, 1911 – 1931.

- [38] **Klobuchar, J.** (1991). Ionospheric effects on GPS. *GPS World*, 1-4.
- [39] **Bilitza, D., Altadil, D., Zhang, Y., Merten, C., Truhilki, V., & Richards, P.** (2014). The International Reference Ionosphere 2012 – a model of international collaboration. *Journal of Space Weather and Climate*.
- [40] **Url-19** < <http://iri.gsfc.nasa.gov/>>, date retrieved 10.12.2013.
- [41] **Araujo-Pradere, E.A., Rowell, T.J., and Pilitza, D.**, (2004), Ionospheric variability for quiet and perturbed conditions, *Advances in Space Research*, Volume 34, Pages 1914-1921.
- [42] **Araujo-Pradere, E.A., Fuller-Rowell, T.J., and Spencer, P.S.J.**, (2006). Consistent features of TEC changes during ionospheric storms, *Journal of Atmospheric and Solar-Terrestrial Physics*, Volume 68, 1834-1842.
- [43] **Url-20** < <http://ccmc.gsfc.nasa.gov/models>>, date retrieved 09.12.2013.

CURRICULUM VITAE



Name Surname: Ayşegül Ceren Moral

Place and Date of Birth: 11 September 1987, Istanbul

Address: Istanbul Technical University ITU, Aeronautics and Astronautics Faculty Meteorological Engineering Department 34469 SARIYER/ISTANBUL TURKEY

E-Mail: moral@itu.edu.tr, kamuinokoi@hotmail.com

B.Sc.: ITU, 2011

EDUCATION

2007-2011 Istanbul Technical University (Istanbul, Turkey); Meteorology Engineering Program
Graduation Project: Geomagnetic Storm Analysis Using THEMIS Spacecraft Data
Date of Graduation: 2010-2011 Spring Term GPA: 3.02/4.00

2001-2005 Behçet Kemal Çağlar High School (Istanbul, Turkey)

INTERNSHIPS

2008 (16.06-11.07) Florya Meteorology Station/ Istanbul Atatürk Airport, Istanbul, Turkey (on Meteorological Instruments and Observations)

2010 (28.06- 23.07) General Directorate of Electric Power Resources Survey and Development Administration, EIE, Ankara, Turkey (on Hydrology)

2010 (09.08-03.09) Istanbul Atatürk Airport, Istanbul, Turkey / Dispatch Department (on Practical Internship)

PROFESSIONAL EXPERIENCE

2011 November-present Research Assistant at Istanbul Technical University,
Meteorology Engineering Department

VOLUNTARY WORK EXPERIENCE

2007-2008 Accountant of METAR (Meteorological Research
Student Club of ITU)

SCHOLARSHIPS

Mustafa Enver Adakan Foundation Scholarship for successful students; 2007-2011

PROJECTS

1. Graduate Student Researcher in TUBITAK Project 109Y058: Investigation of Geomagnetic Storms and Substorms and Their Effects on the Upper Atmosphere by Using THEMIS Spacecraft data : August 2011-July 2012, Finished
2. Graduate Student Researcher in BAP Project: Observation of Ionospheric Variations and their effects by SID Antenna, 2012-2014
3. Graduate Student Researcher in TUBITAK Project 113Y213: Space Weather From the Moon to the Ionosphere: September 2013-2016
4. Graduate Student Researcher in TUJJB-TUMEHAP Project, Determination of Ionospheric Variability over Istanbul Using Magnetotelluric methods; October 2012-2015

LIST OF PRESENTATIONS & PUBLICATIONS

August, 12-18 2012	Poster Presentation; A.C. Moral , F.T. Katircioglu, Z. Kaymaz, and D. Sibeck “Statistical Study of Plasma Depletion Layer” AOGS (Asia Oceania Geosciences Society) Singapore
April, 07-12 2013	Poster Presentation; A.C. Moral , Z. Kaymaz, ,F.T. Katircioglu, and D. Sibeck "Structure Of The Plasma Depletion Layer: Statistical Results from Multispacecraft" EGU (European Geosciences Union) General Assembly Wien, Austria

COMPUTER SKILLS

- Operating Systems ; Linux & Windows
- Programming; FORTRAN, MATLAB
- Modelling; Weather Research and Forecasting Model WRF
- Visualization Programs; GrADs, NCL, Ferret, Origin
- Statistical Programs; Minitab
- MS Office, Adobe Photoshop

LANGUAGES

English – Advanced
Japanese – Intermediate
French – Beginner

AREAS OF INTEREST

Planetary Atmospheres, Climatology, Physics of the Upper Atmosphere, Modelling, Space Weather, Magnetospheric Physics, Atmospheric Sciences

PUBLICATIONS/PRESENTATIONS ON THE THESIS

- A.C. Moral, E.C. Kalafatoglu, and Z. Kaymaz, 2013, "Sudden Ionospheric Disturbances and Their Detection over Istanbul", *Recent Advances in Space Technologies (RAST) Symposium*, June, 12-14 2013, Istanbul, Turkey
- A.C. Moral, Z. Kaymaz, F.T. Katircioglu, E.C. Eyiguler and N. Zaboltn, 2013, "Variations in mid-latitude ionospheric electron density using Istanbul Dynasonde observations", *CAWSES II Symposium*, November, 18-22 2013, Nagoya, Japan